



저작자표시-비영리-변경금지 2.0 대한민국

이용자는 아래의 조건을 따르는 경우에 한하여 자유롭게

- 이 저작물을 복제, 배포, 전송, 전시, 공연 및 방송할 수 있습니다.

다음과 같은 조건을 따라야 합니다:



저작자표시. 귀하는 원저작자를 표시하여야 합니다.



비영리. 귀하는 이 저작물을 영리 목적으로 이용할 수 없습니다.



변경금지. 귀하는 이 저작물을 개작, 변형 또는 가공할 수 없습니다.

- 귀하는, 이 저작물의 재이용이나 배포의 경우, 이 저작물에 적용된 이용허락조건을 명확하게 나타내어야 합니다.
- 저작권자로부터 별도의 허가를 받으면 이러한 조건들은 적용되지 않습니다.

저작권법에 따른 이용자의 권리는 위의 내용에 의하여 영향을 받지 않습니다.

이것은 [이용허락규약\(Legal Code\)](#)을 이해하기 쉽게 요약한 것입니다.

[Disclaimer](#)

Doctor of Philosophy

**Synthesis of carbon-based nanomaterials and composites
toward energy storage applications**

The Graduate School of the University of Ulsan

Department of Chemical Engineering

Di Liu

**Synthesis of carbon-based nanomaterials and composites
toward energy storage applications**

Supervisor: Won Mook Choi

A Dissertation

Submitted to

The Graduate School of the University of Ulsan

In partial Fulfillment of the Requirements

for the Degree of

Doctor of Philosophy

By

Di Liu

Department of Chemical Engineering

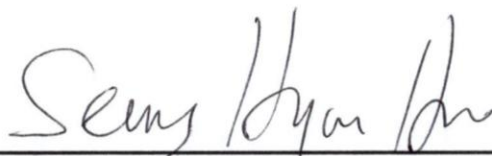
University of Ulsan, Korea

August 2021

**Synthesis of carbon-based nanomaterials and composites
toward energy storage applications**

This certifies that the dissertation

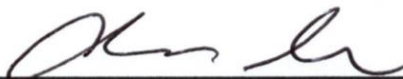
of Di Liu is approved



Committee Chair Prof. Seung Hyun Hur



Committee Member Prof. Sung Gu Kang



Committee Member Prof. Jin Suk Chung



Committee Member Prof. Won Mook Choi



Committee Member Prof. Mun Ho Kim

Department of Chemical Engineering

University of Ulsan, Korea

August 2021

ACKNOWLEDGMENT

This thesis condenses the careful guidance, enthusiastic help and ardent care of tutor, relatives and friends, I would like to extend my sincerest thanks to them.

First, I would like to extend my heartfelt thanks to my tutor Prof. Won Mook Choi. Over the years, my tutor has given careful guidance to my experiment, papers and thesis, and he also put forward some strict requirements. During the period of PhD's study, Prof. Choi provide me with a superior learning and research environment, created a free, harmonious and relaxed academic atmosphere, as well as numerous academic communication opportunities, and broadened my academic horizons.

I would also like to thank my committee members including Prof. Won Mook Choi, Prof. Chung Jin Suk, Prof. Hur Seung Hyun for taking time out of their busy schedule to serve in my committee, review my dissertation and provide valuable comments and suggestions on the work. I would also like to thank Prof. Oh Eun Suok for providing the electrochemical measuring instrument for me to use. And I am thankful to other professors in department of Chemical Engineering for their dedication in experience and knowledge.

I would like to specially thank all members of Flexible and Nano material Laboratory and other friends who kindly helped and shared their knowledge and living experience when I stayed in Korea.

Finally, I deeply would like to thank my family. Their understanding and support made me firm my choice and devote myself to my studies. Their selfless love and tolerance are the strong backing and driving force for my growth. Home is always the warmest harbor and the home of the soul. I hope that I can gain a foothold in society as soon as possible and repay them.

PUBLICATION LIST

1. Di Liu and Won Mook Choi. Hierarchical hollow urchin-like structured MnO₂ microsphere/carbon nanofiber composites as anode materials for Li-ion batteries[J]. Current Applied Physics, 2019, 19(6): 768-774.

2. Di Liu, Seung Hyun Hur, Jin Suk Chung and Won Mook Choi. Fabrication of g-C₃N₄ Quantum Dots/MnCO₃ Nanocomposite on Carbon Cloth for Flexible Supercapacitor Electrode[J]. Applied Sciences, 2020, 10(21): 7927.

3. Di Liu, Seung Hyun Hur, Jin Suk Chung and Won Mook Choi. Synergistically enhanced activity of g-C₃N₄ quantum dots /graphene hydrogel composites for symmetric supercapacitors. Finished the manuscript.

4. Di Liu, Seung Hyun Hur, Jin Suk Chung and Won Mook Choi. Facile synthesis of boron nitride quantum dots decorated ZnO nanoparticle photocatalyst for the degradation of methylene blue and methyl orange. Finished the manuscript.

5. Di Liu, Seung Hyun Hur, Jin Suk Chung and Won Mook Choi. Facile preparation of N-GQDs doped MnCO₃/ZnMn₂O₄ growing on Ni foam composites for high-performance supercapacitor electrodes. Manuscript under preparation.

ABSTRACT

In this dissertation work, we mainly study the carbon-based nanomaterials and composites for energy storage applications, like anode materials for Li-ion materials and electrode materials for supercapacitors.

Urchin-like MnO_2 /carbon nanofiber composites was prepared for anode materials of Li-ion battery, The carbon nanofibers (CNFs) are uniformly deposited on u- MnO_2 to improve the electrical conductivity and to utilize the hierarchical architecture of u- MnO_2 . As the anode electrode of Li-ion batteries, the u- MnO_2 /CNFs nanocomposites exhibit an comparable cycle performance of 988 mAh g^{-1} after 100 cycles with a good rate capability. The superior electrochemical performances of the u- MnO_2 /CNFs nanocomposites can be attributed to the hierarchical urchin-like structures and the superior electrical conductivity of the nanocomposites, which can facilitate fast electron and ion transport and accommodate a large volume change during charge/discharge.

Then obtained q-MC//CC composite is employed as a binder-free electrode of supercapacitor. The g- C_3N_4 quantum dots could effectively enhance the interface electrical conductivity and ion transportation of MnCO_3 electrode, which results in superior electrochemical performances. The q-MC//CC electrode delivers a high specific capacity of 1001 F g^{-1} at a current density of 1 A g^{-1} and a good cycling stability of 96% capacity retention after 5000 cycles. Moreover, asymmetric flexible supercapacitor (ASC) are assembled with q-MC//CC as a positive electrode and carbon cloth as a negative electrode, which exhibits a high energy density of 27.1 Wh kg^{-1} at a power density of 500 W kg^{-1} . Also, the fabricated ASC device demonstrates to power the light-emitting diode effectively under mechanical bending.

Also, as electrode materials of supercapacitors, GH-CN (graphene hydrogel-g- C_3N_4 quantum dots) composites were prepared by hydrothermal method. The results demonstrated that the addition of g- C_3N_4 QDs into graphene hydrogel improved the electrochemical performance distinctly, because the nitrogen-riched quantum dots embedded in graphene hydrogel which has high theoretically surface area, the quantum dots can provide more active sites for faradic reactions, then

promote ion diffusion\transport capability at the electrode/electrolyte interface and enhance the faradic reaction and electron transfer, leading to the observed increased capacitance. The symmetric supercapacitor (SSC) was assembled using GH-2.5CN as positive electrode and negative electrode. The assembled SSC exhibited a high energy density of 22.5 Wh kg^{-1} at 250 W kg^{-1} , and illuminated a red light-emitting diode (LED). It also exhibited excellent flexibility and reached 83.3% capacitance retention after 15000 cycles at 5 A g^{-1} . These results demonstrate the potential GH-CN as a next-generation electrode material for energy storage system.

The novel hierarchical N-GQDs/MnCO₃/ZnMn₂O₄ (N/MC/ZM) composite was grown directly on Ni foam by simple hydrothermal method followed by calcinations treatment for applications as high rate electrodes in supercapacitors. The N/MC/ZM composites exhibited excellent electrochemical properties, including a high specific capacitance of 960.6 F g^{-1} , as well as better cycling stability than MC/ZM (450.3 F g^{-1}). The homogenously dispersed N-GQDs can increase the conductivity and activity sites. Results clearly indicate that the combination of N-GQDs and MC/ZM can constitute a promising binary metal-based electrode material with superior supercapacitive performance, which can provide an alternative to design the quantum dots decorated novel binary metal compounds materials with simple methods for a wide variety of energy storage devices such as supercapacitors, batteries.

TABLE OF CONTENTS

ACKNOWLEDGMENT	I
PUBLICATION LIST	II
ABSTRACT.....	III
TABLE OF CONTENTS.....	V
LIST OF FIGURES.....	VIII
LIST OF TABLES.....	XIV
CHAPTER 1: Introduction	1
1.1 Lithium ion battery	2
1.1.1 Electrode materials of Li-ion battery	4
1.1.1.1 Cathod materials	4
1.1.1.2 Anode materials	6
1.2 Supercapacitors.....	10
1.2.1 Electrode materials of capacitors	12
1.2.1.1 Carbon based materials	12
1.2.1.2 Metal oxide.....	15
1.2.1.3 Polymers.....	16
1.3 Research objectives.....	17
1.4 References	18
CHAPTER 2. Hierarchical hollow urchin-like structured MnO ₂ microsphere/carbon nanofiber composites as anode materials for Li-ion batteries	25
2.1 Introduction	25
2.2 Experimental.....	27
2.3 Characterization.....	27
2.4 Electrochemical measurement.....	28
2.5 Results and discussion	28
2.6 Conclusion.....	42
2.7 References	42

CHAPTER 3 Fabrication of g-C ₃ N ₄ quantum dots/MnCO ₃ nanocomposite on carbon cloth as a binder-free electrode for supercapacitors.....	45
3.1 Introduction	45
3.2 Materials and Methods.....	47
3.2.1 Preparation of g-C ₃ N ₄ Quantum Dots	47
3.2.2 Synthesis of q-MC//CC Nanocomposites.....	47
3.3 Characterization.....	48
3.4 Electrochemical Measurement	48
3.5 Results and discussion	49
3.6 Conclusions	61
3.7 References	62
CHAPTER 4 Synergistically enhanced activity of C ₃ N ₄ quantum dots /graphene hydrogel composites for symmetric supercapacitors	64
4.1 Introduction	64
4.2 Experimental.....	66
4.2.1 Preparation of g-C ₃ N ₄ quantum dots.....	66
4.2.2 Preparation of GH and GH-CN composites	66
4.3 Characterization.....	67
4.4 Electrochemical measurement.....	67
4.5 Results and discussion	68
4.6 Conclusion.....	84
4.7 References	84
CHAPTER 5 Facile preparation of N-GQDs doped MnCO ₃ /ZnMn ₂ O ₄ growing on Ni foam composites for high-performance supercapacitor electrodes.....	87
5.1 Introduction	87
5.2 Materials and methods	89
5.2.1 Chemicals	89
5.2.2 Synthesis of N-GQDs.....	89
5.2.3 Fabrication of MnCO ₃ /ZnMn ₂ O ₄ and N-GQDs/ MnCO ₃ /ZnMn ₂ O ₄ ..	89
5.2.4 Materials characterization.....	90
5.2.5 Electrochemical measurements.....	90

5.3 Results and discussion	92
5.4 Conclusion.....	104
5.5 References	104
CHAPTER 6 Other work.....	107
Facile synthesis of boron nitride quantum dots doped ZnO nanoparticle photocatalyst with efficiently enhanced photocatalytic degradation of methylene blue and methyl orange.....	107
6.1 Introduction	107
6.2 Experimental.....	109
6.2.1 Materials	109
6.2.2 Preparation of ZnO nanoparticles	109
6.2.3 Preparation of boron nitride quantum dots	110
6.2.4 Preparation of ZnO-BN photocatalysts	110
6.2.5 Characterization	110
6.2.6 Photocatalytic activity measurement.....	111
6.3 Results and discussion	112
6.3.1 Characterization of the products	112
6.3.2 Evaluation of photocatalytic activity.....	118
6.3.3 Mechanism of photocatalytic degradation.....	126
6.4 Conclusion.....	128
6.5 References	128
CHAPTER 7 Summary and recommendations for future work	131
7.1 Summary	131
7.2 Recommendations for future work	132

LIST OF FIGURES

Fig. 1-1 Energy Storage Ragone plot (reproduced from [2]).....	2
Fig. 1-2 Scheme of a common lithium-ion battery.....	6
Fig. 1-3 Schematic illustration of active anode materials for the next-generation lithium batteries. Potential (vs. Li/Li^+) and the corresponding capacity density are shown.....	8
Fig. 1-4 Schematic illustration of three different types of anodes based on the lithium storage mechanism and their advantages and disadvantages	10
Fig. 1-5 Ragone plot. Detail window shows energy drop due to internal dissipation and leakage losses for sufficiently high and low power [63]	12
Fig. 2-1(a) FE-SEM image and (b) TEM image of u- MnO_2 microspheres. (c) FE-SEM image and (d) TEM image of nanotubes of u- MnO_2	29
Fig. 2-2 N_2 adsorption/desorption isotherms for bare u- MnO_2 and u- MnO_2/CNFs composite.....	31
Fig. 2-3 XRD patterns of the obtained u- MnO_2	31
Fig. 2-4 FE-SEM image of the obtained MnO_2 products at the different hydrothermal reaction time. (a) 1 hr, (b) 2 hr, (c) 3 hr, and (d) 4 hr.	32
Fig. 2-5 Low magnified FE-SEM image of the obtained MnO_2 products at the different hydrothermal reaction time. (a) 1 hr, (b) 2 hr, (c) 3 hr, and (d) 4 hr. (scale bar is 1 μm).....	32
Fig. 2-6 TEM images of the obtained MnO_2 products at the different hydrothermal reaction time. (a) 1 hr, (b) 2 hr, and (c) 3 hr. (scale bar is 1 μm).....	33
Fig. 2-7 (a) FE-SEM image of the u- MnO_2 products after 8 h of hydrothermal reaction time and (b) its high magnified image. (scale bar is 1 μm)	33
Fig. 2-8 (a) XRD patterns of the obtained MnO_2 products at the different hydrothermal reaction time. (b) Schematic illustration of the morphological evolution of u- MnO_2 microsphere.	34
Fig. 2-9 FE-SEM image of CNFs.....	34
Fig. 2-10 (a) FE-SEM image of the u- MnO_2/CNFs nanocomposite, and corresponding quantitative EDS element mapping of (b) Mn, (c) O and (d) C.	

.....	35
Fig. 2-11 (a) FT-IR spectra and (b) XRD patterns for CNFs, u-MnO ₂ , and u-MnO ₂ /CNFs composite.....	37
Fig. 2-12 TGA curve of the u-MnO ₂ /CNFs composite.....	37
Fig. 2-13 The first four CV curves of (a) bare u-MnO ₂ and (b) u-MnO ₂ /CNFs nanocomposite. Charge-discharge curves at 0.1 C of (c) bare u-MnO ₂ and (d) u-MnO ₂ /CNFs nanocomposite.	38
Fig. 2-14 (a) The cycle performance and (b) the rate performance of bare u-MnO ₂ , u-MnO ₂ /CNFs nanocomposite, and p-MnO ₂ /CNFs nanocomposite.	38
Fig. 2-15 The cycle performance from 100 to 200 cycles for the u-MnO ₂ /CNFs composite.....	40
Fig. 2-16 (a-b) FE-SEM images of the u-MnO ₂ /CNFs electrode after 100 cycles test.....	40
Fig. 2-17 (a) Nyquist plots with inset of equivalent circuit of bare u-MnO ₂ , u-MnO ₂ /CNFs nanocomposite, and p-MnO ₂ /CNFs nanocomposite, and (b) its magnified plots.....	41
Fig. 2-18 (a-b) FE-SEM images of the p-MnO ₂ /CNFs nanocomposites.....	41
Fig. 3-1 Schematic illustration for the synthesis of g-C ₃ N ₄ quantum dots/MnCO ₃ nanocomposite on carbon cloth.	48
Fig. 3-2 (a-b) SEM images of q-MC//CC. (c) TEM image of q-MC//CC and (d) its high magnification image. (d) EDS elementary mapping of q-MC//CC. ...	50
Fig. 3-3 (a-b) SEM images of as-synthesized MC//CC.....	51
Fig. 3-4 High resolution C 1s XPS spectrum of MC//CC.....	51
Fig. 3-5 (a) The XPS survey scan of q-MC//CC and MC//CC. (b-d) High resolution XPS spectrum of Mn 2p, C 1s, and N 1s of q-MC//CC, respectively.	52
Fig. 3-6 Image of the contact angle measurement of (a) MC//CC and (b) q-MC//CC with 1M Na ₂ SO ₄ electrolyte.....	52
Fig. 3-7 FT-IR spectrum for q-MC//CC and MC//CC.....	53
Fig. 3-8 N ₂ adsorption/desorption isotherms for CC and q-MC//CC composite	53
Fig. 3-9 (a) CV curves of q-MC//CC and MC//CC. (b) CV curves of q-MC//CC at	

different scan rates. (c) Galvanostatic charge-discharge curves of q-MC//CC at different current densities. (d) Obtained specific capacitance of q-MC//CC at different current densities.	54
Fig. 3-10 (a) Nyquist plots of q-MC//CC and MC//CC. (a) Specific capacitance retention of q-MC//CC and MC//CC along 5000 cycles (insets show their SEM images after cycle test).	56
Fig. 3-11 (a) Schematic illustration of all-solid-state ASC using q-MC//CC electrode. (b) CV curves at different scan rates and (c) galvanostatic charge-discharge curves at different current densities of q-MC//CC based ASC. (d) The Ragone plots of q-MC//CC based ASC and reported Mn-based supercapacitors. (e) CV curves of the q-MC//CC based ASC under mechanical bending. (f) Photo image of lighting LED powered by q-MC//CC based ASC under flat and bent state.	58
Fig. 4-1 Synthesis of GH-CN composites as the electrode materials for symmetric supercapacitor.	69
Fig. 4-2 (a) XRD results and (b) FTIR patterns of GH and GH-CN composites.	70
Fig. 4-3 (a) SEM images of GH; (b,c) GH-2.5CN composites; (d-g) SEM image and elemental mapping for GH-2.5CN composites; (h,i) EDS measurement of the plotted area and the elemental distribution of GH-2.5CN composites.	71
Fig. 4-4 SEM images of GH	72
Fig. 4-5 (a) TEM image of the GH nanostructure; (b) TEM image of GH-2.5CN ; (c) the size distribution of g-C ₃ N ₄ QDs on graphene hydrogel from (b); (d) HRTEM image of GH-2.5CN.....	72
Fig. 4-6 TEM images of GH-2.5CN.....	73
Fig. 4-7 (a) XPS survey spectra of GH and GH-2.5CN samples; (b) N 1s of GH-2.5CN; (c) C 1s of GH; (d) C 1s of GH-2.5CN.....	74
Fig. 4-8 Nitrogen adsorption-desorption isotherms and pore size distribution plots of GH (a), GH-1CN (b), GH-2.5CN (c) and GH-5CN (d).....	75
Fig. 4-9 Electrochemical performance of GH, GH-1CN, GH-2.5CN and GH-5CN electrodes in 6M KOH electrolyte using a three-electrode system. (a) Cyclic	

	voltammetry curves of different electrodes at a scan rate of 5 mV s ⁻¹ ; (b) Galvanostatic charge-discharge curves of different electrodes at 0.2 A g ⁻¹ ; (c) CV curves of GH-2.5CN at different scan rates from 5 to 100 mV s ⁻¹ ; (d) GCD curves of GH-2.5CN at different current density from 0.2 to 1.5 A g ⁻¹ ; (e) The specific capacitance at different current densities of all samples; (f) Electrochemical impedance spectroscopy (EIS) of the different electrodes (insert: the EIS in the region of high frequency).	77
Fig. 4-10	(a) CV curves of GH at different scan rates from 5 to 100 mV s ⁻¹ ; (b) GCD curves of GH-2.5CN at different current density from 0.2 to 1.5 A g ⁻¹	79
Fig. 4-11	Two-electrode electrochemical performance of GH-CN//GH-CN solid-state symmetric supercapacitor (SSC) in KOH/PVA electrolyte. (a) CV curves of the device at various scan rates from 5 to 100 mV s ⁻¹ (insert are the photograph of device and schematic diagram); (b) GCD curves of the device at different current density from 0.5 to 5 A g ⁻¹ ; (c) CV curves of the device under different bending conditions at a scan rate of 50 mV s ⁻¹ (insert are photographs of the device under different bending conditions) (d) Cycling test of the device over 15000 cycles at a current density of 5 A g ⁻¹ (insert is the charge/discharge profiles at the rate of 5 A g ⁻¹); (e) Ragone plot of the device derived from the GCD curves and other results from the literatures; (f) The photograph of the device connected in series lighting the red LED.	82
Fig. 5-1	(a) XRD patterns for the prepared MC/ZM composites, MC/ZM on Ni foam and Ni foam; (b) XRD patterns for MC/ZM (enlarged degree).	92
Fig.5-2	SEM images in different magnifications : (a) Ni foam; (b-d) hierarchical N/MC/ZM on Ni foam; (e-i) EDS elemental mapping images (of Fig.5-2d).	93
Fig.5-3	(a) SEM image of MC/ZM on Ni foam; (b-e) EDS elemental mapping images of Fig.5-3a; (f) EDS spectrum of MC/ZM on Ni foam.	94
Fig.5-4	(a)TEM image of N-GQDs (insert: the HRTEM of N-GQDs) ; (b) the size-distribution of N-GQDs; (c) TEM and (d) HRTEM images of N/MC/ZM composite (insert: corresponding SAED patterns of N/MC/ZM composite).	

.....	95
Fig.5-5. (a) XPS survey spectra (b) Zn 2p (c) Mn 2p (d) O 1s (e) C 1s (f) N 1s of N/MC/ZM sample.....	96
Fig.5-6 (a) CV curves of MC/ZM and N/MC/ZM electrodes at the scan rate of 5 mV/s in 1.0 M KOH electrolyte; (b) GCD curves of MC/ZM and N/MC/ZM electrodes at 1 A g ⁻¹ current density; (c) CV curves of N/MC/ZM electrode at different scan rates of 5-100 mV s ⁻¹ ; (d) GCD curves of N/MC/ZM electrode at different current densities of 1-10 A g ⁻¹ ; (e) the specific capacitance of MC/ZM and N/MC/ZM electrodes at different current densities derived from GCD; (f) Nyquist plots of MC/ZM and N/MC/ZM electrodes in 1.0 M KOH electrolyte and its equivalent circuit model (insert shows the curves obtained in the high frequency region); (g) cycling performance of MC/ZM and N/MC/ZM at 5A g ⁻¹	98
Fig.5-7. (a) CV curves of MC/ZM at different scan rates and (b) GCD curves of MC/ZM at different current densities.	99
Fig.5-8. Two-electrode electrochemical performance of N/MC/ZM//MC/ZM solid-state asymmetric supercapacitor (ASC) in KOH/PVA electrolyte. (a) Schematic illustration of flexible solid-state N/MC/ZM//MC/ZM asymmetric supercapacitor. (b) CV curves and (c) GCD curves of the device. (d) GCD curves of the devices collected at different potential windows at a fixed current density of 1 A g ⁻¹ . (e) CV curves under different bending conditions at 50 mV s ⁻¹ . (f) Ragone plots of the device (insert is the photographs of LED light powered by the device).....	103
Fig.6-1. (a) XRD patterns and (b) FTIR spectra of the synthesized ZnO and ZnO-BN composites.	112
Fig.6-2. SEM images of ZnO nanoparticles (a,b), and ZnO-4BN composites (c,d); SEM image and elemental mapping for ZnO-4BN composites (e-j); EDS measurement of the plotted area and the elemental distribution of ZnO-4BN composites (k,l).....	113
Fig.6-3. TEM images of BNQDs (a) and ZnO-4BN composites (b-d) (insert, HRTEM of BNQDs).	114

Fig.6-4. XPS spectra of ZnO and ZnO-4BN samples: (a) total survey, (b) Zn 2p, (c) C1s of ZnO, (d) C1s of ZnO-4BN, (e) N 1s of ZnO-4BN and (f) B 1s of ZnO-4BN.....	115
Fig.6-5. (a) UV-vis and (b) PL spectra of ZnO and ZnO-BN composites with different fluencies. The insert picture displays the corresponding $(\alpha h\nu)^2$ versus $h\nu$ plots.	116
Fig.6-6. The photocatalytic activities of ZnO and ZnO-BN composites for degradation of (a) MB and (b) MO under UV light irradiation; Degradation efficiencies of (c) MB and (d) MO under UV light irradiation for different samples; Pseudo first-order kinetic fitting curves and the corresponding apparent rate constants for (e) MB and (f) MO degradation.	118
Fig.6-7. Adsorption properties of the synthesized photocatalysts for MB (a) and MO (b) degradation in the dark respectively.	121
Fig.6-8. UV-vis spectra of MB (a) and MO (b) degradation in the presence of ZnO-4BN composite depends on irradiation time.	121
Fig.6-9. photographs of MB and MO aqueous solution in the presence of ZnO (a) and ZnO-4BN (b) depends on irradiation time.....	122
Fig.6-10. The species trapping experiment for degradation curve and efficiencies of MB (a,b) and MO (c,d) over ZnO-4BN sample under UV light irradiation.	124
Fig.6-11. The recycled photocatalytic experiments of ZnO-4BN sample for degradation of MB (a) and MO (b) under UV light irradiation.....	125
Fig.6-12. Schematic illustration of the possible photocatalytic processes in ZnO-BN of MB and MO degradation.	126
Fig.6-13. zeta-potential of BNQDs (a) and ZnO (b) dispersed in 10 ml (10 mg) of ethanol with sonication 20 minutes.....	126

LIST OF TABLES

Table 3-1 Comparison of the electrochemical performance of q-MC//CC with previous reports.	59
Table 4-1 Specific capacitance of as-prepared electrodes at different scan rate .	80
Table 4-2 Specific capacitance of as-prepared electrodes at different current density.	80
Table 4-3 Comparison of the specific capacitance, potential window, and experimental conditions of the reported supercapacitor electrodes made of graphene hydrogel-based and carbon-based materials measured in 3 electrodes system to our work.	80
Table.5-1 The specific capacitance of different $ZnMn_2O_4$ electrodes.	102
Table.6-1. Photocatalytic degradation of MB with modified ZnO composites under UV light irradiation.	122
Table.6-2. Photocatalytic degradation of MO with modified ZnO composites under UV light irradiation.	123

CHAPTER 1: Introduction

Energy systems play a key role in harvesting energy from various sources and converting it to the energy forms required for applications in various sectors, e.g., utility, industry, building and transportation. Energy sources like fossil fuels can be used to provide energy according to customer demand, i.e. they are readily storable when not required. But other sources such as solar and wind energy need to be harvested when available and stored until needed. Applying energy storage can provide several advantages for energy systems, such as permitting increased penetration of renewable energy and better economic performance. Also, energy storage is important to electrical systems, allowing for load leveling and peak shaving, frequency regulation, damping energy oscillations, and improving power quality and reliability.

Many types of energy storage systems exist, and they can be categorized in various ways. For example, storage characteristics of electrochemical energy storage types, in terms of specific energy and specific power, are often presented in a ‘Ragone plot’ [1], which helps identify the potentials of each storage type and contrast them for applications requiring varying energy storage capacities and on-demand energy extraction rates. The plot also aids in selecting the most appropriate energy storage for specific applications or needs (Fig.1-1). Storage energy density is the energy accumulated per unit volume or mass, and power density is the energy transfer rate per unit volume or mass. When generated energy is not available for a long duration, a high energy density device that can store large amounts of energy is required. When the discharge period is short, as for devices with charge/discharge fluctuations over short periods, a high power density device is needed. Energy storage systems also can be classified based on storage period. Note that only a few energy storage types are shown in Fig. 1-1 as the Ragone plot is traditionally used only for batteries, capacitors and fuel cells.

Electrical energy can be stored electrochemically in batteries and capacitors. Batteries are mature energy storage devices with high energy densities and high voltages. Various types exist including lithiumion (Li-ion), sodium-sulphur (NaS),

nickel-cadmium (NiCd), lead acid (Pb-acid), lead-carbon batteries, as well as zebra batteries (Na-NiCl₂) and flow batteries. Capacitors store and deliver energy electrochemically, and can be classified as electrostatic capacitors, electrolytic capacitors, and electrochemical capacitors. Among these three types, electrochemical capacitors, also called supercapacitors or ultracapacitors (UCs), have the greatest capacitance per unit volume due to having a porous electrode structure.

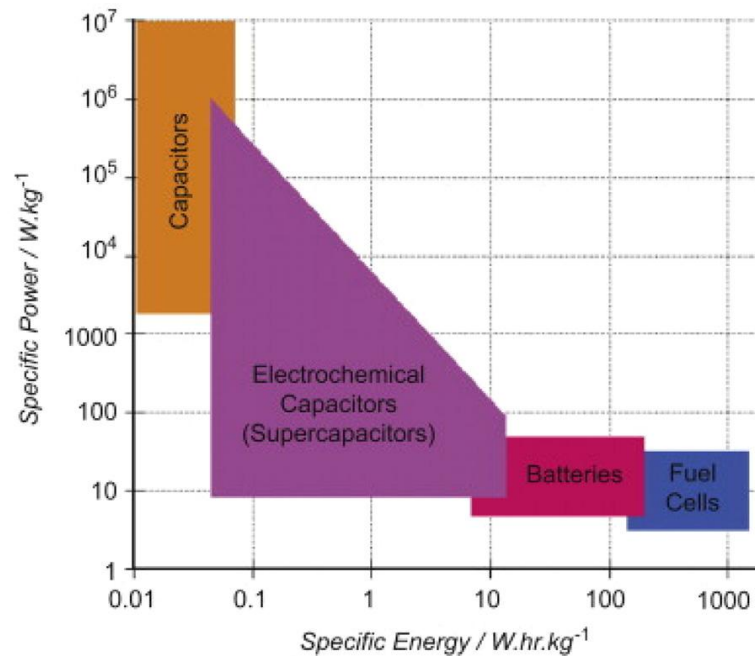


Fig. 1-1 Energy Storage Ragone plot (reproduced from [2])

1.1 Lithium ion battery

Among the various battery types, Li-ion batteries have an unmatched combination of high energy and power density, making it the technology of choice for portable electronics, power tools, and hybrid/full electric vehicles [3]. If electric vehicles (EVs) replace the majority of gasoline powered transportation, Li-ion batteries will significantly reduce green house gas emissions [4]. The high energy efficiency of Li ion batteries may also allow their use in various electric grid applications, including improving the quality of energy harvested from wind, solar, geo-thermal and other renewable sources, thus contributing to their more widespread use and building an

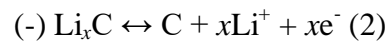
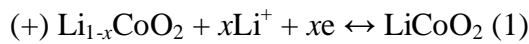
energy-sustainable economy. Therefore Li-ion batteries are of intense interest from both industry and government funding agencies, and research in this field has abounded in the recent years.

A charged Li-air battery provides an energy source for electric vehicles rivaling that of gasoline in terms of usable energy density. The fundamental battery chemistry during discharge is the electrochemical oxidation of lithium metal at the anode and the reduction of oxygen from air at the cathode. Before Li-air batteries can achieve high performance and become commercially viable, numerous technical challenges need to be addressed: designing cathode structures, optimizing electrolyte compositions and elucidating the complex chemical reactions during charge and discharge [5-7]. The most significant developments and the main limiting factors for Li-air batteries, as well as the current understanding of their chemistry, have been summarized in the literature [5,6]. The Li-ion battery is a type of lithium battery that uses an intercalated lithium compound as an electrode material. Bruce et al.[8] examine the energy that can be stored in Li-air (based on aqueous or non-aqueous electrolytes) and lithium-sulfur (Li-S) batteries and compare it with that for Li-ion batteries, and discuss cell operation and development challenges. They suggest that both batteries offer improved energy density compared to Li-ion batteries and could also be more cost-competitive than Li-ion batteries. However, they suggest that more research on the fundamental chemistry involved in the Li-O₂ and Li-S cells is needed before they can reach markets. Thackeray et al.[9] provide a historical overview of lithium-ion batteries, the status of current ones, and a description of advances in lithium-air batteries. The performance of Li-ion batteries is affected by the solid electrolyte interphase, a protecting layer formed on the negative electrode of the battery due to electrolyte decomposition during the first charge-discharge cycle. Factors that affect the solid electrolyte interphase and how they impact battery performance are discussed by Verma et al. [10]. Janek and Zeier [11] suggest that the energy density of conventional Li-ion batteries will soon reach a physicochemical limit and solid-state batteries that use solid electrolytes instead of liquid ones could meet the need for higher energy and power densities, although technical issues such as slow kinetics limit commercialization of solid-state systems.

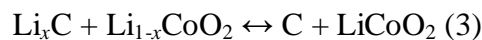
1.1.1 Electrode materials of Li-ion battery

1.1.1.1 Cathod materials

The existing concept of present lithium-ion batteries is based on the combination of a lithium-ion positive electrode “cathode” and a negative electrode “anode” with these being separated by a membrane soaked with a lithium-ion conducting electrolyte, for example a solution of LiPF_6 in alkyl organic carbonates, as schematically shown in Fig.1-2. Lithium transition metal oxides or phosphates (LiCoO_2 , LiMn_2O_4 , $\text{LiNi}_{1/3}\text{Co}_{1/3}\text{Mn}_{1/3}\text{O}_2$, LiFePO_4 , $\text{LiNi}_{0.8}\text{Co}_{0.15}\text{Al}_{0.05}\text{O}_2$ (NCA), etc.) are generally adopted as the active cathode materials of the commercial lithium-ion batteries [12-15]. At the anode side, graphite is the common choice [16]. During charge of the cell, lithium ions move out of the cathode ($\text{Li}_{1-x}\text{CoO}_2$) and become trapped inside the anode (Li_xC_6) when external electrical current is applied, through which the electrical energy is converted to chemical energy. Upon the cell discharge, those lithium ions travel back to the cathode and release the chemical energy stored via producing an external electrical current. The electrochemical reactions occurring in a typical lithium-ion battery based on LiCoO_2 cathode and graphite anode can be described as follows:



Overall reaction:



The reversible flow of lithium ions moving back and forth through the ionically conducting electrolyte between two electrodes allows the conversion of chemical energy and electrical energy repeatedly. During the initial battery cycling (charge/discharge), multicomponent (organic/inorganic) and multilayer passivation films form at each electrode known as solid electrolyte interphase (SEI) that is critical to protecting the electrodes from further reactions with electrolytes. Although such lithium-ion batteries are commercially very successful, we must realize that we are reaching the limits in performance using the current electrode and electrolyte

materials [17]. The performance limitation together with the cost concern of the commercially available Li-ion batteries seriously limits the fast expansion of the electrical vehicle market and efficient usage of renewable energy sources. In addition, some other technical bottlenecks of the current Li-ion technology including slow recharge cycles, relatively short calendar life as well as the safety issues need to be fully addressed.

Significant research has been conducted to exploring higher energy density electrode materials in order to meet the requirement for EV's application. Currently, LiCoO_2 [18], layered metal oxides such as $\text{LiNi}_{0.8}\text{Co}_{0.15}\text{Al}_{0.05}\text{O}_2$ (NCA) [19,20] and $\text{LiNi}_{1/3}\text{Co}_{1/3}\text{Mn}_{1/3}\text{O}_2$ (NCM) [21,22], electrode derived from spinel-type LiMn_2O_4 [23] and olivine-type LiFePO_4 [24] are the state of the art for cathode active materials. However, they deliver relatively low practical capacities in a lithium-ion cell, typically in the range of 100–180 mAh g^{-1} at moderate current rates. Clearly, it is important to develop new strategies to design alternative high-energy cathode materials that are superior to those achievable with standard LiCoO_2 , LiMn_2O_4 and LiFePO_4 type electrodes, yet they still have to maintain considerable structural stability, rate capability as well as long cycle life. For example, a family of high-energy manganese based cathode materials have been developed recently by structurally integrating a Li_2MnO_3 stabilizing component into an electrochemically active LiMO_2 (M=Mn, Ni, Co) electrode, which boosts specific capacity up to 250 mAh g^{-1} due to the excess lithium in the system and, thereby, significantly improves the energy density of cell (based on the active materials) to 900 Wh kg^{-1} [25,26]. However, the decay of capacity and voltage of these materials during the long time cycling led to the severe loss of the cell energy density that prevents its practical application in EVs [27,28]. Going beyond the horizon of Li-ion batteries could offer another great opportunity to increase the energy density of the cell, although it requires the exploration of new electrochemistry and materials. For example, sulfur- and oxygen-based cathodes have recently been intensely investigated due to their potentially much higher theoretical capacity than the conventional lithium metal oxide [29-31]. These systems, however, are still in the early stage and facing a formidable challenge. The science and technology of the development of high-performance cathode materials have been extensively reviewed in

the previous reported papers, to which the reader is referred for more details [22,32-38].

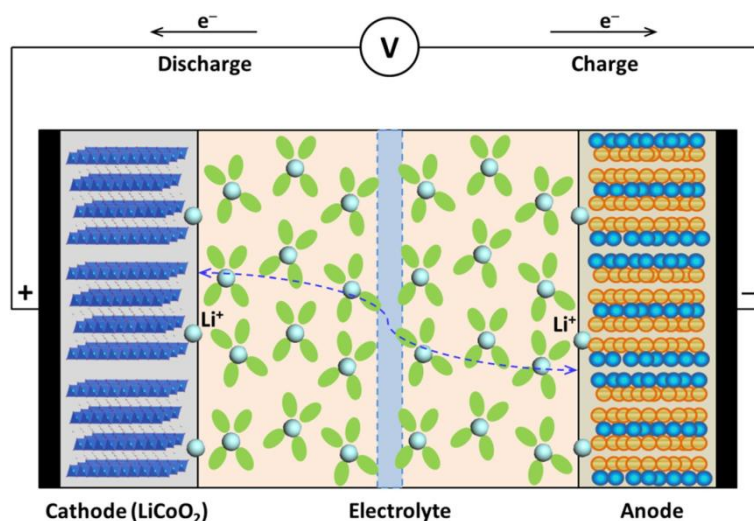


Fig. 1-2 Scheme of a common lithium-ion battery

1.1.1.2 Anode materials

Another effective approach of increasing the energy density of lithium-ion batteries is to search for high-capacity anode materials. As mentioned earlier, graphite is definitely the most widely used anode active material in the commercial Li-ion cells thanks to its excellent features including low working potential, low cost and good cycle life [39]. However, graphite only delivers a relatively low capacity of 372mAh g^{-1} since it allows the intercalation of only one lithium for six carbon atoms forming a stoichiometric LiC_6 , as shown in reaction 2. In addition, battery with graphite anode usually has moderate power density due to the relatively slow diffusion rate of lithium ion into carbon materials (between 10^{-12} and $10^{-6}\text{ cm}^2\text{ s}^{-1}$) [40]. Therefore, there is an urgency to find alternative anode materials with high-capacity and high lithium-ion diffusion rate that could help to improve the energy and power densities of the cell. During the past decade, numerous efforts have been devoted to this blooming field with significant progress being achieved; yet there is still a sizable challenge facing those involved in the design and development of high-performance anode materials.

An ideal anode for Li-ion battery should fulfill the requirement of high reversible

gravimetric and volumetric capacity; a low potential against cathode materials; high-rate capability; long cycle life; low cost; excellent abuse tolerance; and environmental compatibility. Pure lithium metal is clearly the best anode material since it does not carry any dead weight, if taking the specific capacity into account alone. However, the electroplating of dendritic lithium during charging can cause an internal short circuit, leading to severe safety concerns. Both carbon and non-carbon materials for high-performance anode have been intensively investigated [41], including but not limiting to carbon nanotubes [42,43], carbon nanofibers [44], graphene [45-47], porous carbon [48], silicon [49] and silicon monoxide [50,51], germanium [52,53], tin [54,55], and transition metal oxides [56,57], sulfides [58], phosphides [50] and nitrides [58,59]. The redox potentials versus Li/Li^+ and the corresponding specific capacity of these materials are shown in Fig.1-3, which clearly shows that the selection of suitable anode materials has significant impact on improving energy density of the Li-ion cell.

Based on their electrochemical lithiation/delithiation mechanism, the innovative anode materials discussed in this review can be classified into three main groups as shown in Fig.1-4, i.e., intercalation anodes, carbon-based materials and $\text{Li}_4\text{Ti}_5\text{O}_{12}$; alloy anodes such as Si, Ge, Sn; conversion anodes, mainly referring to transition metal oxides but also including metal sulfides, phosphides and nitrides. Compared to the conventional graphite anode, the above-mentioned materials show great promise in terms of energy density and/or power density (see Fig.1-4). However, it requires significant research efforts in a variety of fields to unlock their full potentials. Fortunately, researchers and industry alike see a great chance in the development of high-performance anode materials with the recent progress in advanced technologies and fundamental understandings.

The need for storage technologies with much greater energy density than the current Li-ion systems for applications such as electrical vehicles and grid storage calls for the search of higher-capacity electrode materials, both cathode and anode, which certainly relies on material breakthroughs. Although notable progress has been achieved in the development of high-performance anode materials for Li-ion batteries, further investigation of the underpinning mechanisms that limit their performance is required in order to aid the rational design and development of kinetically facile and

chemically stable anode materials. As detailed in this review article, we mainly discussed the research activities and achievements of three different types of high-performance anode materials, i.e., intercalation anodes (graphene and $\text{Li}_4\text{Ti}_5\text{O}_{12}$); alloy anodes (Si, Sn, P); conversion oxide anodes; as well as the holy-grail lithium metal anode. Without a doubt, substantial challenges exist for each component, which requires significant research efforts in a variety of fields to unlock their full potentials as the next-generation anode material.

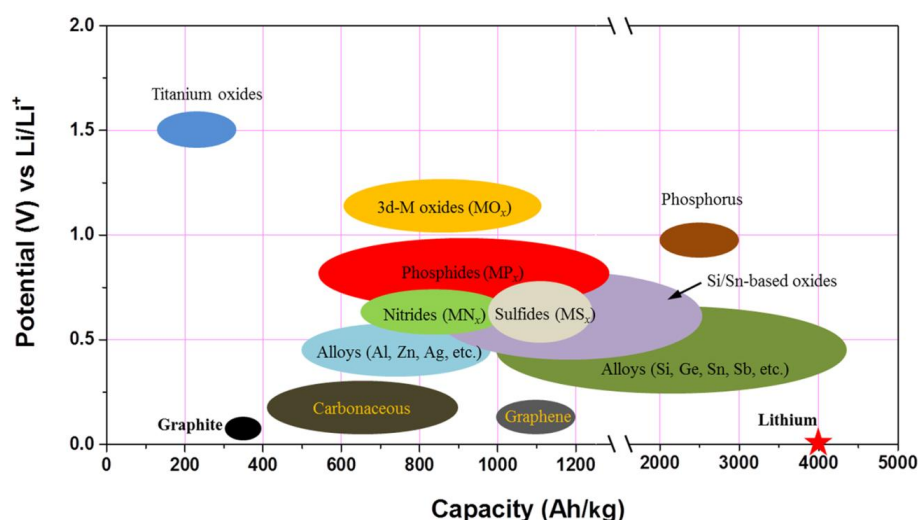


Fig. 1-3 Schematic illustration of active anode materials for the next-generation lithium batteries. Potential (vs. Li/Li^+) and the corresponding capacity density are shown.

Graphene-based materials show some promises; their restacking issue and high irreversible capacity loss during the initial discharge/charge cycle seriously limit their application. Its high surface area leads to low CE and significant consumption of electrolyte, also making it not a practical anode material. However, graphene could be used as a novel support for other anode materials such as silicon, tin or transition metal oxides by taking the advantage of graphene's high surface area, mechanical strength and electrical conductivity. In this sense, further research is needed to find the best combination between the graphene and other materials that will give satisfactory capacity and capacity retention.

Alloy-type materials represented by Si and Sn are the most attractive anode due to their high capacity, but the large volume changes during cycling have been the main

impediment to their implementation. To address this issue, one approach that demonstrates great success is using nanoscale design; however, future research is necessary in the following areas. First, quantitative understanding of the nanoscale design, such as size-dependent of the nanostructure properties, is still needed. Second, the nature of solid electrolyte interface (SEI) layer that has the significant impact on the coulombic efficiency need to be fully investigated. Third, developing of advanced characterization techniques (both in situ and ex situ) together with multiscale modeling and simulation is vital to unravel the detail microscopic processes that occur during lithiation/delithiation, especially at both the atomic level and the electrode surface. Fourth, it is necessary to develop effective method to pack the nanostructured materials into the electrode and understand the deformation mechanism at the whole electrode level. Finally, in terms of the practical application, it is vital to develop large-scale and low-cost fabrication strategies for nanomaterials with desirable performance.

Similar to alloy anodes, the conversion anodes also have the issues of material pulverization at the individual particle level, unstable SEI layer, and the morphology and volume change at the whole electrode level. To enable good cycling performance for the conversion oxides, nanoscale materials design is needed for interconversion of multiple solid phases. Another challenging aspect of conversion anode is the large voltage hysteresis (~ 1 V) between charge/discharge, which needs to be addressed.

Titanium-based materials as the high-power anode showed much improved tolerance to thermal abuse compared with the conventional graphite anode. However, the main drawbacks of this type of materials are low inherent theoretical capacities and low electronic conductivity in bulk materials with micrometer-sized particles. Nanocrystallization, doping or surface doping could potentially solve the issue of low electronic conductivity. The intrinsic gassing issue of LTO is associated with that the lithiated $\text{Li}_{4-x}\text{Ti}_5\text{O}_{12}$ has a tendency to react with non-aqueous electrolyte when aged at elevated temperatures. Resolving the gassing issue would enable the successful deployment of the LTO as highpower anode for HEV applications.

Eventually, enabling the lithium metal electrode would be the ultimate goal for the high-performance anode of the next-generation Li-ion batteries. The challenges of Li metal anodes call for strategies to form a stable interfacial layer with the dual functions

of suppressing the dendrite formation and stop the side chemical reaction. Liquid electrolyte and additives are an important area of research to stabilize Li metal anodes since the formed SEI can have significantly different morphology, composition and properties. Solid electrolytes including polymers and ceramics with strong mechanical property for dendrite suppression would be another interesting direction to go. Finally nanoscale interfacial materials design could be a promising approach to address the Li metal anode problems.

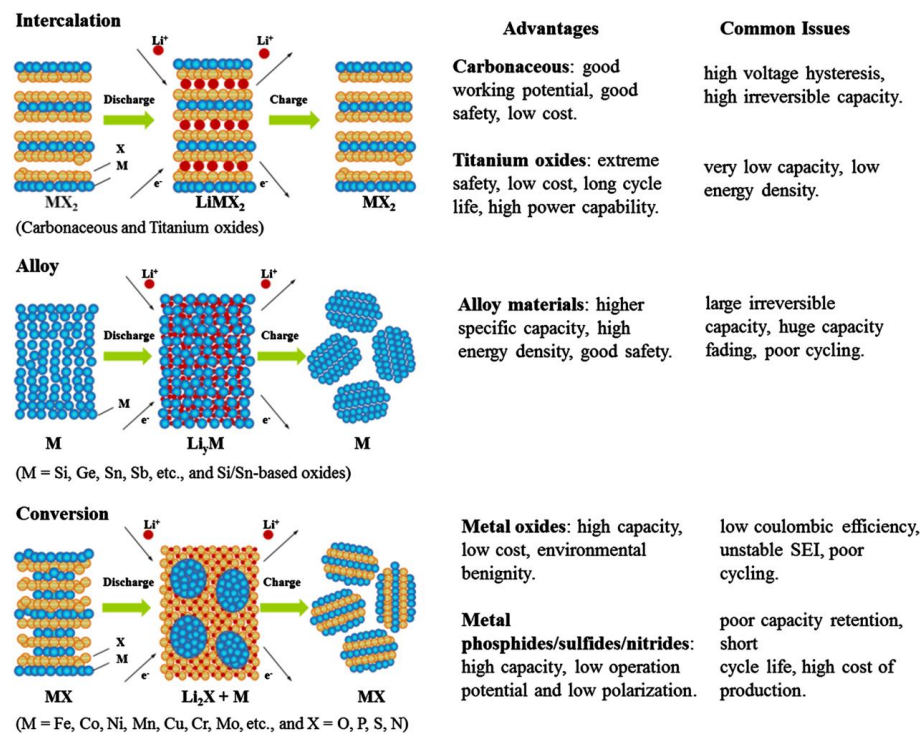


Fig. 1-4 Schematic illustration of three different types of anodes based on the lithium storage mechanism and their advantages and disadvantages

1.2 Supercapacitors

Supercapacitors are devices capable of managing high power rates compared to batteries. Although supercapacitors provide hundred to many thousand times higher power in the same volume [60], they are not able to store the same amount of charge as batteries do, which is usually 3–30 times lower [60]. This makes supercapacitors suitable for those applications in which power bursts are needed, but high energy

storage capacity is not required. Supercapacitors can also be included within a battery based ESS to decouple the power and energy characteristics of the ESS, thus improving the sizing while fulfilling the power and energy requirements, and probably enlarging its lifetime.

The power output of supercapacitors is lower than that of electrolytic capacitors, but can reach about 10 kW kg^{-1} . On the other hand, their specific energy is several orders of magnitude higher than the one of capacitors [61]. These devices are interesting because they fill the gap between aluminum electrolytic capacitors and batteries, which are capable of storing large amounts of energy, but do not offer very high power densities ($<1 \text{ kW kg}^{-1}$) due to their storage mechanism. This can be graphically explained in a Ragone plot, in which the energy and power densities are represented in horizontal and vertical axes, also showing the discharge time of the devices in diagonal lines ($E=Pt$). Different storage technologies are represented in a Ragone plot in Fig.1-5. However, the Ragone plot does not reflect many other performance parameters such as cost, safety and cycle life. They need to be mentioned separately for a complete understanding of advantages and limitations of a particular energy storage technology.

Thus, it is extremely important to note that supercapacitors can not only be discharged in a matter of seconds, but also be charged in such a short time period. This is an important benefit for energy recovery systems, e.g. for dynamic braking of transport systems. Another great advantage of supercapacitors is their cycle life. These devices can withstand millions of cycles thanks to their charge storage mechanism, which does not involve irreversible chemical reactions, storing charges physically at the surface of the electrodes in an electric double layer. This allows exceeding the cycle life of batteries, which are at best capable of withstanding a few thousand cycles. The highly reversible electrostatic storage does not produce changes in the electrode volume, eliminating the swelling occurring in typical redox reactions in the bulk of a battery's active material during charge and discharge cycles. A supercapacitor electrode has no such rate limitations as those of redox battery electrodes due to electrochemical kinetics through a polarization resistance [62]. The main disadvantage related to the charge storage mechanism is the operating voltage of

a supercapacitor cell, which should be kept low in order to avoid the chemical decomposition of electrolytes.

A supercapacitor cell comprises two electrodes with a separator between them. The electrodes can be identical for symmetric cells or different for asymmetric cells. The separator is soaked in electrolyte and prevents the electrical contact between the electrodes.

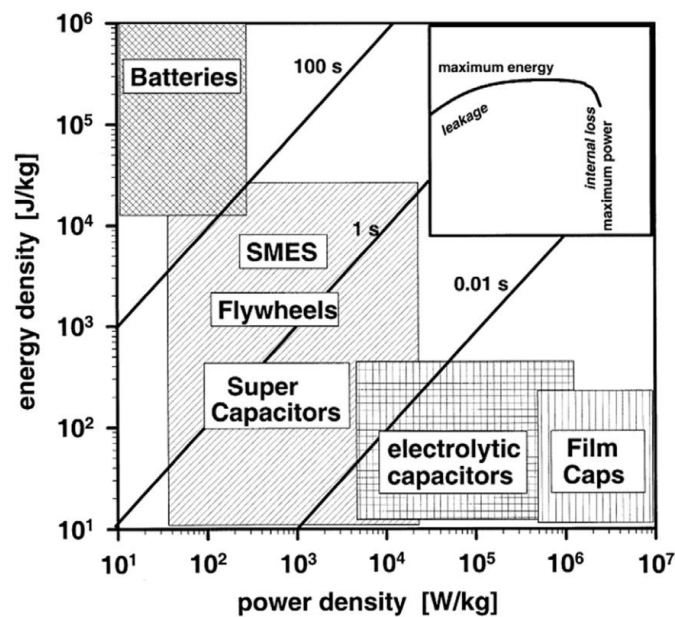


Fig. 1-5 Ragone plot. Detail window shows energy drop due to internal dissipation and leakage losses for sufficiently high and low power [63]

1.2.1 Electrode materials of capacitors

The most important electrode materials are gathered here, giving a brief explanation of their characteristics. This section is divided in three subsections comprising carbon based materials, metal oxides, and conducting polymers.

1.2.1.1 Carbon based materials

Carbon based materials are widely used in many applications. As they feature relatively low cost and an established industrial production processes, their

availability is quite high. This section details carbons for supercapacitors, from the most widespread types to the newest developments. These materials show a nearly rectangular shape cyclic voltammogram. Activated carbon is the most widely used active material for supercapacitor electrodes due to its high surface area and relatively low cost [64-66]. These are obtained from carbon-rich organic precursors through a heat treatment under inert atmosphere (carbonization) and activation resulting in porosity formation. These precursors can be obtained from natural renewable resources such as coconut shells wood, fossil fuels and their derivatives such as pitch, coal or coke, or from synthetic precursors such as polymers [64,65]. Most of the commercially available devices are constructed with activated carbon electrodes and organic electrolytes. These devices reach operating cell voltages of 2.7 V with a specific capacitance of 100–120 F g⁻¹ [67] and up to 60 F cm⁻³ [64]. This can be illustrated by a few examples. As a promising material for mass production, low-cost carbon-rich biochar (red cedar) material was reported to achieve a gravimetric capacitance of 115 F g⁻¹ in aqueous electrolyte [68]. In [69] carbon hollow fibers were reported to achieve 287 F g⁻¹ at 50 mA g⁻¹ with a capacitance retention of 86.4% at 1 A g⁻¹. In [70] a specific capacitance of 340 F g⁻¹ was reported for carbon prepared by phosphoric acid activation from a sugarcane bagasse precursor. In aqueous electrolytes the operating cell voltage is limited to 0.9 V [64] and the specific capacitance reaches 300 F g⁻¹ [65].

Carbon nanotubes (CNTs) and carbon nanofibers, are produced by the catalytic decomposition of certain hydrocarbons [61,64]. It is possible to obtain different nano structured formations controlling their crystalline order by manipulating different parameters [61]. Depending on the synthesis parameters, single walled carbon nanotubes (SWCNTs) and multi-walled carbon nanotubes (MWCNTs) can be prepared. These, have a fully accessible external surface area and high electric conductivity [61,64]. The specific capacitance of CNTs is greatly influenced by the purity and the morphology of the material [61]. The surface of CNT electrodes is mainly mesoporous, associated to the external face of the tubes. Many research efforts are focused on the development of a dense and aligned, perpendicular to the current collector, CNT forest, which could increase the capacitance retention at high current

by tuning the distance between tubes. This material seems to be promising for microelectronics applications [71,72]. As CNTs have limited SSA, leading to moderate capacitance, there is some interest in creating composites combining both CNTs and conducting polymers. These composites take advantage of the double layer capacitance of the CNTs and the pseudocapacitance of the conducting polymers, achieving higher capacitance than achievable with any of these materials alone. A graphical example in Fig. 8 illustrates a conformal deposit of pseudocapacitive material in CNTs. The composites are typically prepared by an in situ chemical polymerization of a suitable monomer, which usually forms a uniform coating on the CNT surface [61]. MWCNTs electrodeposited with polypyrrole (PPy) have achieved a specific capacitance of about 170 F g^{-1} [73,74], but due to the degradation of the polymer a cycle life greater than 100,000 cycles may not be achievable [75,76]. Similar composites using SWCNTs instead of MWCNTs have achieved specific capacitances up to 265 F g^{-1} .

Graphene is a one-atom thick sheet made of sp^2 bonded carbon atoms in a polyaromatic honeycomb crystal lattice [77-81]. This material is suitable for high performance energy storage systems due to their rate and cycle capability and improved capacity and excellent physiochemical properties [82]. Among the advantages of this material its large surface area, good flexibility, good electrical conductivity, good chemical and thermal stability, wide potential window and abundant surface functional groups can be highlighted [83]. Graphene based supercapacitors were reported with specific capacitance of 75 F g^{-1} and energy density of 31.9 W h kg^{-1} with ionic liquid electrolytes [84], and specific capacitances of 135 F g^{-1} in aqueous electrolyte and 99 F g^{-1} in organic electrolytes [85]. Reduced graphene with low agglomeration reached a maximum specific capacitance of 205 F g^{-1} in aqueous electrolyte exhibiting an energy density of 28.5 W h kg^{-1} [86].

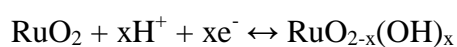
Mesoporous carbons can be prepared following different methods. Particularly, a high surface ordered meso-structures are interesting as they are capable of dealing with high power ratings without a significant capacity fading. Usually microporosity contains bottlenecks that can decrease ion mobility drastically, thus reducing the power capability of the electrode. Mesopores are not narrow paths slowing down the

ion transport, so these can maintain capacitance even at high current densities. In [87] a mesoporous carbon obtained from lignin using Pluronic F127 surfactant is reported to achieve a SSA of $624 \text{ m}^2 \text{ g}^{-1}$ after CO_2 activation and a gravimetric specific capacitance up to 102 F g^{-1} . In [88] a mesoporous carbon using rice husk precursor is reported. This reaches a BET surface area of $1357 \text{ m}^2 \text{ g}^{-1}$ with a total pore volume of $0.99 \text{ cm}^3 \text{ g}^{-1}$ and a 44.4% of mesoporosity. This carbon has a specific capacitance of 114 F g^{-1} in organic electrolyte at 5 mV s^{-1} scan rate.

1.2.1.2 Metal oxide

Metal oxides have high specific capacitance and conductivity, making them suitable for electrode fabrication focused on high energy and high power supercapacitors. There are several different metal oxide materials used for electrode fabrication such as RuO_2 [89,90], IrO_2 [91], MnO_2 [92,93], NiO [94,95], Co_2O_3 [96], SnO_2 [97], V_2O_5 [98-100] or MoO_x [101,102]. The most studied ones are ruthenium and manganese oxides [103].

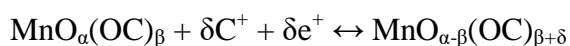
Ruthenium oxide (RuO_2) is one of the most explored electrode materials due to its advantages vis-a-vis other materials. This material has the highest specific capacitance among pseudocapacitive materials, about 1000 F g^{-1} [60]. Besides, it has a wide potential window, highly reversible redox reactions, high proton conductivity, good thermal stability, long cycle life, metallic-type conductivity, and high rate capability [104-106]. It also has three oxidation states accessible within 1.2 V [103,65]. But it has a very high cost, which reduces its applications to aerospace and military. The double layer capacitance only contributes to about 10% of the stored charge in RuO_2 electrodes, working in parallel with pseudocapacitance [103]. The pseudocapacitive behavior of ruthenium oxide involves different reactions in acidic and alkaline solutions [107,108]. In acidic electrolyte solutions, a fast reversible electron transfer and an electro-adsorption of protons onto the surface occurs where ruthenium oxidation states change from (II) to (IV) [109]:



where $x \in [0..2]$. The change of x during proton insertion/deinsertion occurs over 1.2 voltage window and leads to capacitive behavior due to ion adsorption following a

Frumkin-type isotherm [110]. Specific capacitances above 600 F g^{-1} have been achieved, but ruthenium-based aqueous systems are expensive, and their 1 V working voltage window limits their applications to small electronic devices [65].

Manganese oxides appear to be an alternative to RuO_2 thanks to their relatively low cost, low toxicity and environmental safety, and theoretical high capacitances going up to $1100\text{--}1300 \text{ F g}^{-1}$ [111-114]. The main pseudocapacitive energy storage mechanism in this material is attributed to a reversible redox transitions involving the exchange of protons and/or cations with the electrolyte and transitions between different oxidation states, Mn(III)/Mn(II), Mn(IV)/Mn(III), and Mn(VI)/Mn(IV) [115,116]. This can be expressed using the following equation:



where C^+ represents the protons and alkali metal cations (Li^+ , Na^+ , K^+) in the electrolyte, and $\text{MnO}_\alpha(\text{OC})_\beta$ and $\text{MnO}_{\alpha-\beta}(\text{OC})_{\beta+\delta}$ are $\text{MnO}_2\text{nH}_2\text{O}$ in high and low oxidation states, respectively. The morphology, composition and structures of MnO_x depend on the preparation conditions, affecting pseudocapacitive response in the material. The morphology of MnO_x is usually controllable by the preparation process or the reaction conditions [117]. For $\alpha\text{-MnO}_2$ specific capacitances of $265\text{--}320 \text{ F g}^{-1}$ were reported for the 0–1 V voltage window in a 0.1 M Na_2SO_4 aqueous electrolyte solution [115]. Specific capacitances of $195\text{--}275 \text{ F g}^{-1}$ were achieved in 2 M KCl solution, and 310 F g^{-1} in 2M $(\text{NH}_4)_2\text{SO}_4$ [115]. For $\gamma\text{-MnO}_2$ a specific capacitance of 240 F g^{-1} was achieved at 1 mA cm^{-2} [118], but usually the specific capacitances are in the range $20\text{--}30 \text{ F g}^{-1}$ [119]. $\delta\text{-MnO}_2$ synthesized in different ways exhibits specific capacitances of 236 F g^{-1} at 0.5 mA cm^{-2} in 0.1 M Na_2SO_4 electrolyte, but also specific capacitances exceeding 350 F g^{-1} [120,121] are reported.

1.2.1.3 Polymers

Polymers electrodes have high electric conductivity, up to 10^4 S cm^{-1} for doped polyacetylene, the high electroactivity, which is the ability of an electrode coated with a polymer film to reversibly change its oxidation-reduction state in a solution under the application of an external electric field, the ability to form passive layers on metal surfaces, and the semiconductor band structure [122].

Swelling and shrinking of polymers upon cycling can cause long term degradations [123,124]. Aromatic polyimides (PIs) are interesting as matrix for conducting composites because of their thermal stability, good mechanical properties and environmental stability. Composites made of intrinsically conducting polymers (ICPs) and PI matrix have improved mechanical properties, chemical stability and electrical properties under varying temperatures. For example, polypyrrole/polyimides (PPy/PI) composites show enhanced temperature and environmental stability [122]. The excellent miscibility between PPy carbonyls and PI's NH is caused by hydrogen bonding. This composite has also an excellent electroactivity [125]. A thin (less than 100 μm) high surface area conducting polymer can be grown on a current collector in order to make an electrode. During this electrochemical formation process the electrode can be p-doped or n-doped. On charging or discharging the electrode the dopant ions move in or out of the polymer electrode forming an electric double layer. These materials' charging mechanism is claimed to be pseudocapacitive rather than double layer charging, reaching very high capacitances (400–500 F g^{-1} of active material if the surface area is large enough) [122]. PPy is electroactive at positive electrode potentials. PIs are electroactive at negative potentials, and under certain conditions also at positive potentials [125]. This makes it possible to use PPy/PI composites for supercapacitors.

1.3 Research objectives

The target of this thesis is to study the carbon-based nanomaterials and composites for energy storage applications, the applications of energy storage are mainly divided into two parts: anode materials for Li-ion materials and electrode materials for supercapacitors.

For anode materials of Li-ion battery, the hollow structure MnO_2 /carbon nanofiber composites exhibit excellent electrochemical performance, because the hierarchical urchin-like structures and the superior electrical conductivity of the nanocomposites can facilitate fast electron and ion transport and accommodate a large volume change during charge/discharge process.

As electrode materials for supercapacitors, the obtained q-MC//CC (g-C₃N₄ quantum dots-MnCO₃//Carbon cloth) delivers a high specific capacity and a good cycling performance, due to the addition of g-C₃N₄ quantum dots on MnCO₃. The g-C₃N₄ quantum dots could effectively improve the interface electrical conductivity and ion transportation of the MnCO₃ electrode, which results in superior electrochemical performance.

Also, as electrode materials of supercapacitors, GH-CN (graphene hydrogel-g-C₃N₄ quantum dots) composites were prepared by hydrothermal method. The g-C₃N₄ quantum dots play an very important role in enhancing the pseudocapacitive activity, conductivity and promoting ion diffusion/transport capability. And the high nitrogen content in g-C₃N₄ can provide active sites for faradic reactions, which could increase the surface polarity, improve the wettability of electrode, enhance the mass transfer efficiency. The graphene hydrogel has a large surface area, and it can be good support for distribution of g-C₃N₄ quantum dots.

A hierarchical structure like N-GQDs/MnCO₃/ZnMn₂O₄ composite electrode was designed and synthesized using simple, low-cost, and effective hydrothermal approach for supercapacitor applications. The resulting composite had a hierarchical structure formed with nanosheets, particles and quantum dots which provided a abundant pores for rapid electrons and ions transportation. Moreover, the dispersion of MnCO₃ particles on ZnMn₂O₄ nanosheets was more favorable to the synergistic effects, and the addition of N-GQDs enhanced higher conductivity.

These objectives can open more research approaches on energy storage devices by other future studies.

1.4 References

- [1] T. Christen, M.W. Carlen, *J. Power Sources* 91 (2) (2000) 210–216.
- [2] P.J. Hall, E.J. Bain, *Energy Policy* 36 (2008) 4352–4355.
- [3] J.M. Tarascon, M. Armand, *Nature* 414 (6861) (2001) 359.
- [4] S. Pacala, R. Socolow, *Science* 305 (5686) (2004) 968.
- [5] N. Nitta, F. Wu, J.T. Lee, G. Yushin, *Mater. Today* 18 (5) (2015) 252–264.

- [6] G. Girishkumar, B. McCloskey, A.C. Luntz, S. Swanson, W. Wilcke, *J. Phys. Chem. Lett* 1 (14) (2010) 2193–2203.
- [7] L. Zhang, Z. Wang, D. Xu, X. Zhang, L. Wang, *Int. J. Smart Nano Mater.* 4 (1) (2013) 27–46.
- [8] P.G. Bruce, S.A. Freunberger, L.J. Hardwick, J. Tarascon, *Nat. Mater.* 11 (1) (2012) 19–29.
- [9] M.M. Thackeray, C. Wolverton, E.D. Isaacs, *Energy Environ. Sci.* 5 (2012) 7854–7863.
- [10] P. Verma, P. Maire, P. Novák, *Electrochim. Acta* 55 (2010) 6332–6341.
- [11] J. Janek, W.G. Zeier, *Energy* 500 (400) (2016) 300.
- [12] Armstrong, A.R., Bruce, P.G. *Nature* 381, 499–500 (1996).
- [13] Kang, K.S., Meng, Y.S., Breger, J., et al. *Science* 311, 977–980 (2006)
- [14] Yabuuchi, N., Ohzuku, T. *J. Power Sources* 119, 171–174 (2003).
- [15] Okubo, M., Hosono, E., Kim, J., et al. *J. Am. Chem. Soc.* 129, 7444–7452 (2007).
- [16] Guerard, D., Herold, A. *Carbon* 13, 337–345 (1975).
- [17] Scrosati, B., Garche, J. *J. Power Sources* 195, 2419–2430 (2010).
- [18] Cho, J., Kim, Y.J., Park, B. *Chem. Mater.* 12, 3788–3791 (2000).
- [19] Song, S.W., Zhuang, G.V., Ross, P.N. *J. Electrochem. Soc.* 151, A1162–A1167 (2004)
- [20] Tran, H.Y., Greco, G., Täubert, C., et al. *J. Power Sources* 210, 276–285 (2012).
- [21] Wang, Z.X., Sun, Y.C., Chen, L.Q., et al. *J. Electrochem. Soc.* 151, A914–A921 (2004)
- [22] Rao, C.V., Reddy, A.L.M., Ishikawa, Y., et al. *ACS Appl. Mater. Interfaces* 3, 2966–2972 (2011).
- [23] Tarascon, J.M., McKinnon, W.R., Coowar, F., et al. *J. Electrochem. Soc.* 141, 1421–1431 (1994).
- [24] Chung, S.Y., Bloking, J.T., Chiang, Y.M. *Nat. Mater.* 1, 123–128 (2002).
- [25] Thackeray, M.M., Kang, S.H., Johnson, C., et al. *J. Mater. Chem.* 17, 3112–3125 (2007).
- [26] Yabuuchi, N., Yoshii, K., Myung, S.T., et al. *J. Am. Chem. Soc.* 133, 4404–4419

- (2011).
- [27] Zheng, J.M., Gu, M., Xiao, J., et al. *Nano Lett.* **13**, 3824–3830 (2013).
- [28] Zheng, J.M., Gu, M., Genc, A., et al. *Nano Lett.* **14**, 2628–2635 (2014).
- [29] Zhu, Z., Kushima, A., Yin, Z., et al. *Nat. Energy* **1**, 16111 (2016).
- [30] Lu, J., Lee, Y. J., Luo, X., et al. *Nature* **529**, 377–382 (2016).
- [31] Tan, G., Xu, R., Xing, Z., et al. *Nat. Energy* **2**, 17090 (2017).
- [32] Whittingham, M.S. *Chem. Rev.* **104**, 4271–4301 (2004).
- [33] Grey, C.P., Dupre, N. *Chem. Rev.* **104**, 4493–4512 (2004).
- [34] Ellis, B.L., Lee, K.T., Nazar, L.F. *Chem. Mater.* **22**, 691–714 (2010).
- [35] Luntz, A.C., McCloskey, B.D. **114**, 11721–11750 (2014).
- [36] Bruce, P.G., Freunberger, S.A., Hardwick, L.J., et al. *Nat. Mater.* **11**, 19–29 (2012).
- [37] Chen, J., Cheng, F.Y. *Acc. Chem. Res.* **42**, 713–723 (2009).
- [38] Yang, Y., Zheng, G., Cui, Y. *Chem. Soc. Rev.* **42**, 3018–3032 (2013).
- [39] Long, J.W., Dunn, B., Rolison, D.R., et al. *Chem. Rev.* **104**, 4463–4492 (2004).
- [40] Goriparti, S., Miele, E., Angelis, F.D., et al. *J. Power Sources* **257**, 421–443 (2014).
- [41] Hassoun, J., Scrosati, B. *J. Electrochem. Soc.* **162**, A2582–A2588 (2015).
- [42] Landi, B.J., Ganter, M.J., Cress, C.D., et al. *Energy Environ. Sci.* **2**, 638–654 (2009).
- [43] Lee, S.W., Yabuuchi, N., Gallant, B.M., et al. *Nat. Nanotechnol.* **5**, 531–537 (2010).
- [44] Qie, L., Chen, W.M., Wang, Z.H., et al. *Adv. Mater.* **24**, 2047–2050 (2012).
- [45] Su, F.Y., He, Y.B., Li, B.H., et al. *Nano Energy* **1**, 429–439 (2012).
- [46] Ambrosi, A., Chua, C.K., Bonanni, A., et al. *Chem. Rev.* **114**, 7150–7188 (2014).
- [47] Fang, Y., Lv, Y.Y., Che, R.C., et al. *J. Am. Chem. Soc.* **135**, 1524–1530 (2013).
- [48] Stein, A., Wang, Z.Y., Fierke, M.A. *Adv. Mater.* **21**, 265–293 (2009).
- [49] Wu, H., Chan, G., Choi, J.W., et al. *Nat. Nanotechnol.* **7**, 310–315 (2012).
- [50] Park, C.M., Kim, J.H., Kim, H., et al. *Chem. Soc. Rev.* **39**, 3115–3141 (2010).
- [51] Miyachi, M., Yamamoto, H., Kawai, H., et al. *J. Electrochem. Soc.* **152**, A2089–A2091 (2005).

- [52] Xue, D.J., Xin, S., Yan, Y., et al. *J. Am. Chem. Soc.* **134**, 2512–2515 (2012).
- [53] Seo, M.H., Park, M., Lee, K.T., et al. *Energy Environ. Sci.* **4**, 425–428 (2011).
- [54] Idota, Y., Kubota, T., Matsufuji, A., et al. *Science* **276**, 1395–1397 (1997).
- [55] Lee, K.T., Jung, Y.S., Oh, S.M. *J. Am. Chem. Soc.* **125**, 5652–5653 (2003).
- [56] Lee, K., Mazare, A., Schmuki, P. *Chem. Rev.* **114**, 9385–9454 (2014).
- [57] Poizot, P., Laruelle, S., Grugeon, S., et al. *Nature* **407**, 496–499 (2000).
- [58] Ji, L.W., Lin, Z., Alcoutlabi, M., et al. *Energy Environ. Sci.* **4**, 2682–2699 (2011).
- [59] Rowsell, J.L.C., Pralong, V., Nazar, L.F. *J. Am. Chem. Soc.* **123**, 8598–8599 (2001).
- [60] Miller JR, Simon P. *Science* 2008;321(5889):651–2.
- [61] Pandolfo A, Hollenkamp A. *J Power Sources* 2006;157(1):11–27.
- [62] Kötz R, Carlen M. *Electrochim Acta* 2000;45:2483–98.
- [63] Christen T, Carlen MW. *J Power Sources* 2000;91 (2):210–6.
- [64] Simon P, Burke A. *Soc. Interface* 2008;17(1):38–44.
- [65] Simon P, Gogotsi Y. *Nat Mater* 2008;7(11):845–54.
- [66] Zhang LL, Zhao XS. *Chem Soc Rev* 2009;38(9):2520–31.
- [67] Fernández J, Morishita T, Toyoda M. *J Power Sources* 2008;175(2008):675–9.
- [68] Jiang J, Zhang L, Wang X, Holm N, Rajagopalan K, Chen F, et al. *Electrochim Acta* 2013;113:481–9.
- [69] Du X, Zhao W, Wang Y, Wang C, Chen M, Qi T, et al. *Bioresour Technol* 2013;149:31–7.
- [70] Thambidurai A, Lourdasamy JK, John JV, Ganesan S. *Kor J Chem Eng* 2014;31 (2):268–75.
- [71] Talapatra S, Kar S, Pal SK, Vajtai R, Ci L, Victor P, et al. *Nat Nanotechnol* 2006;1(2):112–6.
- [72] Pushparaj VL, Shaijumon MM, Kumar A, Murugesan S, Ci L, Vajtai R, et al. *Proc Natl Acad Sci* 2007;104(34):13574–7.
- [73] Hughes M, Shaffer MSP, Renouf AC, Singh C, Chen GZ, Fray DJ, et al. *Adv Mater* 2002;14(5):382–5.
- [74] Frackowiak E, Jurewicz K, Szostak K, Delpeux S, Béguin F. *Fuel Process Technol* 2002;77–78:213–9.

- [75] Hughes M, Shaffer M, Renouf A, Singh C, Chen G, Fray D, et al. *Adv Mater* 2002;14(5):382.
- [76] Hughes M, Chen GZ, Shaffer MSP, Fray DJ, Windle AH. *Chem Mater* 2002;14(4):1610–3.
- [77] Wu Z-S, Zhou G, Yin L-C, Ren W, Li F, Cheng H-M. *Nano Energy* 2012;1(1):107–31.
- [78] Novoselov KS, Geim AK, Morozov SV, Jiang D, Zhang Y, Dubonos SV, et al. *Science (New York, N.Y.)* 2004;306(5696):666–9.
- [79] Novoselov KS, Geim AK, Morozov SV, Jiang D, Katsnelson MI, Grigorieva IV, et al. *Nature* 2005;438(7065):197–200.
- [80] Geim A, Novoselov K. *Nat Mater* 2007:183–91.
- [81] Geim A. *Science (New York, N.Y.)* 2009;324 (5934):1530–4.
- [82] Chen H, Müller MB, Gilmore KJ, Wallace GG, Li D. *Adv Mater* 2008;20(18):3557–61.
- [83] Pumera M. *Chem Soc Rev* 2010;39(11):4146–57.
- [84] Vivekchand SRC, Rout CS, Subrahmanyam KS, Govindaraj A, Rao CNR. *J Chem Sci* 2008;120 (1):9–13.
- [85] Stoller M, Park S, Zhu Y, An J, Ruoff R. *Nano Lett* 2008:6–10.
- [86] Wang Y, Shi Z, Huang Y, Ma Y. *J Phys Chem C* 2009;113(30):13103–7.
- [87] Saha D, Li Y, Bi Z, Chen J, Keum JK, Hensley DK, et al. *Langmuir : ACS J Surf Colloids* 2014;30(3):900–10.
- [88] Kumagai S, Sato M, Tashima D. *Electrochim Acta* 2013;114:617–26.
- [89] Ahn YR, Song MY, Jo SM, Park CR, Kim DY. *Nanotechnology* 2006;17(12):2865.
- [90] Patake VD, Lokhande CD, Joo OS. *Appl Surf Sci* 2009;255 (7):4192–6.
- [91] Hu CC, Huang YH, Chang KH. *J Power Sources* 2002;108(1–2):117–27.
- [92] Yan J, Wei T, Cheng J, Fan Z, Zhang M. *Mater Res Bull* 2010;45 (2):210–5.
- [93] Jiang J, Kucernak A. *Electrochim Acta* 2002;47(15):2381–6.
- [94] Patil UM, Salunkhe RR, Gurav KV, Lokhande CD. *Appl Surf Sci* 2008;255(5 (Part 2)):2603–7.
- [95] Nelson PA, Owen JR. *J Electrochem Soc* 2003;150(10):A1313.

- [96] Kandalkar SG, Gunjekar JL, Lokhande CD. *Appl Surf Sci* 2008;254 (17):5540–4.
- [97] Miura N, Oonishi S, RajendraPrasad K. *Electrochem SolidState Lett* 2004;7(8):A247.
- [98] Hu CC, Huang CM, Chang KH. *J Power Sources* 2008;185(2):1594–7.
- [99] da Silva DL, Delatorre RG, Pattanaik G, Zangari G, Figueiredo W, Blum R-P, et al. *J Electrochem Soc* 2008;155(1):E14.
- [100] Zhou X, Chen H, Shu D, He C, Nan J. *J Phys Chem Solids* 2009;70(2):495–500.
- [101] Nakayama M, Tanaka A, Sato Y, Tonosaki T, Ogura K. *Langmuir* 2005;21(13):5907–13.
- [102] Babakhani B, Ivey DG. *J Power Sources* 2010;195(7):2110–7.
- [103] Wang G, Zhang L, Zhang J. *Chem Soc Rev* 2012;41(2):797–828.
- [104] Kim I-H, Kim K-B. *J Electrochem Soc* 2006;153(2):A383.
- [105] Jia QX, Song SG, Wu XD, Cho JH, Foltyn SR, Findikoglu AT, et al. *Appl Phys Lett* 1996;68(8):1069.
- [106] Sakiyama K, Onishi S, Ishihara K. *J Electrochem Soc* 1993;140(3):834–9.
- [107] Zheng J, Cygan P, Jow T. *J Electrochem Soc* 1995;142(8):9–13.
- [108] Wu N-L, Kuo S-L, Lee M-H. *J Power Sources* 2002;104:62–5.
- [109] Hu CC, Lee CH, Wen TC. *J Appl Electrochem* 1996;26(1):72–82.
- [110] Conway B. New York: Kluwer Academic; 1999.
- [111] Pang S-C, Anderson Ma, Chapman TW. *J Electrochem Soc* 2000;147(2):444.
- [112] Toupin M, Brousse T, Belanger D. *Chem Mater* 2002;14(9):3946–52.
- [113] Toupin M, Brousse T, Belanger D. *Chem Mater* 2004;16 (16):3184–90.
- [114] Chang J-K, Lee M-T, Tsai W-T. *J Power Sources* 2007;166(2):590–4.
- [115] Hu C-C, Tsou T-W. *Electrochem Commun* 2002;4:105–9.
- [116] Messaoudi B, Joiret S, Keddou M, Takenouti H. *Electrochim Acta* 2001;46(16):2487–98.
- [117] Donne S, Hollenkamp AF, Jones B. *J Power Sources* 2010;195(1):367–73.
- [118] Chou S, Cheng F, Chen J. *J Power Sources* 2006;162(1):727–34.
- [119] Brousse T, Toupin M, Dugas R, Athouel L, Crosnier O, Belanger D. *J Electrochem Soc* 2006;153 (12):A2171.

- [120] Zolfaghari A, Ataherian F, Ghaemi M, Gholami A. *Electrochim Acta* 2007;52(8):2806–14.
- [121] Ghaemi M, Ataherian F, Zolfaghari A, Jafari S. *Electrochim Acta* 2008;53(14):4607–14.
- [122] Levine K. *Synthesis*, University of Cincinnati; 2002.
- [123] Arbizzani C, Mastragostino M, Soavi F. *J Power Sources* 2001;100:164–70.
- [124] Frackowiak E, Khomenko V, Jurewicz K, Lota K, Béguin F. *J Power Sources* 2006;153(2):413–8.
- [125] Haushalter RC, Krause LJ. *Thin Solid Films* 1983;102:161–71.

CHAPTER 2. Hierarchical hollow urchin-like structured MnO₂ microsphere/carbon nanofiber composites as anode materials for Li-ion batteries

2.1 Introduction

Lithium ion batteries (LIBs) is well-developed energy storage device for various applications such as portable electronic devices, electric vehicles, and sustainable energy generation systems because of their attractive high gravimetric and volumetric energy densities compared with other energy storage techniques [1,2]. In the past, the anode in LIBs is usually composed of carbonaceous materials with long lifespan and low cost, but their low storage capacity and safety problems are the major concerns for large-scale energy storage applications [3,4]. Currently, a variety of transition metal oxides have been widely investigated as potential anode materials for LIBs [5,6]. However, the employment of metal oxides is still largely hampered by their poor long-term cycling stability and intrinsic low charge/ionic conductivity.

In this regard hierarchical hollow nanostructured materials have been explored in recent years, due to their high specific surface area and hollow structure, which facilitates fast diffusion of the electrolyte ions and fast conduction of electrons. Typically, a hierarchical hollow nanostructure can be obtained using the template-assisted method with soft or hard templates, such as polystyrene spheres, silica particles, and micelles [7–11]. However, this method required the removal of the template or sacrificial material using a harsh process with high temperatures or toxic chemical agents, often leading to structural collapse, limiting the scalable process for large scale production. Therefore, it is highly needed to develop simple and facile synthetic methods obtaining hierarchical hollow nanostructured materials for energy storage applications. Nanostructured manganese dioxides (MnO₂) have attracted considerable attention as promising electrode materials for energy storage applications, such as supercapacitors and Li-ion batteries owing to their high theoretical capacity (1232 mAh g⁻¹), low cost, environmental friendliness, and

abundant amount in nature [12–14]. However, the intrinsically poor electrical conductivity and low structural stability of MnO_2 limit their practical applications. Specifically, MnO_2 as an electrode of lithium ion batteries suffers fast capacity fading and poor cycling performance, which is attributed to their low electrical conductivity and large volume change with severe aggregation during charge/discharge cycling [14,15]. In order to overcome these limitations, extensive research has focused on the development of nanostructured MnO_2 with large specific surface areas and the preparation of its composite with conductive additives [16–20]. However, it has been still challenging to synthesis the nanostructured MnO_2 with a high surface area, for example, 1D nanowires/nanorods [21,22], 2D nanosheets [23,24] and 3D nanoflowers [18–20]. Among these MnO_2 nanostructures, while various studies have reported synthesis and properties of hierarchical urchin-like MnO_2 [25–27], few reports have been reported on the synthesis of hierarchical hollow urchin-like MnO_2 [28,29] consisting of a hollow microsphere with 1D nanorods or nanotubes. To enhance the electrical conductivity, the preparation of MnO_2 nanocomposites has been extensively studied using conductive carbon-based additives, such as graphene [27,30], carbon nanotubes (CNTs) [31], and carbon nanofibers (CNFs) [32]. Specifically, the utilization of CNTs and CNFs with the hierarchical nanostructured MnO_2 could be an effective way to accommodate large volume change and improve the electrical conductivity of the MnO_2 .

Herein, we demonstrated a simple and facile hydrothermal synthesis of hierarchical hollow urchin-like MnO_2 microspheres (u- MnO_2), consisting of a hollow inner sphere with nanotubes on the outer surface. The structure and morphology of the MnO_2 particles were controlled by hydrothermal reaction time and finally evolved into the u- MnO_2 . In addition, the u- MnO_2 /CNFs composites were prepared and investigated for an anode electrode of Li-ion batteries. Our work showed that the u- MnO_2 /CNFs nanocomposites have enhanced electrochemical performance of high capacity, good cycling stability and rate capability, which is associated with the hierarchical nanostructures as well as the synergetic effect of u- MnO_2 /CNFs nanocomposites.

2.2 Experimental

Preparation of u-MnO₂ and u-MnO₂/CNFs nanocomposites

In one-pot hydrothermal synthesis procedure, 8 mmol KMnO₄ was dissolved completely in 120 mL deionized (DI) water, and the 12 M HCl aqueous solution was then slowly dropped into the solution under magnetic stirring (the molar ration of KMnO₄ to HCl is 1:10). After stirring for 20 min, the obtained mixture solution was transferred to a 200 mL Teflon-lined stainless steel autoclave, which was heated to 120°C and maintained for 4 h. After the autoclave was then cooled down to room temperature, the precipitates were collected by centrifugation at 5000 rpm for 15 min. The obtained products were washed with ethanol and DI water several times, and then dried in an oven at 60 °C overnight. For the preparation of the u-MnO₂/CNFs nanocomposites, commercial CNFs (*ca.*100 nm in diameter, Sigma-Aldrich) were first oxidized in a concentrated nitric acid with mechanical stirring for 6 h. The oxidized CNFs were then collected by filtration and dried in a vacuum oven at 80 °C overnight. The prepared u-MnO₂ was then added to the oxidized CNFs aqueous solution (3 mg/mL) with short sonication and stirring for 12 h (the weight ratio of u-MnO₂ to CNFs is 8:1), followed by filtration and drying at 80 °C. As the control sample, the particle-shaped MnO₂ (p-MnO₂) was synthesized after 1 h of hydrothermal reaction and fabricated the p-MnO₂/CNFs nanocomposite using the same procedure above.

2.3 Characterization

X-ray diffraction (XRD) measurement was performed using a Bruker D8 Advance diffractometer with a non-monochromated Cu K α operated at 40 kV and 30 mA. The morphology of the samples was characterized using a field-emission scanning electron microscope (FE-SEM, JEOL-JSM820) and a transmission electron microscope (TEM, Hitachi, H-8100). Fourier transform infrared (FT-IR) spectra were obtained using a Nicolet IR 200 FT-IR spectrometer (Thermo Scientific). The specific surface area was measured using a surface area and porosity analyzer (Micromeritics, ASAP 2020, USA) with the calculations performed using the Brunauer-Emmett-Teller (BET) equation.

2.4 Electrochemical measurement

The electrochemical performance of the u-MnO₂/CNFs nanocomposites were investigated using the anode electrode Li-ion batteries which consisted of 90 wt% u-MnO₂/CNFs as the active material with 10 wt% carboxyl methyl cellulose (CMC) as the binder. The slurry of the anode electrode mixture was then coated using the doctor-blade technique on copper foil, dried in a convection oven at 60 °C for 30 min, and subsequently placed in a vacuum oven overnight at 70 °C. The loading density of the anode electrode was approximately 1.3 g cm⁻³. For electrochemical characterizations, CR2016 coin half-cells were assembled with the u-MnO₂/CNFs electrode and lithium foil as the working and counter electrodes, respectively. The electrolyte used in this work was 1 M LiPF₆ (Panaxetec Co., Korea) dissolved into a mixture of ethylene carbonate (EC), dimethyl carbonate (DMC), and ethylene carbonate (EMC) at volumetric ratio of 1:1:1. All cells were assembled in an argon-filled glove box. The anodic performance was characterized using a galvanostatic charge/discharge between 0.1 V and 3.0 V in an automatic battery cycler (WBCS3000 Co., Korea) with a 0.1 C rate for the first 2 cycles and a 0.5 C rate for the next 98 cycles. The rate capability of the prepared anodes was tested at various charge/discharge current rates. Electrochemical impedance spectroscopy (EIS) was performed using a using a BioLogic VSP potentiostat at a frequency range of 0.01 Hz - 100 kHz.

2.5 Results and discussion

In this work, a simple hydrothermal synthesis method was used for the hierarchical hollow urchin-like MnO₂ microsphere (u-MnO₂) without neither template nor surfactant. Briefly, a mixture solution of KMnO₄ and HCl in deionized water was heated at 120 °C in an autoclave for 4 h to synthesize the u-MnO₂. The morphology and microstructure of u-MnO₂ were characterized by field-emission scanning electron microscopy (FE-SEM) and transmission electron microscopy (TEM). Fig. 2-1a shows the as-synthesized u-MnO₂ had a typical sea urchin shape with a diameter of 3–4 μm and 1D nanotubes on the outer surface. The broken microsphere shown in Fig. 1a

indicates that the obtained u-MnO₂ had hollow urchin-like structures. In addition, TEM image in Fig. 2-1b clearly shows a hollow inner space of u-MnO₂. High magnification FE-SEM and TEM images in Fig. 2-1c and d shows that these spherical hollow urchin was composed of radially grown MnO₂ nanotubes with a diameter of about 50–100 nm. These unique hollow urchin-like nanostructures of u-MnO₂ with the numerous nanotubes can provide high surface area (Fig. 2-2) and reactive sites, which could be beneficial for facilitating electrolyte diffusion and fast electron transportation. The crystallographic structure of u-MnO₂ was examined by XRD, as shown in Fig. 2-3. All diffraction peaks of u-MnO₂ could be indexed to a tetragonal phase of α -MnO₂ (JCPDS 44-0141) with a lattice constant of $a = b = 9.783 \text{ \AA}$, $c = 2.863 \text{ \AA}$. No anomalous peaks such as the β - or γ - MnO₂ phase could be observed, indicating the obtained u-MnO₂ could show high purity of the α -MnO₂ phase.

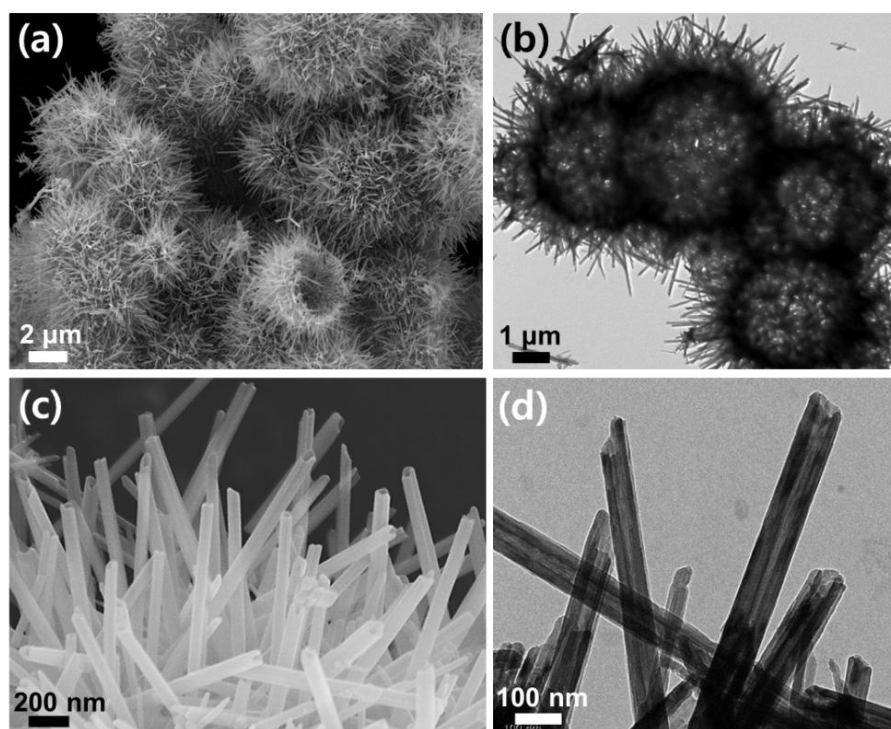


Fig. 2-1(a) FE-SEM image and (b) TEM image of u-MnO₂ microspheres. (c) FE-SEM image and (d) TEM image of nanotubes of u-MnO₂

To explore the synthesis formation of the hierarchical hollow urchin-like structure of u-MnO₂, a series of experiments with different hydrothermal times were

conducted. Fig. 2-4 shows SEM images of the obtained products at 120 °C for different hydrothermal times. As shown in Fig. 2-4a and Fig. 2-5, it is observed that the MnO₂ products obtained after 1 h are microspheres decorated with small irregular nanobumps (p-MnO₂). When the hydrothermal time was prolonged to 2 h, thin nanowalls were formed on the surface of the MnO₂ microspheres (Fig. 2-4b). For the 3 h of reaction time, it can be seen that some nanoneedles were grown between nanowalls (Fig. 2-4c). The TEM images shown in Fig. 2-6 indicate that the MnO₂ products of 1 h and 2 h reaction times have solid cores, while a semi-hollow core is found for the MnO₂ of 3 h reaction. With the reaction time reaching 4 h, Fig. 2-4d reveals that the long nanotubes were densely grown on the microsphere without nanowalls and formed hierarchical urchin-like structured MnO₂ microspheres. Also, a small number of opened u-MnO₂ particles can be observed, confirming the hollow sphere structure. After a longer hydrothermal reaction of 8 h, the hollow urchin-like structure of MnO₂ was maintained, although further broken and opened u-MnO₂ microspheres were found (Fig. 2-7).

The corresponding XRD patterns of the obtained products at different reaction time are presented in Fig. 2-8a. The XRD graphs for the products of 1, 2, and 3 h reaction time show that the diffraction peaks can be indexed to two different phases of manganese oxides, the cubic phase of Mn₂O₃ (JCPDS 65-7467, $a = b = c = 9.41 \text{ \AA}$) and the tetragonal phase of α -MnO₂, indicating the coexistence of Mn₂O₃ and α -MnO₂ phases. As the hydrothermal time increased, the Mn₂O₃ phase began to disappear, and the diffraction peaks of the α -MnO₂ phase were only detected after a reaction time of 4 h. According to the above evolution of the time-dependent morphology and crystallinity, we proposed the formation mechanism of u-MnO₂ as illustrated in Fig. 2-8b. In the initial stage, the high concentration of MnO₂ was present caused by the reaction of KMnO₄, and the MnO₂ molecules tended to aggregate to form microsphere particles with nanobumps that minimized the overall energy of the system. As the hydrothermal reaction proceeded, thin nanowalls grew on the surface of the microspheres. When KMnO₄ was consumed completely, the entire system was transferred to a thermodynamically stable environment. Then, because of the 1D growth habit of the α -MnO₂ crystal [33], MnO₂ nanoneedles began

to grow and form a hierarchical urchin-like structure, where the microsphere core served as the nucleation seed. Finally, the nanotubes grew outside by expanding the MnO_2 microspheres core, resulting in hollow microspheres with nanotubes.

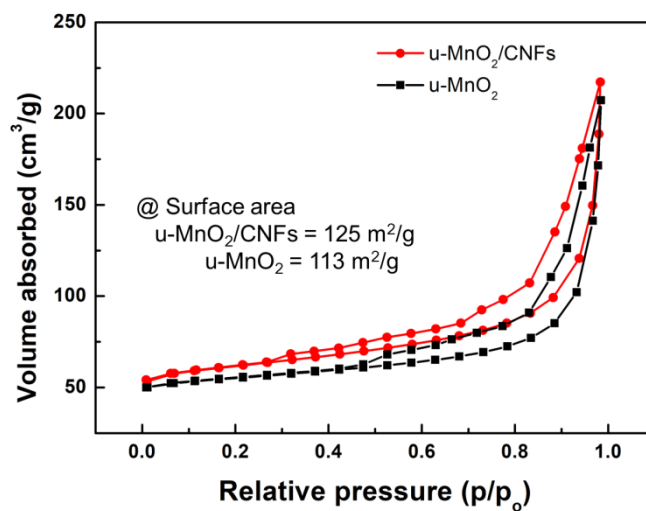


Fig. 2-2 N₂ adsorption/desorption isotherms for bare u-MnO₂ and u-MnO₂/CNFs composite.

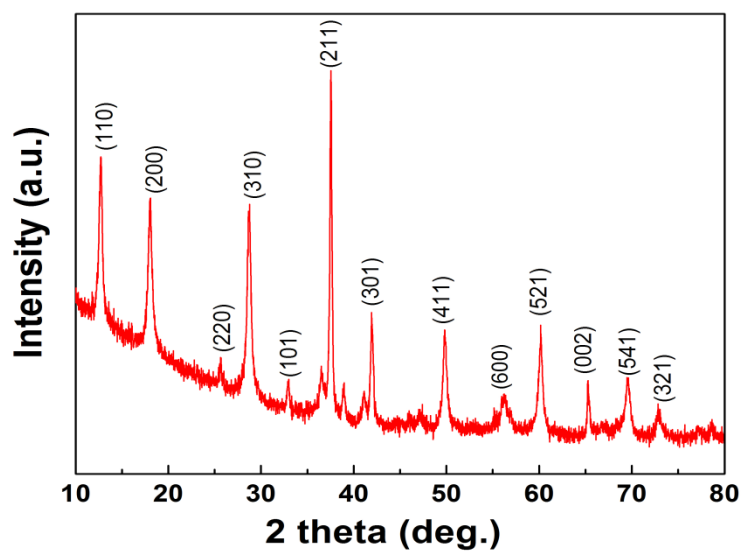


Fig. 2-3 XRD patterns of the obtained u-MnO₂

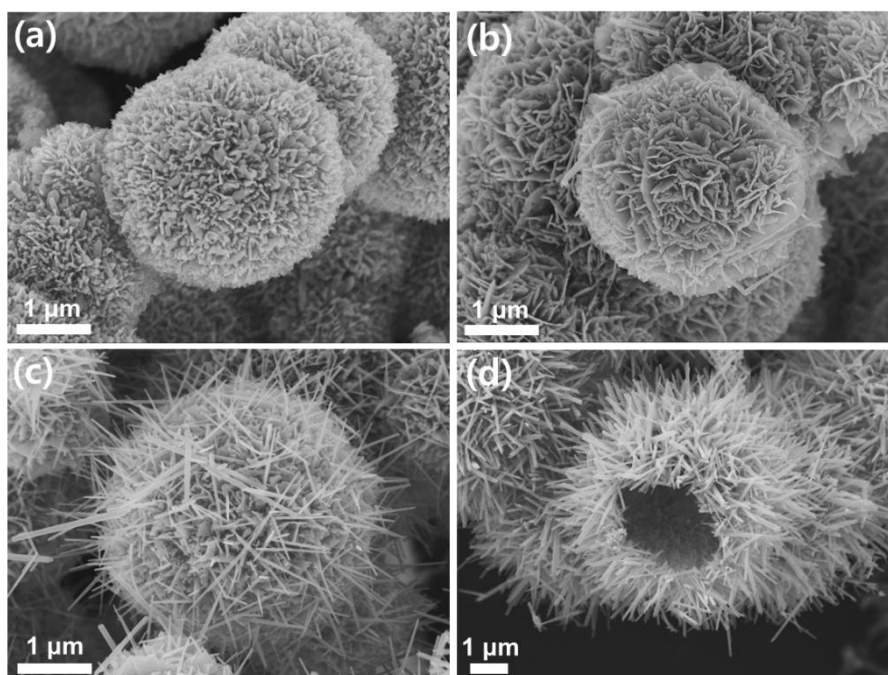


Fig. 2-4 FE-SEM image of the obtained MnO₂ products at the different hydrothermal reaction time. (a) 1 hr, (b) 2 hr, (c) 3 hr, and (d) 4 hr.

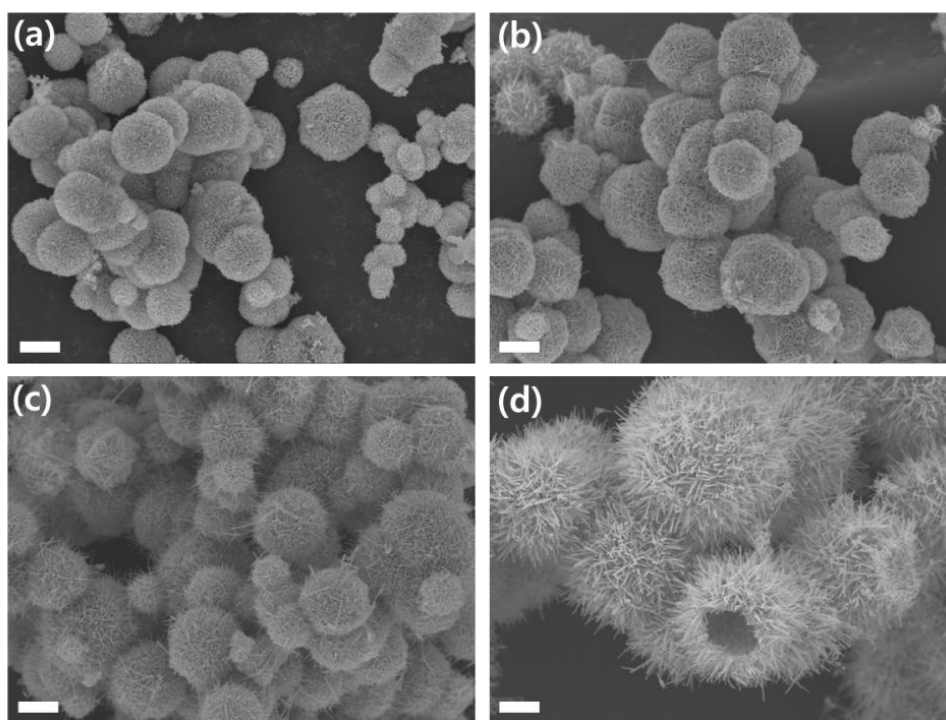


Fig. 2-5 Low magnified FE-SEM image of the obtained MnO₂ products at the different hydrothermal reaction time. (a) 1 hr, (b) 2 hr, (c) 3 hr, and (d) 4 hr. (scale bar is 1 μm)

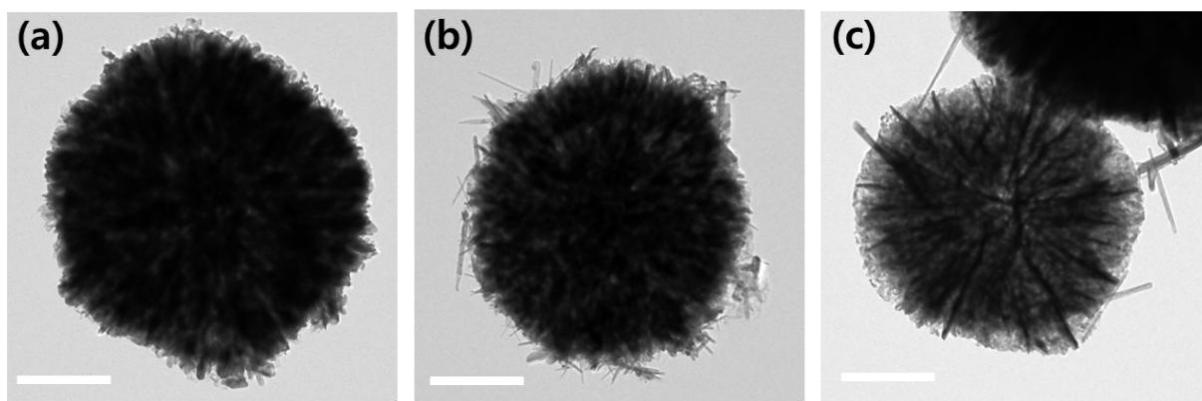


Fig. 2-6 TEM images of the obtained MnO₂ products at the different hydrothermal reaction time. (a) 1 hr, (b) 2 hr, and (c) 3 hr. (scale bar is 1 μ m)

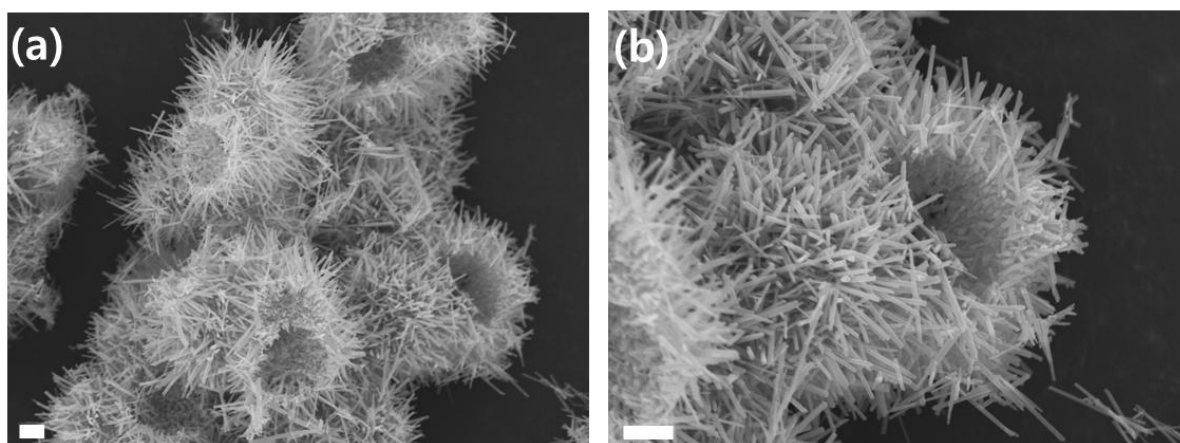


Fig. 2-7 (a) FE-SEM image of the u-MnO₂ products after 8 h of hydrothermal reaction time and (b) its high magnified image. (scale bar is 1 μ m)

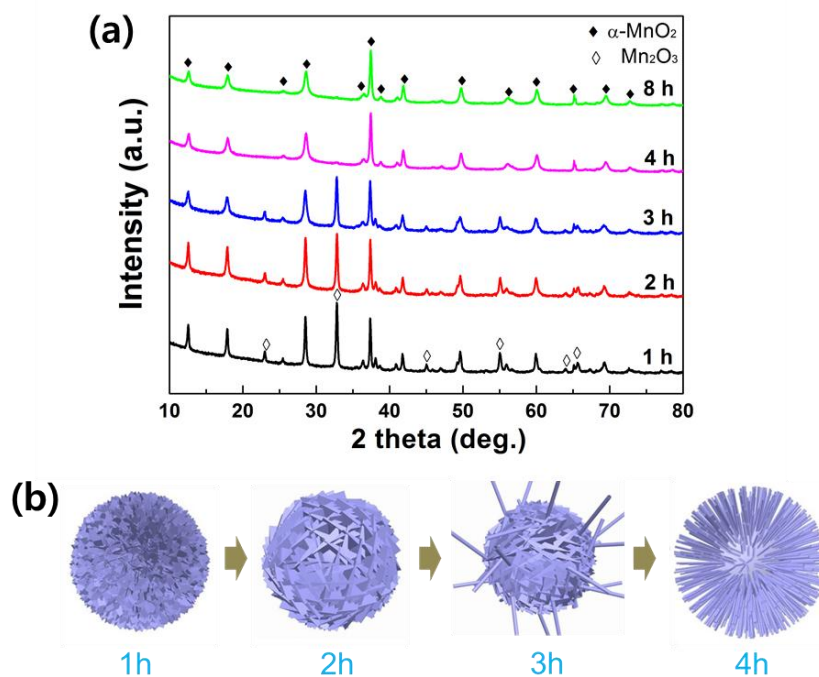


Fig. 2-8 (a) XRD patterns of the obtained MnO_2 products at the different hydrothermal reaction time. (b) Schematic illustration of the morphological evolution of α - MnO_2 microspheres.

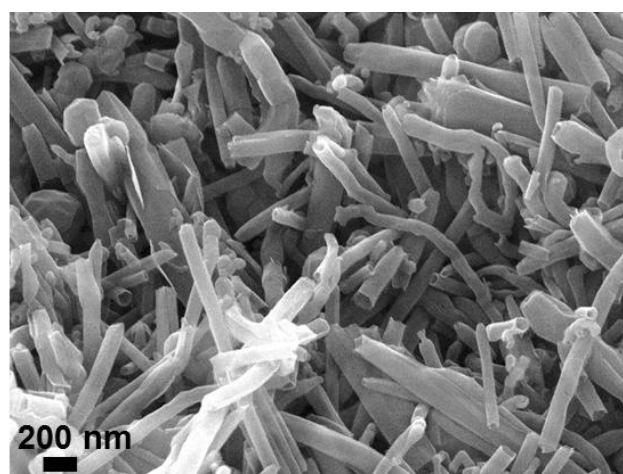


Fig. 2-9 FE-SEM image of CNFs.

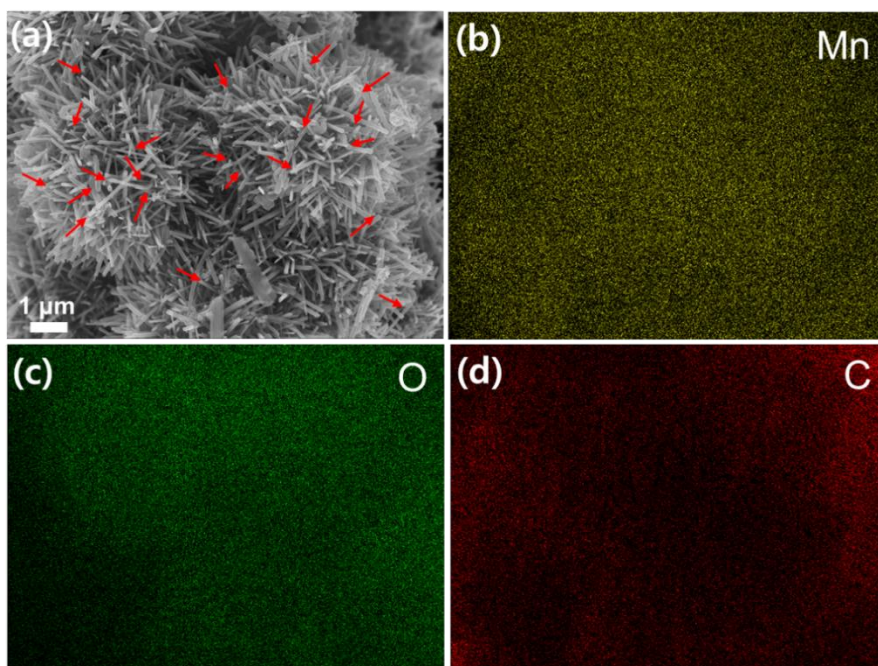


Fig. 2-10 (a) FE-SEM image of the u-MnO₂/CNFs nanocomposite, and corresponding quantitative EDS element mapping of (b) Mn, (c) O and (d) C.

For the potential application of electrode materials of energy storage, the electrical conductivity of u-MnO₂ needs to be improved. The preparation of a composite with 1D carbon nanofibers (CNFs) could be beneficial to maximize the utilization of the hierarchical structure of u-MnO₂. The incorporation of CNFs with nanotubes of u-MnO₂ may retain a large specific area of hierarchical u-MnO₂ and a fast electron and ion transport. The morphology of CNFs used in this work was characterized by FE-SEM (Fig. 2-9), and the range of diameter of the CNFs is about 100–200 nm. Fig. 2-10a shows the morphology of the obtained u-MnO₂/CNFs nanocomposite. Because of a similar morphology of CNFs with the nanotubes of u-MnO₂, the CNFs in the nanocomposite were identified by red arrows, revealing that CNFs uniformly exist between the nanotubes of u-MnO₂ and retain the hierarchical structure. A corresponding elemental mapping analysis was conducted, as depicted in Fig. 2-10b–d. The u-MnO₂/CNFs nanocomposite is mainly composed of Mn, O, and C elements, which are homogeneously distributed throughout the composite. These results were also confirmed by the XRD and FT-IR measurements, showing the successful fabrication of u-MnO₂/CNFs nanocomposite (Fig. 2-11). In addition, the CNFs content can be evaluated from the TGA measurement (Fig. 2-12), showing the

weight loss (~12.5%) around 600 °C due to the oxidation of CNFs.

The electrochemical properties of bare u-MnO₂ and u-MnO₂/CNFs nanocomposite were investigated. Fig. 2-13a and b shows the CV curves for the first four charge/discharge cycles with a scanning rate of 0.5 mV s⁻¹ between 0.01 V–3.0 V. The curves of the u-MnO₂/CNFs nanocomposite and bare u-MnO₂ exhibit similar anodic and cathodic peaks, implying similar redox reaction for both samples during the charge/discharge process. For the first cycle, the distinct cathode peak near 0.25 V corresponds to the complete reduction of Mn²⁺ to metallic Mn⁰, and the decomposition of the electrolyte, and the formation of the solid electrolyte interface (SEI) layer. In the anodic scan for the first cycle, the distinct peak near 1.3 V and the broad peak around 2.1 V were observed, which corresponds to the oxidation of Mn⁰ to Mn⁴⁺ to re-form MnO₂ and the decomposition of the polymeric layer at high voltage above 2.0 V, respectively. In the subsequent cycles, the u-MnO₂/CNFs composites tend to be more stable with only slight shift of the distinct cathodic and anodic peaks, compared to that of u-MnO₂, indicating the highly reversible redox reactions of the electrodes ($\text{MnO}_2 + 4\text{Li} + 4\text{e}^- \leftrightarrow 2\text{Li}_2\text{O} + \text{Mn}$). Fig. 2-13c and d presents the galvanostatic charge and discharge curves in the first two cycles at a current density of 0.1 C. The initial discharge and charge capacities of bare u-MnO₂ are calculated to be 346 and 312 mAh g⁻¹ with a Coulombic efficiency of 90% and those of the u-MnO₂/CNFs nanocomposite are 1064 and 703 mAh g⁻¹ with a Coulombic efficiency of 60%. This high capacity loss of the u-MnO₂/CNFs nanocomposite can be attributed to the formation of the irreversible SEI layer and the Li⁺ trapped in the CNFs. The initial discharge and charge capacities of the u-MnO₂/CNFs nanocomposite are superior to that of bare u-MnO₂ due to the incorporation of CNFs. In the second cycle, the discharge and charge capacity of the u-MnO₂/CNFs nanocomposite delivers 685 and 701 mAh g⁻¹ with a Coulombic efficiency of 102%.

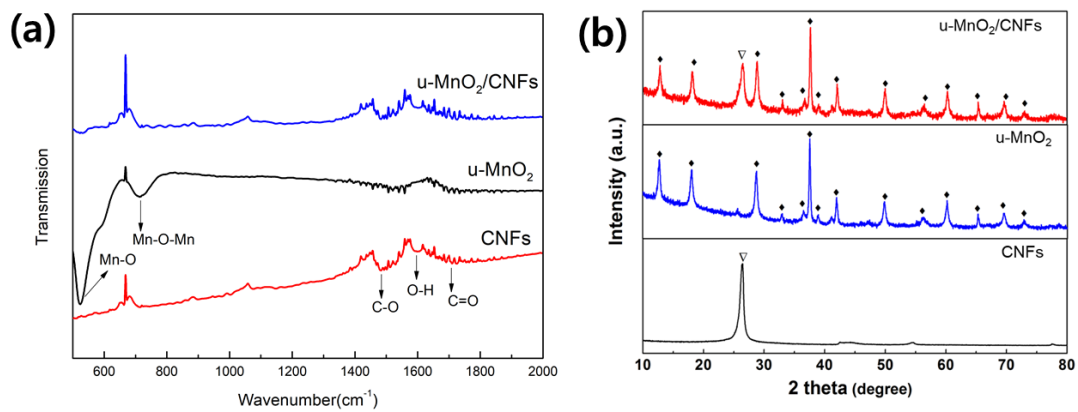


Fig. 2-11 (a) FT-IR spectra and (b) XRD patterns for CNFs, u-MnO₂, and u-MnO₂/CNFs composite

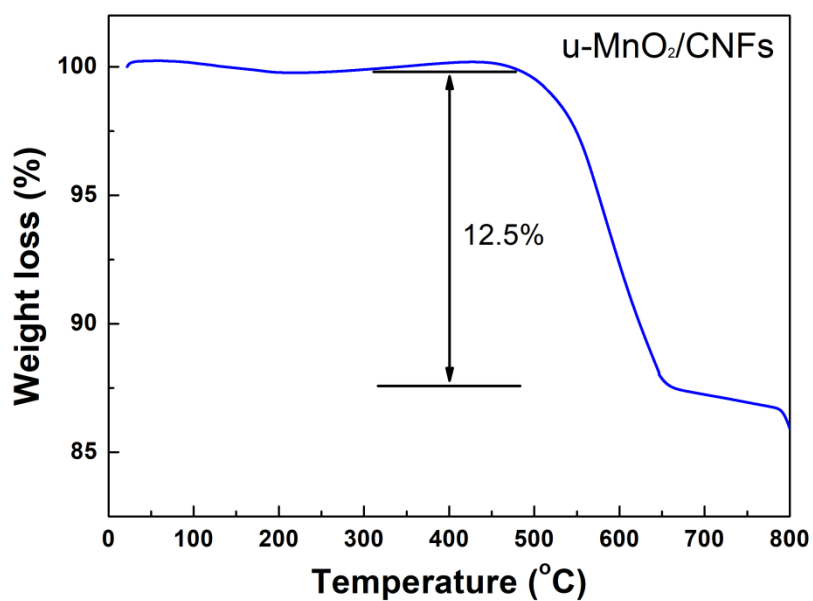


Fig. 2-12 TGA curve of the u-MnO₂/CNFs composite

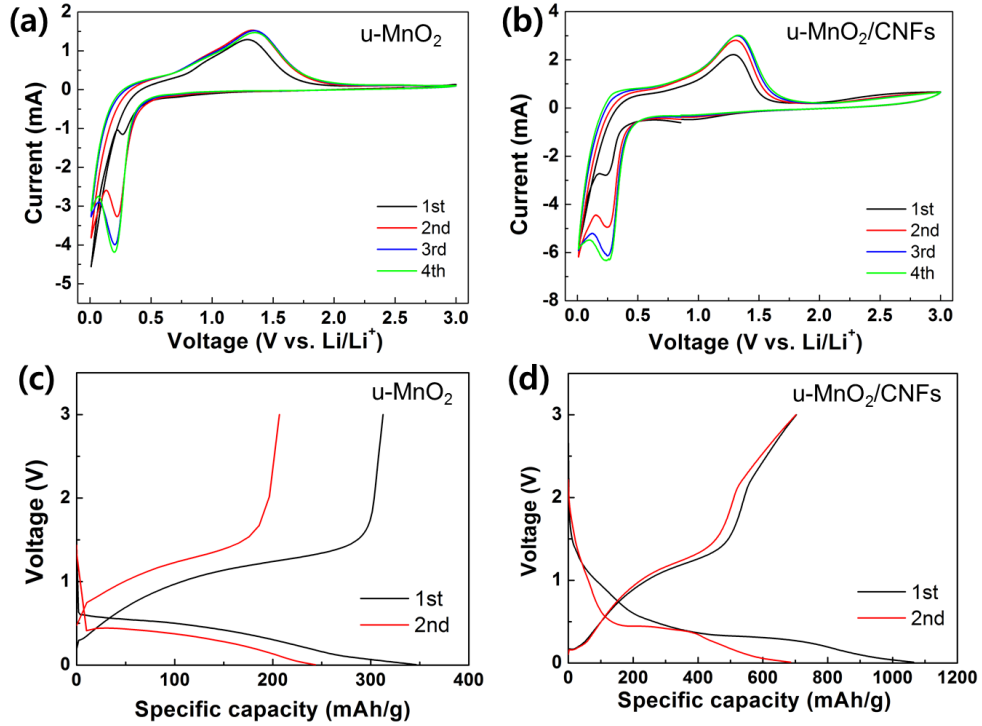


Fig. 2-13 The first four CV curves of (a) bare u-MnO₂ and (b) u-MnO₂/CNFs nanocomposite. Charge-discharge curves at 0.1 C of (c) bare u-MnO₂ and (d) u-MnO₂/CNFs nanocomposite.

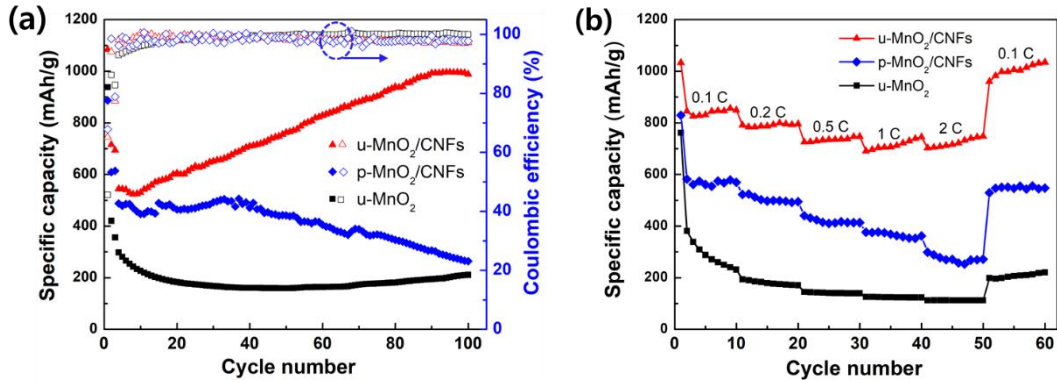


Fig. 2-14 (a) The cycle performance and (b) the rate performance of bare u-MnO₂, u-MnO₂/CNFs nanocomposite, and p-MnO₂/CNFs nanocomposite.

The cycling performance of the bare u-MnO₂, u-MnO₂/CNFs nanocomposite, and p-MnO₂/CNFs nanocomposite was further evaluated at the current density of 0.1 C for the first two cycles and 0.5 C for other cycles. Fig. 2-14a clearly shows that the discharge capacity of the u-MnO₂/CNFs nanocomposite is superior over the cycles because CNFs contribute to enhance the discharge capacity by improving the electrical conductivity and providing additional reaction sites with Li, because the surface of oxidized CNFs has oxygen containing functional groups such as hydroxyl groups which can act as active sites (Fig. 2-11a) [34]. The initial discharge capacity of the u-MnO₂/CNFs nanocomposite is 1083 mAh g⁻¹ and reaches 988 mAh g⁻¹ with 91% retention after 100 cycles, whereas only 21 and 30% retention were obtained from the initial capacity of 938 and 886 mAh g⁻¹ for the bare u-MnO₂ and p-MnO₂/CNFs nanocomposite electrode. This fast capacity decay of the bare u-MnO₂ electrode is ascribed to the large volume change of MnO₂ during the discharge/charge process, resulting in the destruction of the electrical connection between the u-MnO₂ and conductive carbon. Also, the superior cycle performance, compared to the p-MnO₂/CNFs nanocomposite, is related to the hierarchical nanostructure of u-MnO₂/CNFs nanocomposite, which creates fast electrochemical accessibility of the electrolyte and ions to the active sites and facilitate the efficient contact between active materials and the electrolyte for fast kinetics. Another interesting observation is that the discharge capacity of the u-MnO₂/CNFs nanocomposite shows a gradual increase after the 8th cycle in the subsequent 100 cycles and remains stable about 990 mAh g⁻¹. Such increase in capacity may be attributed to the additional Li ion interaction with the u-MnO₂/CNFs electrode and the formation of the polymeric gel-like layer on the transition metal oxide MnO₂ with better electrolyte infiltration during cycling [35–37]. In addition, the discharge capacity of the u-MnO₂/CNFs nanocomposite after 200 cycles was maintained with slight decrease along cycles (Fig. 2-15). After cycle test, the morphology of u-MnO₂/CNFs electrode was also well preserved without obvious physical change (Fig. 2-16), indicating a good stability of u-MnO₂/CNFs composite. The rate performances of the bare u-MnO₂ and u-MnO₂/CNFs nanocomposite were tested at different current densities, as shown in Fig. 2-14b. It can be seen that the u-MnO₂/CNFs nanocomposite exhibits superior rate

capability with average capacity of 849, 796, 747, 745, and 748 mAh g⁻¹ at current rate densities of 0.1 C, 0.2 C, 0.5 C, 1 C, and 2 C, respectively. For the bare u-MnO₂ electrode, the obtained average capacities are 231, 170, 139, 123, and 112 mAh g⁻¹ at the same current densities, respectively. When the current density returned to 0.1 C, the capacity of the u-MnO₂/CNFs nanocomposite restored to 960 mAh g⁻¹, displaying an excellent rate capability performance. These improved electrochemical performances of the u-MnO₂/CNFs nanocomposite can be attributed to the unique hierarchical structure of u-MnO₂ with well-dispersed CNFs, which provides additional electrochemical active sites and defects available for Li ion insertion, enhanced electrical conductivity, and limit the volume change.

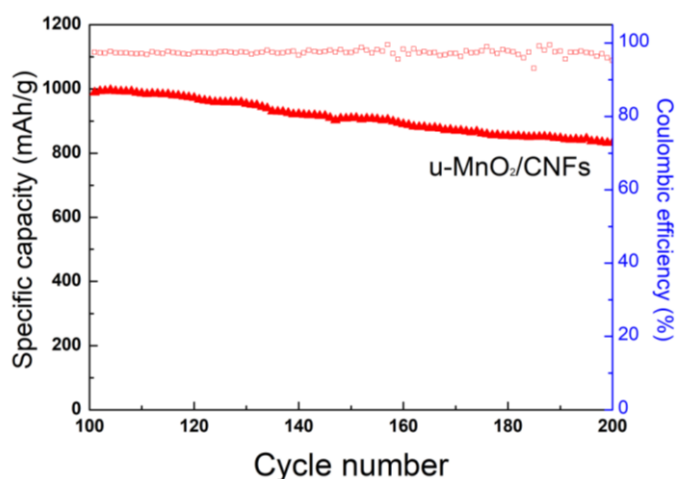


Fig. 2-15 The cycle performance from 100 to 200 cycles for the u-MnO₂/CNFs composite

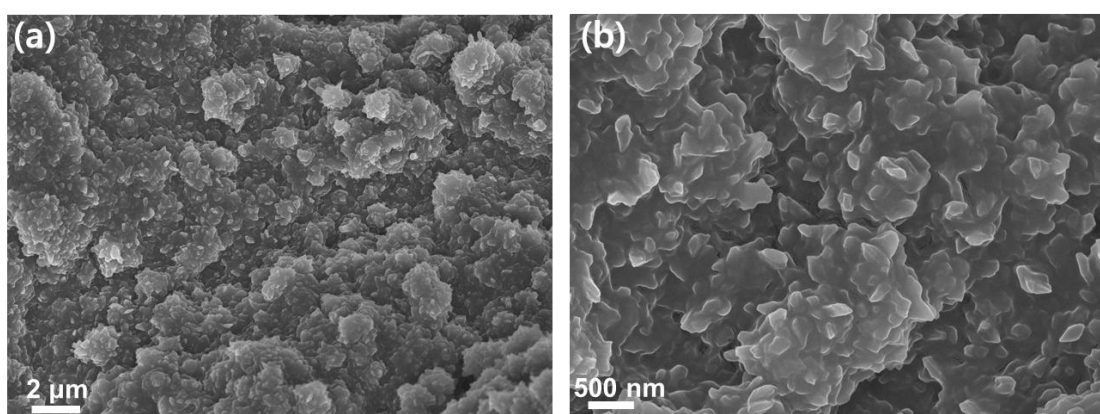


Fig. 2-16 (a-b) FE-SEM images of the u-MnO₂/CNFs electrode after 100 cycles test.

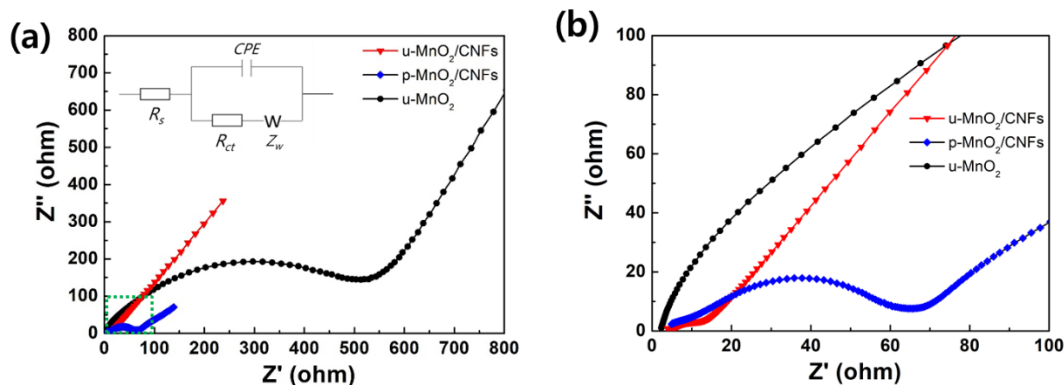


Fig. 2-17 (a) Nyquist plots with inset of equivalent circuit of bare u-MnO₂, u-MnO₂/CNFs nanocomposite, and p-MnO₂/CNFs nanocomposite, and (b) its magnified plots.

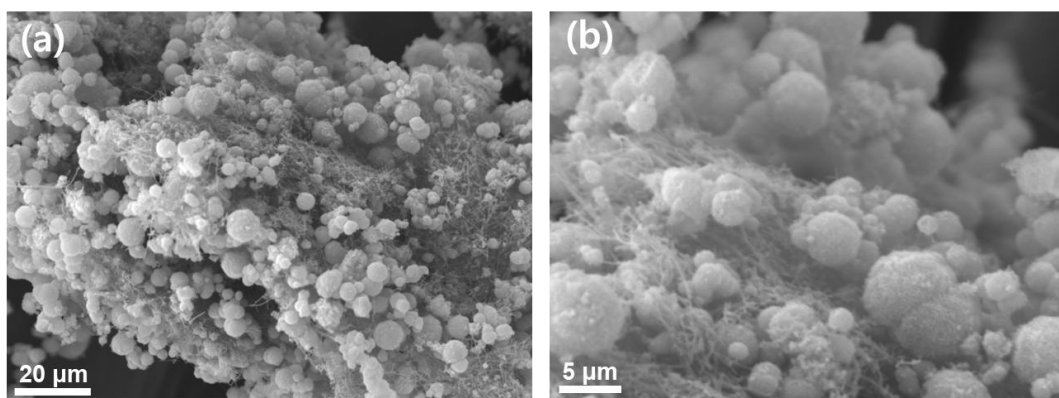


Fig. 2-18 (a-b) FE-SEM images of the p-MnO₂/CNFs nanocomposites

Electrochemical impedance spectroscopy (EIS) measurements of the bare u-MnO₂, u-MnO₂/CNFs nanocomposite, p-MnO₂/CNFs nanocomposite were carried out and the resulting Nyquist plots with an equivalent circuit are shown in Fig. 2-17. The diameter of the semicircle in the high-middle frequency region can be assigned to the charge-transfer resistance (R_{ct}), and the diameter of the semicircle for the u-MnO₂/CNFs nanocomposite is much smaller than that of the bare u-MnO₂. The calculated R_{ct} of u-MnO₂/CNFs nanocomposite is 5.3 Ω , whereas those of bare u-MnO₂ and p-MnO₂/CNFs nanocomposite are 250 and 45.6 Ω . This stiff drop of R_{ct} suggests that CNFs in nanocomposite can facilitate fast electron and Li ion transfer, and enhance electrical conductivity, resulting in the highly enhanced electrochemical performance of the uMnO₂/CNFs nanocomposite. In addition, the lower R_{ct} can be ascribed to the structural feature of u-MnO₂ which would be beneficial for the

uniform distribution of CNFs in the nanocomposite, comparing to the poor mixture morphology of the p-MnO₂/CNFs nanocomposite (Fig. 2-18).

2.6 Conclusion

In summary, we successfully demonstrated the synthesis of hierarchical u-MnO₂ and its nanocomposites with CNFs for the application of a Li-ion anode electrode. The hierarchical hollow urchin-like MnO₂ structures are obtained by controlling the hydrothermal reaction time. For improving electrical conductivity, the u-MnO₂/CNFs nanocomposite is prepared, which is beneficial for maximizing the utilization of hierarchical structures of u-MnO₂. When used as anode electrode of a Li-ion battery, the u-MnO₂/CNFs nanocomposite exhibits excellent electrochemical performance of superior cycle capacity as well as high rate capacity. These outstanding performances are attributed to the unique hierarchical structure and synergetic hybridization of u-MnO₂ and CNFs which facilitates faster electron and Li ion transfer.

2.7 References

- [1] R. Marom, S.F. Amalraj, N. Leifer, J. David, A. Doron, *J. Mater. Chem.* 21 (2011) 9938–9954.
- [2] M.S. Cao, X.X. Wang, W.Q. Cao, X.Y. Fang, B. Wen, J. Yuan, *Small* 14 (2018) 1800987.
- [3] B.K. Guo, X.Q. Wang, P.F. Fulvio, M.F. Chi, S.M. Mahurin, X.G. Sun, S. Dai, *Adv. Mater.* 23 (2011) 4661–4666.
- [4] L. Qie, W.M. Chen, Z.H. Wang, Q.G. Shao, X. Li, L.X. Yuan, X.L. Hu, W.X. Zhang, Y.H. Huang, *Adv. Mater.* 24 (2012) 2047–2050.
- [5] W.Q. Cao, W.Z. Wang, H.L. Shi, J. Wang, M.S. Cao, Y.J. Liang, M. Zhu, *Nano Res.* 11 (2018) 1437–1446.
- [6] M.S. Wu, P.C.J. Chiang, J.T. Lee, J.C. Jin, *J. Phys. Chem. B* 109 (2005) 23279–23284.
- [7] Z.Y. Zhong, Y.D. Lin, B. Gates, Y.N. Xia, *Adv. Mater.* 12 (2000) 206–209.
- [8] D. Gu, H. Bongard, Y.H. Deng, D. Feng, Z.X. Wu, Y. Fang, J.J. Mao, B. Tu, F.

- Schuth, D.Y. Zhao, *Adv. Mater.* 22 (2010) 833–837.
- [9] P.M. Arnal, C. Weidenthaler, F. Schuth, *Chem. Mater.* 18 (2006) 2733–2739.
- [10] P.M. Arnal, F. Schuth, F. Kleitz, *Chem. Commun.* 11 (2006) 1203–1205.
- [11] B. Smarsly, D. Grosso, T. Brezesinski, N. Pinna, C. Boissiere, M. Antonietti, C. Sanchez, *Chem. Mater.* 16 (2004) 2948–2952.
- [12] M.S. Wu, P.C.J. Chiang, J.T. Lee, J.C. Jin, *J. Phys. Chem. B* 109 (2005) 23279–23284.
- [13] A. Yu, H.W. Park, A. Davies, D.C. Higgins, Z. Chen, X. Xiao, *J. Phys. Chem. Lett.* 2 (2011) 1855–1860.
- [14] A.L.M. Reddy, M.M. Shaijumon, S.R. Gowda, P.M. Ajayan, *Nano Lett.* 9 (2009) 1002–1006.
- [15] P. Poizot, S. Laruelle, S. Grugeon, L. Dupont, J.-M. Tarascon, *Nature* 407 (2000) 496–499.
- [16] H. Xia, Y. Wang, J. Lin, L. Lu, *Nanoscale Res. Lett.* 7 (2012) 33.
- [17] P. Umek, A. Gloter, M. Pregelj, R. Dominko, M. Jagodic, Z. Jaglicic, A. Zimina, M. Brzhezinskaya, A. Potocnik, C. Filipic, A. Levstik, D. Arcon, *J. Phys. Chem. C* 113 (2009) 14798–14803.
- [18] J. Ni, W. Lu, L. Zhang, B. Yue, X. Shang, Y. Lv, *J. Phys. Chem. C* 113 (2008) 54–60.
- [19] H.Q. Wang, Z.S. Li, Y.G. Huang, Q.Y. Li, X.Y. Wang, *J. Mater. Chem.* 20 (2010) 3883–3889.
- [20] H. Zhang, G.P. Cao, Z.Y. Wang, Y.S. Yang, Z.J. Shi, Z.N. Gu, *Nano Lett.* 8 (2008) 2664–2668.
- [21] W. Zhang, Z. Yang, X. Wang, Y. Zhang, X. Wen, S. Yang, *Catal. Commun.* 7 (2006) 408–412.
- [22] H. Xia, J. Feng, H. Wang, M.O. Lai, L. Lu, *J. Power Sources* 195 (2010) 4410–4413.
- [23] H.T. Zhu, J. Luo, H.X. Yang, J.K. Liang, G.H. Rao, J.B. Li, Z.M. Du, *J. Phys. Chem. C* 112 (2008) 17089–17094.
- [24] D. Yan, P. Yan, S. Cheng, J. Chen, R. Zhuo, J. Feng, G.A. Zhang, *Cryst. Growth Des.* 9 (2008) 218–222.

- [25] S. Zhao, T. Liu, D. Shi, Y. Zhang, W. Zeng, T. Li, B. Miao, *Appl. Surf. Sci.* 351 (2015) 862–868.
- [26] X.C. Song, Y. Zhao, Y.F. Zheng, *Cryst. Growth Des.* 7 (2007) 159–162.
- [27] W. Yang, Z. Gao, J. Wang, B. Wang, Q. Liu, Z. Li, T. Mann, P. Yang, M. Zhang, L. Liu, *Electrochim. Acta* 69 (2012) 112–119.
- [28] M. Zhou, X. Zhang, J.M. Wei, S.L. Zhao, L. Wang, B.X. Feng, *J. Phys. Chem. C* 115 (2010) 1398–1402.
- [29] B. Li, G. Rong, Y. Xie, L. Huang, C. Feng, *Inorg. Chem.* 45 (2006) 6404–6410.
- [30] L. Li, A.-R.O. Raji, J.M. Tour, *Adv. Mater.* 25 (2013) 6298–6302.
- [31] H. Xia, M. Lai, L. Lu, *J. Mater. Chem.* 20 (2010) 6896–6902.
- [32] J.G. Wang, Y. Yang, Z.H. Huang, F. Kang, *J. Mater. Chem.* 22 (2012) 16943–16949.
- [33] X. Wang, Y. Li, *J. Am. Chem. Soc.* 124 (2002) 2880–2881.
- [34] L. Yue, W. Li, F. Sun, L. Zhao, L. Xing, *Carbon* 48 (2010) 3079–3090.
- [35] S. Grugeon, S. Laruelle, L. Dupont, J.-M. Tarascon, *Solid State Sci.* 5 (2003) 895–904.
- [36] X. Gu, J. Yue, L. Li, H. Xue, J. Yang, X. Zhao, *Electrochim. Acta* 184 (2015) 250–256.
- [37] J. Mujtaba, H.Y. Sun, G.Y. Huang, K. Mødhav, Y.G. Liu, Y.Y. Zhao, X. Wang, S.M. Xu, J. Zhu, *Sci. Rep.* 6 (2016) 20592.

CHAPTER 3 Fabrication of g-C₃N₄ quantum dots/MnCO₃ nanocomposite on carbon cloth as a binder-free electrode for supercapacitors

3.1 Introduction

Supercapacitors have attracted considerable attention for the application of advanced energy storage devices of electronic vehicles and portable electronic devices due to their beneficial properties such as excellent power density, rapid charging time, and durability [1]. Electric double layer capacitors (EDLC) mainly use various carbon-based materials, such as activated carbon, carbon nanotubes (CNTs), and graphene. In EDLC, an accumulation of ionic charges occurs between the electrode and electrolyte of carbon-based electrodes, and carbon-based electrodes with large surface areas deliver high power density and long cycle stability. On the other hand, pseudocapacitors can exhibit substantially high specific capacitance and high energy density compared to EDLC, owing to the fast and reversible surface Faradaic redox reaction. In addition, transition metal oxide and carbonate materials have been explored as electrode materials of pseudocapacitors due to their high theoretical storage capacity and superior reversibility. Among them, Mn-based active materials have attracted a great deal of interest owing to the high theoretical capacitance, low cost, and natural abundance [2–5]. However, most research has been done with Mn-based oxides, and manganese carbonates (MnCO₃) are relatively new and popular active materials for pseudocapacitors. Recently, MnCO₃ has been extensively studied as a potential electrode of supercapacitors due to the low manganese valence state of +2 and the redox process to high manganese valence states (+3 or +4), which could show high electrochemical performance. The low manganese valence (+2) in MnCO₃ can exhibit a better hydroxyl ions insertion of alkaline electrolytes for the formation of MnOHCO₃ compared to high manganese valence states (+3 or +4) [5–7]. However, low electrical conductivity and poor cycle stability restrict the application of MnCO₃ as an active material in energy storage applications. To overcome these drawbacks, an effective

approach is to hybridize MnCO_3 using conductive carbon-based additives such as carbon [8], CNTs [9,10], and graphene [11–14], which have proved to be effective to improve electrochemical performance.

Graphitic carbon nitride ($\text{g-C}_3\text{N}_4$) recently attracted a lot of interest as a promising electrode candidate for electrochemical devices due to its high nitrogen content, good structural stability, and low interfacial impedance. Thus, $\text{g-C}_3\text{N}_4$ was employed in the transition metal oxides or hydroxide-based electrodes for supercapacitors. Chang et al. [15] synthesized novel sandwich-like $\text{MnO}_2/\text{g-C}_3\text{N}_4$ composites for supercapacitor electrodes and showed the enhanced electrochemical performance, which was ascribed to various active sites and the existence of N of $\text{g-C}_3\text{N}_4$ for better wettability with electrolytes. Gao et al. [16] reported the enduring supercapacitance using $\text{MnO}_2/\text{protonated g-C}_3\text{N}_4$. It showed that the strong hydrogen bonding between MnO_2 and the $\text{g-C}_3\text{N}_4$ can restrain particle agglomeration in the cycling test, resulting in stable energy storage performance. Ding et al. [17] fabricated the honeycomb nanostructured $\text{g-C}_3\text{N}_4@\text{Ni}(\text{OH})_2$ for an asymmetric supercapacitor, where the $\text{g-C}_3\text{N}_4$ showed a good charge transport with good chemical stability. However, there are limited reports studying the application of $\text{g-C}_3\text{N}_4$ quantum dots (CNQDs) in energy storage fields.

Herein, we report a simple hydrothermal process to prepare the nanostructured MnCO_3 and CNQDs nanocomposites on carbon cloth (denoted as q-MC//CC). The active material of MnCO_3 and CNQDs nanocomposites is synthesized directly on the carbon cloth as a flexible conductive substrate, which is then also used for an electrode of a solid-state flexible asymmetric supercapacitor (ASC). MnCO_3 and CNQDs nanocomposites exhibit excellent electrochemical performance, including good specific capacitance and rate capability, which is attributed to the enhanced electrical conductivity and shorter ions pathway. Moreover, CNQDs have generally large surface areas and accessible edges that can function as active sites of electrochemical reaction, which would improve the electrochemical performance. The q-MC//CC electrode delivers a high specific capacitance of 1001.4 F g^{-1} under a current density of 1 A g^{-1} as well as good cycling performance (96% capacity retention). Furthermore, a solid-state binder-free flexible ASC using q-MC//CC

electrode is demonstrated, showing a high energy density of 27.1 Wh kg^{-1} at a power density of 500 W kg^{-1} and good mechanical stability.

3.2 Materials and Methods

3.2.1 Preparation of g-C₃N₄ Quantum Dots

First, 5 g of melamine were calcinated in a muffle furnace at $550 \text{ }^\circ\text{C}$ for 4 h to obtain bulk g-C₃N₄. Then, 2 g of bulk g-C₃N₄ were treated in a mixture solution of sulfuric acid (40 mL) and nitric acid (40 mL) for about 2 h at room temperature. Then, the mixture was rinsed several times with deionized (DI) water, and the as-obtained white product was dispersed in the concentrated NH₃ H₂O. The mixture solution was transferred into a Teflon-lined stainless-steel autoclave with heating at $180 \text{ }^\circ\text{C}$ for 12 h. After the hydrothermal process, the precipitate was rinsed with DI water to remove residual NH₃ molecules. Subsequently, the treated g-C₃N₄ nanosheets were dispersed and sonicated in 100 mL water for 6 h, and the as-obtained aqueous suspension was centrifuged at 7000 rpm and dialyzed in a dialysis bag (3000 Da, Spectrum Lab. Inc) for 48 h to remove large particles. Finally, the CNQDs solution was obtained.

3.2.2 Synthesis of q-MC//CC Nanocomposites

First, carbon cloth was treated by immersing in a mixture acid solution (H₂SO₄:HNO₃ = 1:3) at room temperature for 24 h and then washed with DI water. For the typical synthesis of q-MC//CC nanocomposites (Figure 3-1), MnSO₄ H₂O (3.38 g) was dissolved in DI water (134 mL), and NH₄F (0.6 g) was added to the above solution with stirring to form a transparent solution. After several minutes, urea (2.4 g) and 5 mg of CNQDs was added to the above homogeneous solution with 30 min stirring at room temperature. Then, the treated carbon cloth ($3 \times 1 \text{ cm}^2$) was immersed into the mixture solution and treated with the hydrothermal process, maintaining at $120 \text{ }^\circ\text{C}$ for 4 h. The obtained q-MC//CC nanocomposites were washed with DI water to remove the residual reactants and dried at $60 \text{ }^\circ\text{C}$. As a control sample, the MnCO₃ on carbon cloth sample was also synthesized by following the same procedure without adding CNQDs

(denoted as MC//CC).

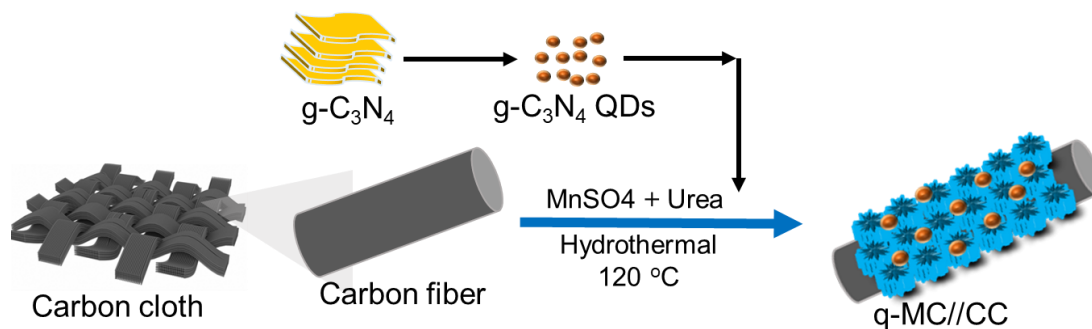


Fig. 3-1 Schematic illustration for the synthesis of g-C₃N₄ quantum dots/MnCO₃ nanocomposite on carbon cloth.

3.3 Characterization

A transmission electron microscope (TEM, H-8100, Hitachi, Tokyo, Japan) and a field-emission scanning electron microscope (FE-SEM, JEOL-JSM820, JEOL Ltd., Akishima-shi, Japan) were used to investigate the morphology of the obtained samples. X-ray photoelectron spectroscopy (XPS, K-alpha, Thermo Fisher, Waltham, MA, USA) measurements were carried out using monochromatic AlK α radiation ($h\nu = 1486.6$ eV). Contact angle measurements with electrolyte (1.0 M Na₂SO₄) droplets were performed to investigate the wettability of the q-MC//CC electrode using an Attension Theta Optical Tensiometer (Biolin Scientific AB, Stockholm, Sweden). Fourier transform infrared (FTIR) spectra were collected using a Nicolet IR 200 FT-IR spectrometer (Thermo Scientific, Waltham, MA, USA), and Raman spectroscopy (DXR Raman spectrometer, Thermo Scientific, Madison, WI, USA) was performed with a 532 nm excitation source.

3.4 Electrochemical Measurement

Electrochemical performance was investigated by cyclic voltammetry (CV), galvanostatic charge/discharge (GCD), and electrochemical impedance spectroscopy (EIS) tests. All electrochemical measurements were performed using a BioLogic VSP

electrochemical workstation at room temperature. A three-electrode system was used to test the electrochemical performance of the prepared electrodes with platinum wire and Ag/AgCl electrodes as the counter and reference electrodes, respectively. The obtained products such as MC//CC and q-MC//CC ($1 \times 1 \text{ cm}^2$) are directly used as working electrodes. The mass loading of active materials (MC//CC and q-MC//CC) of tested electrode was about 2.5 mg in this work. All electrochemical tests were performed in an aqueous electrolyte of 1 M Na_2SO_4 at room temperature. EIS was performed at open circuit potential in a frequency range from 10 kHz to 0.01 Hz with an AC amplitude of 5 mV. The solid-state flexible ASC were prepared using the q-MC//CC and carbon cloth as positive and negative electrodes, respectively, which were assembled with PVA/ Na_2SO_4 gel electrolyte and filter paper as a separator. The prepared two electrodes were wetted with the PVA/ Na_2SO_4 gel electrolyte for 10 min and then assembled face to face with filter paper using gentle pressure. The specific capacitance (C_s) of the product can be calculated from the CV curves and galvanostatic charge-discharge curves according to the following equation:

$$C_s = \frac{\int I(V) dV}{v \times m \times \Delta V} \quad (1)$$

$$C_s = \frac{I \times \Delta t}{m \times \Delta V} \quad (2)$$

where $\int I(V) dV$ is the area enclosed by the CV curves, ΔV (V) is the potential window, v (mV s^{-1}) is the potential scan rate, m (g) is the mass of the active materials in the electrodes, and Δt (s) is the discharge time.

3.5 Results and discussion

Figure 3-2a,b show FE-SEM images of as-prepared q-MC//CC nanocomposites. The pristine carbon cloth shows a smooth surface consisting of aligned carbon fiber bundles. After the hydrothermal reaction of the synthesis of q-MC//CC, it is observed that clusters of spindle-shaped petals of MnCO_3 were densely grown on the surface of carbon fibers. In addition, the prepared q-MC//CC sample shows good flexibility, as shown in the inset of Figure 3-2a. The morphology of MC//CC (Figure 3-3) has a similar nanostructure to that of q-MC//CC, showing that the addition of CNQDs has no effect on the morphological formation of MnCO_3 . The TEM image (Figure 3-2c)

of the q-MC//CC confirms that the CNQDs are uniformly embedded in MnCO_3 , and the lattice fringe of CNQDs is found in the high resolution TEM (HRTEM) image (Figure 3-2d), where a lattice distance is 0.336 nm, corresponding to the (002) planes of g-C₃N₄. The SEM image of q-MC//CC and its elemental mapping from energy-dispersive X-ray spectroscopy (EDS) reveal the existence of the expected atomic elements (Figure 3-2e), which clearly confirms that Mn, C, and N elements are uniformly distributed on the MnCO_3 surface and the successful formation of q-MC//CC nanocomposite. In addition, the obtained q-MC//CC has a larger surface area ($182 \text{ m}^2/\text{g}$) than the pristine carbon cloth ($69 \text{ m}^2/\text{g}$) due to its unique nanostructure (Figure 3-4).

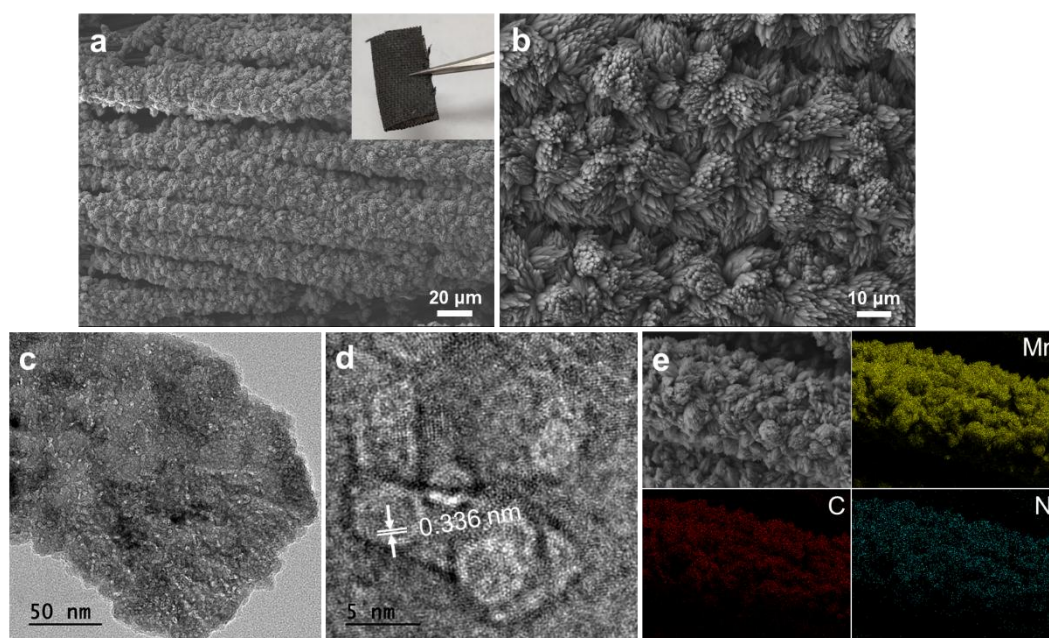


Fig. 3-2 (a-b) SEM images of q-MC//CC. (c) TEM image of q-MC//CC and (d) its high magnification image. (e) EDS elementary mapping of q-MC//CC.

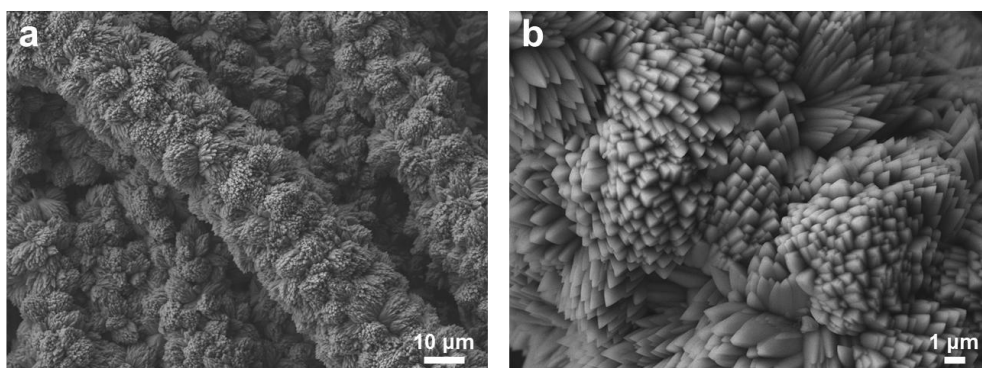


Fig. 3-3 (a-b) SEM images of as-synthesized MC//CC.

An XPS study was performed to characterize the chemical compositions of the q-MC//CC. The XPS survey scans in Figure 3-5a show that both q-MC//CC and MC//CC samples contain the Mn, O, and C atoms, while the N peak is only found in the q-MC//CC nanocomposites due to CNQDs. The deconvolution of the Mn 2p spectrum of q-MC//CC (Figure 3-5b) displays two peaks located at 655.8 eV and 643.8 eV respectively, assigning to Mn 2p^{1/2} and Mn 2p^{3/2} with an energy separation of 12.0 eV, which coincides with Mn²⁺ [18,19]. In the high-resolution C1s spectrum of q-MC//CC (Figure 3-5c) and MC//CC (Figure 3-6), two typical peaks of the C-C bond at 284.6 eV and C=O bond at 288.5 eV are observed, relating to the surface carbon of the carbon cloth and carbon element in carbonate ions [20]. In addition, two additional peaks at 286.0 and 292.7 eV are only observed for q-MC//CC, which for q-MC//CC, which correspond to the C-N bond and carboxylate bond of CNQDs, respectively.

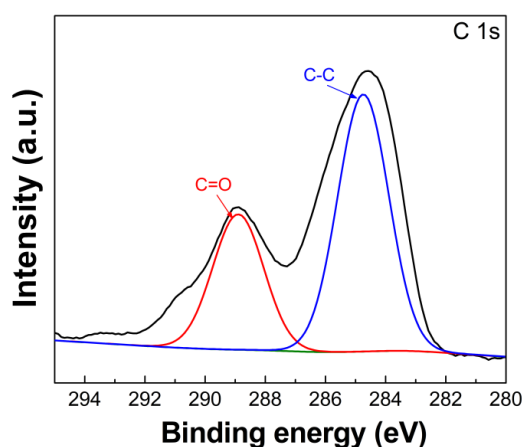


Fig. 3-4 High resolution C 1s XPS spectrum of MC//CC.

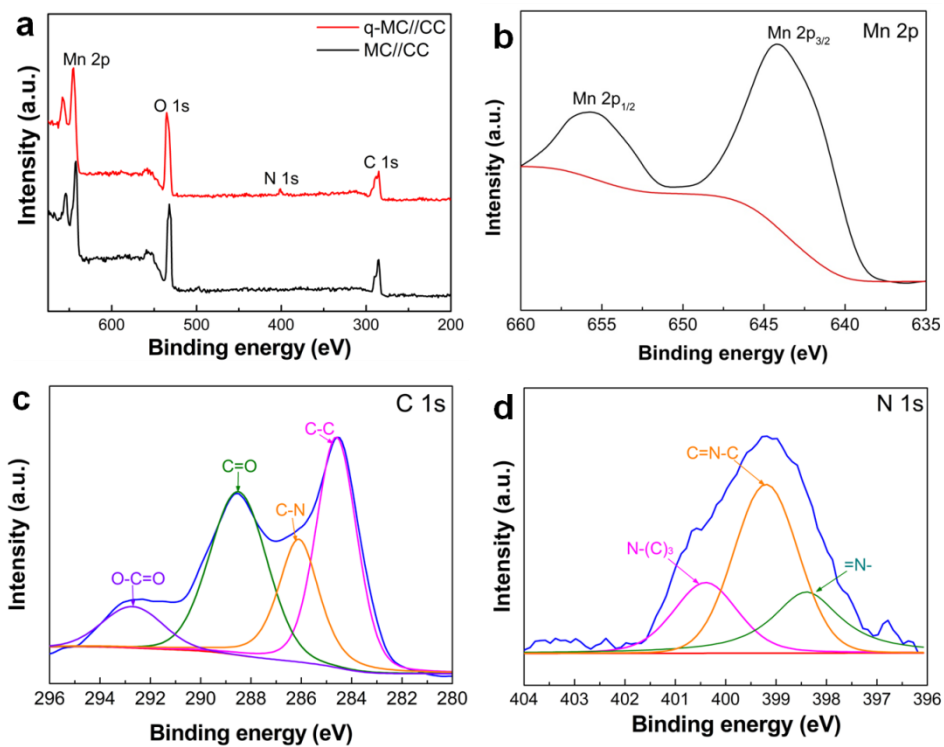


Fig. 3-5 (a) The XPS survey scan of q-MC//CC and MC//CC. (b-d) High resolution XPS spectrum of Mn 2p, C 1s, and N 1s of q-MC//CC, respectively.

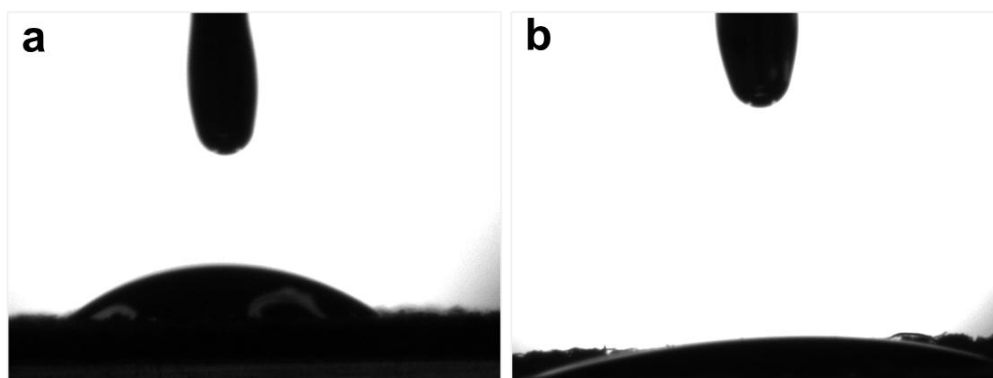


Fig. 3-6 Image of the contact angle measurement of (a) MC//CC and (b) q-MC//CC with 1M Na₂SO₄ electrolyte

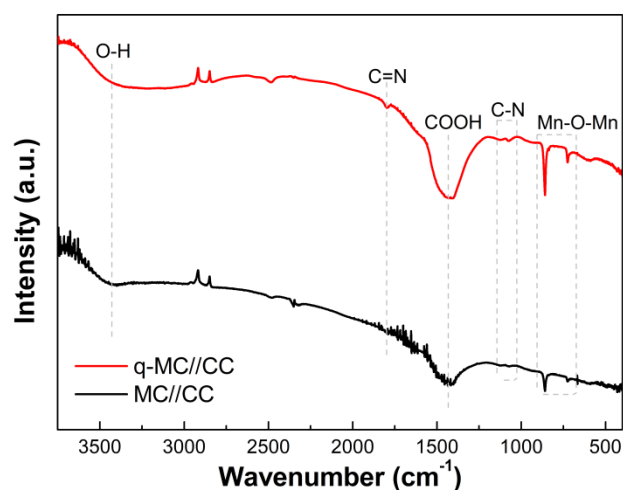


Fig. 3-7 FT-IR spectrum for q-MC//CC and MC//CC.

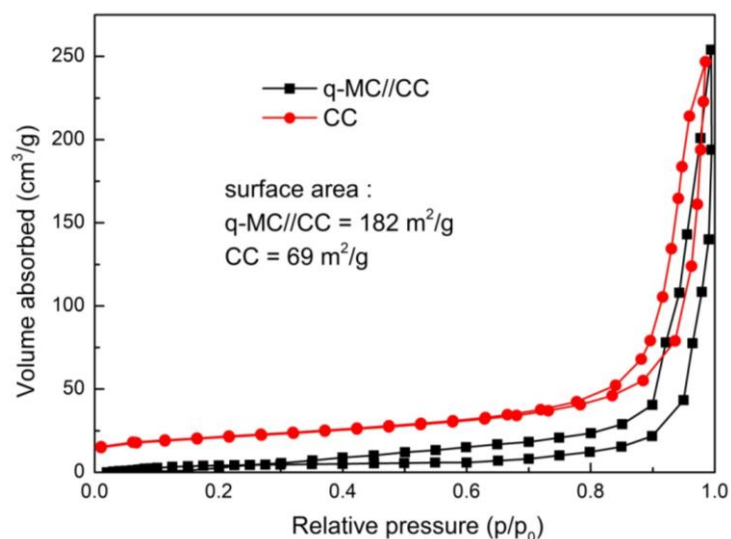


Fig. 3-8 N₂ adsorption/desorption isotherms for CC and q-MC//CC composite

In addition, the high-resolution N 1s spectrum of q-MC//CC can be fitted into three peaks, as shown in Figure 3-5d, corresponding to =N- (398.4 eV), C=N-C (399.1 eV), and N-(C)₃ (400.4 eV) [21], indicating the presence of CNQDs in the q-MC//CC nanocomposite. The contact angle measurements with 1 M Na₂SO₄ electrolyte were performed to study the effect of CNQDs on the surface wettability of the prepared q-MC//CC composite. Figure 3-7 illustrates the images of electrolyte droplets on the prepared MC//CC and q-MC//CC composites, respectively. The q-MC//CC composite shows a lower contact angle with Na₂SO₄ electrolyte than MC//CC, which is due to the more ion-accessible surfaces by CNQDs. This enhanced

surface wettability of the q-MC//CC composite facilitates the accessibility of electrolyte, leading to better electrochemical performance compared to the MC//CC composite. In addition, the FTIR spectra of the as-prepared q-MC//CC and MC//CC are shown in Figure 3-8. The characteristic peak of the Mn-O-Mn bond is observed at 727 cm^{-1} for both samples, while that of the characteristic peaks corresponding to the C-N (1033 cm^{-1}) and C=N bonds (1780 cm^{-1}) are only found for q-MC//CC due to the existence of CNQDs.

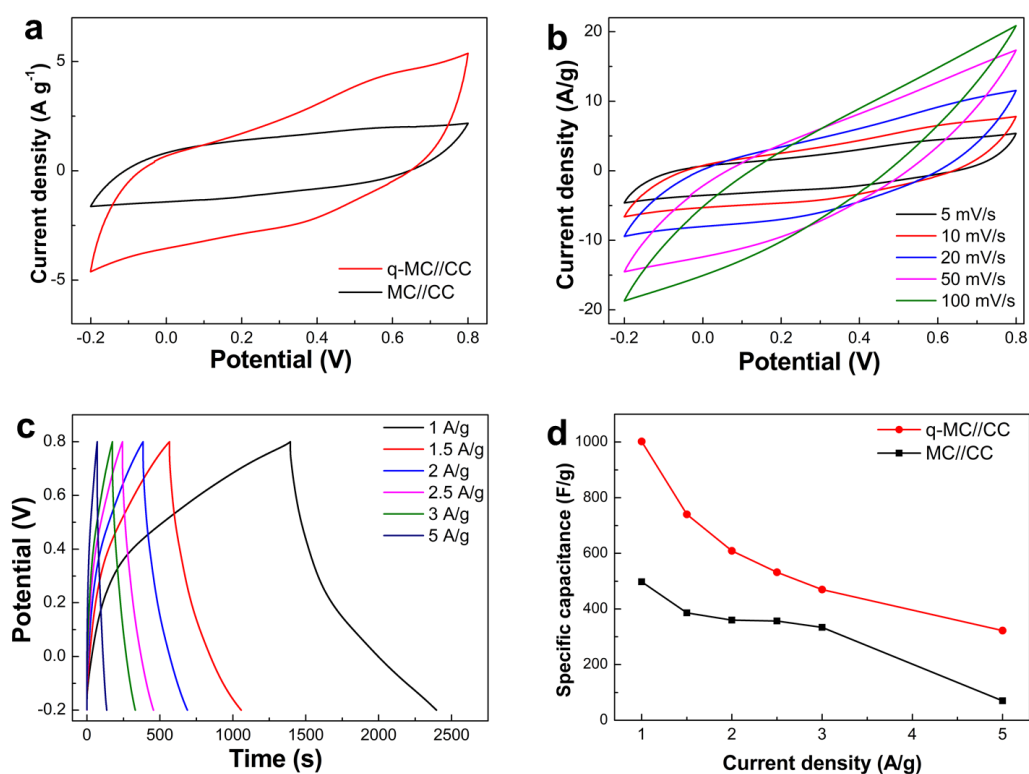


Fig. 3-9 (a) CV curves of q-MC//CC and MC//CC. (b) CV curves of q-MC//CC at different scan rates. (c) Galvanostatic charge-discharge curves of q-MC//CC at different current densities. (d) Obtained specific capacitance of q-MC//CC at different current densities.

The electrochemical performances of q-MC//CC composites as binder-free electrodes of supercapacitors are studied using CV and GCD characterization in 1 M Na_2SO_4 aqueous electrolyte using a three-electrode system. Figure 3-9a shows the CV curves of q-MC//CC and MC//CC measured at a scan rate of 5 mV s^{-1} with potentials

ranging from -0.2 to 0.8 V. CV curves of both electrodes show rectangular shapes in a potential window, indicating excellent capacitive behavior. The larger integral area of the CV curve for q-MC//CC electrode suggests higher specific capacitance than the MC//CC electrode, which represents its superior electrochemical property due to the synergistic effects of CNQDs and MnCO₃. The CV curves of q-MC//CC measured at different scan rates from 5 mV s⁻¹ to 100 mV s⁻¹ are shown in Figure 3-9b. The CV curve shapes are maintained upon increasing the scan rate, revealing fast ionic and electronic transportation. The current response also simultaneously increases along with the scan rate, showing a diffusion-controlled phenomenon. The GCD measurement of the q-MC//CC electrode was performed at different current density (Figure 3-9c). All GCD curves show some linear and symmetric behavior, indicating capacitive characteristics and good reversibility of the q-MC//CC electrode. In addition, a noticeable potential drop at the discharge plot is not observed, suggesting the low internal resistance of the q-MC//CC electrode. The specific capacitance decreases with increasing current densities, due to slow ionic diffusion at high current. Figure 3-9d compares the calculated specific capacitance of q-MC//CC and MC//CC electrodes at current densities. It demonstrates the superior capacitive performance of q-MC//CC compared to the MC//CC electrode by the incorporation of CNQDs. The calculated specific capacitances of the q-MC//CC electrode are 1001.4, 609.3, 469.8, and 322.6 F g⁻¹ at 1, 2, 3, and 5 A g⁻¹, respectively. The charge storage mechanism of MnCO₃ involves the intercalation/de-intercalation of Na⁺ with the redox reactions of the Mn ions. In addition, a surface process of the adsorption/desorption of Na⁺ ions occurs. The redox process of Mn (II) ↔ Mn (I) occurs in Na₂SO₄ electrolyte: MnCO₃ + Na⁺ + e⁻ ↔ NaMnCO₃. CNQDs on MnCO₃ can facilitate the intercalation/de-intercalation of Na⁺ ions and the redox reaction of Mn ions. This excellent electrochemical performance of the q-MC//CC electrode is highly comparable with previously reported MnCO₃-based electrodes (Table 3-1).

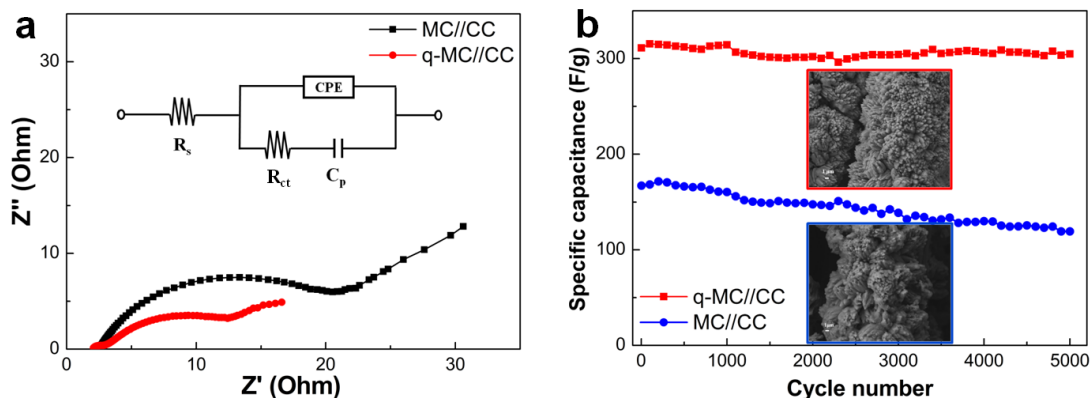


Fig. 3-10 (a) Nyquist plots of q-MC//CC and MC//CC. (a) Specific capacitance retention of q-MC//CC and MC//CC along 5000 cycles (insets show their SEM images after cycle test).

To further investigate the kinetics of ion and charge transfer, an EIS test was performed, and the Nyquist plots of q-MC//CC and MC//CC are presented in Figure 3-10a. The plots consist of a depressed circle at the high-frequency region and a straight line at the low-frequency region. The depressed is attributed to the charge transfer process of the Faradaic reaction at the interface of the electrode and electrolyte, and it belongs to the kinetic control, while the low-frequency region belongs to the mass transfer control. The formation of a depressed circle due to the roughness of the electrode/electrolyte surface results in the change of capacitance in double layer. In addition, the high slope of observed, traight lines at the low-frequency region represents a small Warburg resistance. At the low-frequency region, the linear shape suggests the fast ion diffusion in electrolyte and the adsorption process at the electrode surface. The solution resistances (R_s) of q-MC//CC and MC//CC are 2.1 Ω and 2.5 Ω ; the as-prepared q-MC//CC enhances electron transport from electrode to current collector, implying the decrease in equivalent series resistance by the strong synergistic effect between $MnCO_3$ and CNQDs. The diameter of the depressed circle denotes the charge transfer resistance (R_{ct}). The q-MC//CC electrode exhibits a much lower R_{ct} value (10.8 Ω) than the MC//CC electrode (18.0 Ω), clearly revealing that the highly conductive interface between CNQDs and $MnCO_3$ significantly improves

the charge transfer kinetics. The long-term cycle stability of q-MC//CC and MC//CC electrodes was examined by CV measurement for 5000 cycles at a scan rate of 50 mV s^{-1} . As shown in Figure 3-10b, the q-MC//CC electrode exhibits superior cycle performance with a 96% retention of its initial specific capacitance compared to the MC//CC electrode (71%). These results may be attributed to the distribution of CNQDs on MnCO_3 , which can suppress the deformation and damage of the structure. As shown in the insert images in Figure 3-10b, the q-MC//CC electrode retains its initial microstructure after cycling, while the MC//CC electrode shows a swollen structure, revealing the excellent cycle stability of the q-MC//CC electrode.

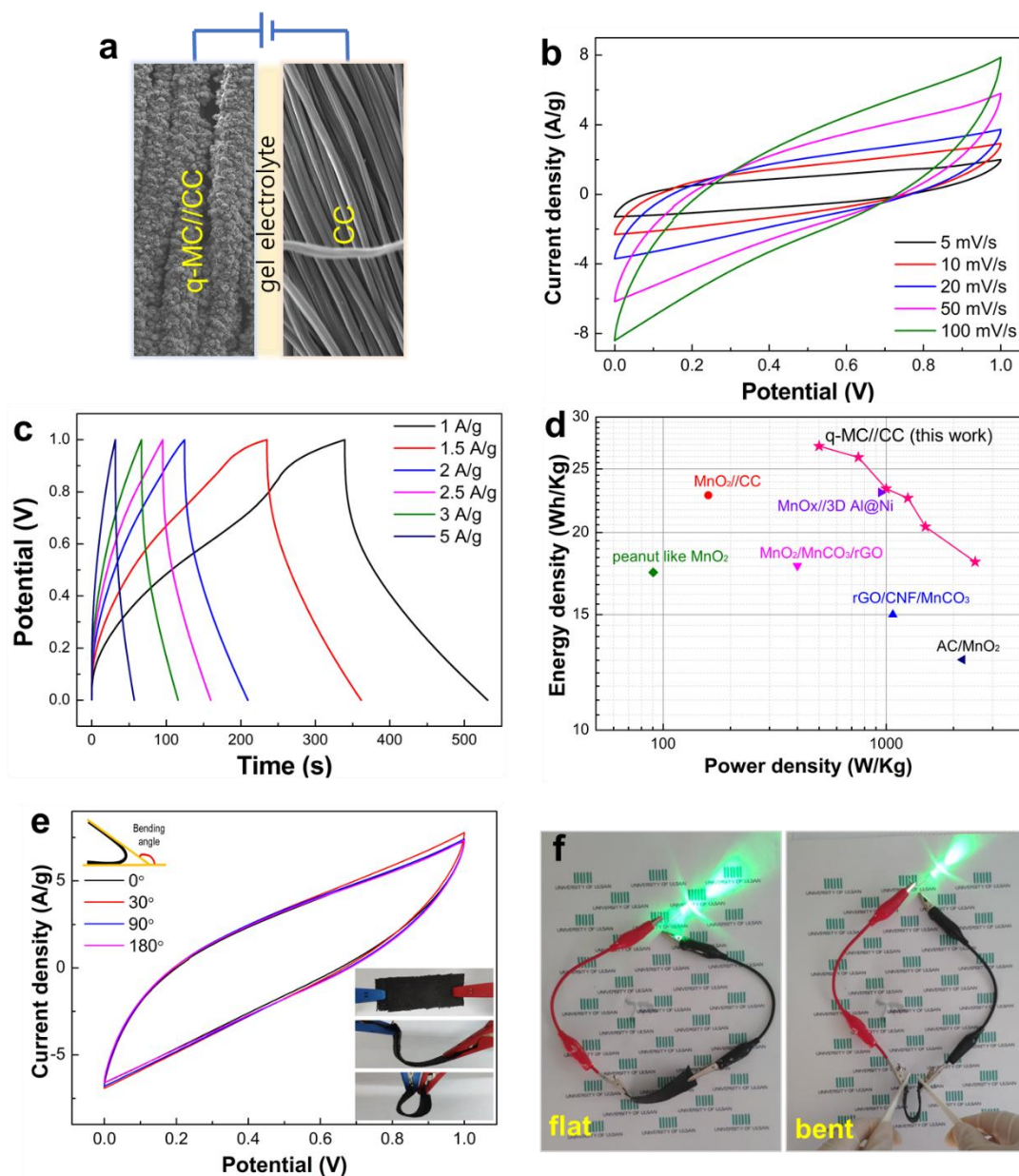


Fig. 3-11 (a) Schematic illustration of all-solid-state ASC using q-MC//CC electrode. (b) CV curves at different scan rates and (c) galvanostatic charge-discharge curves at different current densities of q-MC//CC based ASC. (d) The Ragone plots of q-MC//CC based ASC and reported Mn-based supercapacitors. (e) CV curves of the q-MC//CC based ASC under mechanical bending. (f) Photo image of lighting LED powered by q-MC//CC based ASC under flat and bent state.

To study the practical application of q-MC//CC as a binder-free electrode, an all-solid-state asymmetric supercapacitor (ASC) device was constructed. The q-MC//CC electrode was the positive electrode and a carbon cloth was the negative electrode, which were then assembled with a polyvinyl alcohol (PVA)/Na₂SO₄ gel

electrolyte and separator (Figure 3-11a). The CV curves measured at different scan rates are shown in Figure 3-11b. All CV curves present typical quasi-rectangular shapes without any obvious redox peaks, indicating the ideal capacitive behavior of the prepared ASC with the q-MC//CC electrode. Figure 3-11c presents the GCD curves at different current densities from 1 to 5 A g⁻¹. The nearly symmetric charge–discharge curves imply the high reversibility of the q-MC//CC electrode. The specific capacitances of ASC using the q-MC//CC electrode obtained from the curves are 195, 168, 147, and 130 F g⁻¹ at current densities of 1, 2, 3, and 5 A g⁻¹, respectively. The energy density of the assembled ASC is calculated and compared with other previous Mn-based ASC devices in the Ragone plot, as shown in Figure 6d. The prepared q-MC//CC electrode ASC delivers an energy density of 27.1 Wh kg⁻¹ at a power density of 500 W kg⁻¹ and retains 18.1 Wh kg⁻¹ even at a high power density of 2500 W kg⁻¹, which is superior to other systems reported [22–27]. To explore mechanical stability, the CV curves of the all-solid-state ASC using q-MC//CC are measured under different bending angles at a scan rate of 50 mV s⁻¹. The results in Figure 3-11e reveal that the CV curve shapes are well maintained with no remarkable changes, even at a bending angle of 180°, which reveals the good mechanical good mechanical stability of the a-MC//CC electrode during bending. In addition, the application potential of the assembled ASC is further explored. Figure 3-11f shows that the ASC device under a flat and folded state lights up the green light-emitting diode (LED).

Table 3-1 Comparison of the electrochemical performance of q-MC//CC with previous reports.

Electrode	Electrolyte	Specific capacitance	Cycle stability	Ref.
Electrodeposited MnCO ₃	0.1M Na ₂ SO ₄	194F/g at 0.5A/g	92% after 10000 cycles	[28]

MnCO ₃ @rGO O	KI/0.5M Na ₂ SO ₄	546F/g at 0.5A/g	103% after 2000 cycles	[29]
MnCO ₃ /rGO	1M Na ₂ SO ₄	335F/g at 2A/g	73% after 10000 cycles	[30]
rGO/CNF/MnCO ₃	1M Na ₂ SO ₄	215 F/g at 0.2A/g	91% after 500 cycles	[25]
MnCO ₃ microphere @MnO ₂	1M Na ₂ SO ₄	363 F/g at 1A/g	84% after 2000 cycles	[31]
rGO/MnCO ₃	1M Na ₂ SO ₄	368 F/g at 1.5A/g	96% after 1000 cycles	[11]
Peanut-like MnCO ₃	2M KOH	293.7F/g at 0.25 A/g	72% after 6000 cycles	[22]
Ni-doped	3M KOH	583.5F/g at	85%	[27]

MnCO ₃		1A/g	after 2000 cycles	
CNT/MnO ₂ nanosheets	1M Na ₂ SO ₄	1229 F/g at 1A/g	94% after 10000 cycles	[32]
g-C ₃ N ₄ QDs/MnCO ₃ //CC	1M Na ₂ SO ₄	1001 F/g at 1A/g	96% after 5000 cycles	This work

3.6 Conclusions

In summary, q-MC//CC for a binder-free electrode of supercapacitor was successfully prepared via a simple hydrothermal method. The synergistic effects of CNQDs embedded on MnCO₃ can improve the interface electrical conductivity and shorten the ion diffusion paths for the utilization of MnCO₃. The binder-free q-MC//CC electrode shows enhanced supercapacitive performance, including a high specific capacitance of 1001.4 F g⁻¹ at a current density 1 A g⁻¹ and a superior cycling performance of 96% retention after 5000 cycles. In addition, the q-MC//CC electrode-based ASC was assembled with a gel electrolyte, which exhibited a high energy density of 27.1 Wh kg⁻¹ with a power density of 500 W kg⁻¹ with good mechanical stability. These results provide a promising alternative method to prepare a binder-free electrode for high-performance flexible supercapacitors.

3.7 References

- [1] Wang, G.; Zhang, L.; Zhang, J. *Chem. Soc. Rev.* 2012, 41, 797–828.
- [2] He, S.; Hu, C.; Hou, H.; Chen, W. *J. Power Sources* 2014, 246, 754–761.
- [3] Gomez, J.; Kalu, E.E. *J. Power Sources* 2013, 230, 218–224.
- [4] Wu, Y.; Liu, S.; Wang, H.; Wang, H.; Zhang, X.; Jin, G. *Electrochim. Acta* 2013, 90, 210–218.
- [5] Devaraj, S.; Liu, H.Y.; Balaya, P. *J. Mater. Chem. A* 2014, 2, 4276–4281.
- [6] Wang, L.; Sun, Y.; Zeng, S.; Cui, C.; Li, H.; Xu, H.; Wang, H. *CrystEngComm* 2016, 18, 8072–8079.
- [7] Vardhan, P.V.; Sridhar, S.; Sivakkumar, S.R.; Mudali, U.K.; Devaraj, S. *J. Nanosci. Nanotechnol.* 2018, 18, 2775–2780.
- [8] Wang, R.; Ma, Y.; Wang, H.; Key, J.; Brett, D.; Ji, S.; Shibin, Y.; Shen, P.K. *J. Mater. Chem. A* 2016, 4, 5390–5394.
- [9] Wen, Q.; Zhang, S.; Sun, M.; Jin, R. *Nano* 2018, 13, 1850050.
- [10] Wu, S.; Liu, C.; Dinh, D.A.; Hui, K.S.; Hui, K.N.; Yun, J.M.; Kim, K.H. *ACS Sustain. Chem. Eng.* 2019, 7, 9763–9770.
- [11] Ghosh, D.; Giri, S.; Dhibar, S.; Kumar, C. *Electrochim. Acta* 2014, 147, 557–564.
- [12] Yuan, J.; Zhu, J.; Bi, H.; Zhang, Z.; Chen, S.; Liang, S.; Wang, X. *RSC Adv.* 2013, 3, 4400–4407.
- [13] Zhou, L.; Kong, X.; Gao, M.; Lian, F.; Li, B.; Zhou, Z.; Cao, H. *Inorg. Chem.* 2014, 53, 9228–9234.
- [14] Zhong, Y.; Yang, M.; Zhou, X.; Luo, Y.; Wei, J.; Zhou, Z. *Adv. Mater.* 2015, 27, 806–812.
- [15] Chang, X.; Zhai, X.; Sun, S.; Gu, D.; Dong, L.; Yin, Y.; Zhu, Y. *Nanotechnology* 2017, 28, 135705.
- [16] Shi, Y.; Gao, S.; Yuan, Y.; Liu, G.; Jin, R.; Wang, Q.; Lu, J. *Nano Energy* 2020, 77, 105153.
- [17] Dong, B.; Li, M.; Chen, S.; Ding, D.; Wei, W.; Gao, G.; Ding, S. *ACS Appl. Mater. Interfaces* 2017, 9, 17890–17896.
- [18] Lee, S.H.; Kwon, Y.; Park, S.; Cho, M.; Lee, Y. *J. Mater. Sci.* 2015, 50,

5952–5959.

- [19] Zhang, R.; Wang, D.; Qin, L.C.; Wen, G.; Pan, H.; Zhang, Y.; Huang, X. *J. Mater. Chem. A* 2017, 5, 17001–17011.
- [20] Chandra Sekhar, S.; Nagaraju, G.; Yu, J.S. *Appl. Surf. Sci.* 2018, 435, 398–405.
- [21] Chen, J.J.; Mao, Z.Y.; Zhang, L.X.; Wang, D.J.; Xu, R.; Bie, L.J.; Fahlman, B.D. *ACS Nano* 2017, 11, 12650–12657.
- [22] Tang, Y.; Chen, S.; Chen, T.; Guo, W.; Li, Y.; Mu, S.; Yu, S.; Zhao, Y.; Wen, F.; Gao, F. *J. Mater. Chem. A* 2017, 5, 3923–3931.
- [23] Zhang, H.; Lin, L.; Wu, B.; Hu, N. *J. Power Sources* 2020, 476, 228527.
- [24] Wang, H.; Fu, Q.; Pan, C. *Electrochim. Acta* 2019, 312, 11–21.
- [25] Amutha, B.; Sathish, M. *J. Solid State Electrochem.* 2015, 19, 2311–2320.
- [26] Karuppaiah, M.; Akilan, R.; Sakthivel, P.; Asaithambi, S.; Shankar, R.; Yuvakkumar, R.; Hayakawa, Y.; Ravi, G. *J. Energy Storage* 2020, 27, 101138.
- [27] Zhao, N.; Fan, H.; Zhang, M.; Ren, X.; Wang, C.; Peng, H.; Li, H.; Jiang, X.; Cao, X. *Ceram. Int.* 2019, 45, 5266–5275.
- [28] Vardhan, P.V.; Idris, M.B.; Ramanathan, V.; Devaraj, S. *Chemistryselect* 2018, 3, 6775–6778.
- [29] Li, H.; Wu, X.; Zhou, J.; Liu, Y.; Huang, M.; Xing, W.; Yan, Z.; Zhuo, S. *ChemElectroChem* 2019, 6, 316–319.
- [30] Jana, M.; Samanta, P.; Chandra Murmu, N.; Kuila, T. *J. Mater. Chem. A* 2017, 5, 12863–12872.
- [31] Chen, H.; Yan, Z.; Liu, X. Y.; Guo, X. L.; Zhang, Y. X.; Liu, Z. H. *J. Power Sources* 2017, 353, 202–209.
- [32] Jia, H.; Cai, Y.; Zheng, X.; Lin, J.; Liang, H.; Qi, J.; Cao, J.; Feng, J.; Fei, W. *ACS Appl. Mater. Interfaces* 2018, 10, 38963–38969.

CHAPTER 4 Synergistically enhanced activity of C₃N₄ quantum dots /graphene hydrogel composites for symmetric supercapacitors

4.1 Introduction

In recent years, energy storage has become a key technology due to the deteriorating energy consuming and global warming. Supercapacitors, as one of remarkable energy storage devices, have recently received great attention for powering electronics because of their high power capability, long cycling life and low maintenance cost [1-2]. The electrode is the vital part of a supercapacitor, and there're various active materials for electrode, such as transition metal compound, conducting polymers and carbon materials [3-7].

Among carbon materials, graphene as a two-dimensional monolayer of sp²-hybridized carbon atom has received sustained attention due to its unique electrical, mechanical, and thermal properties [8-10]. Assembly of graphene sheets into three-dimensional macroscopic materials as graphene hydrogel (GH) can have high performance as electrode materials, because of their high porosity, large specific surface area and high electrical conductivity [11-13]. Recently, a great deal of efforts by introducing some heteroatoms or quantum dots into GH has shown a promising way to increase the capacitive performance of electrode, such as nitrogen doped [14-16], sulphur doped [17], fluorinated [18], carbon dots [19], graphene quantum dots (GQD) doped [20] and nitrogen-GQD doped [21]. For example, He's group [16] synthesized nitrogen doped GH shows excellent capacitive behavior, they indicated that excellent electrochemical behavior attributed to the incorporation of the pyrrolic and pyridinic N in the graphene, which enhanced the pseudo-capacitance. Li's group [21] fabricated N-GQDs doped GH on carbon fibers (CF) improved electrochemical performance, which capacitance was around 7 times higher than that of GH/CF. These reports showed the important role of pyrrolic and pyridinic N exist in graphene is favorable for improving the pseudo-capacitance.

However, graphitic carbon nitride (g-C₃N₄) as a nitrogen-rich substance already attracted increasing attention for enhancing electrochemical activity for the electrode materials[22-28].Chen et al.[28] have prepared graphene/g-C₃N₄ composites via a hydrothermal reaction.16 It is found that the composites show a high specific capacitance of 264 F g⁻¹ in acid electrolyte medium as well as outstanding cycling stability which retains over 80% of its initial capacitance after 10000 charge–discharge cycles. Mohammadi et al. [25] declared that g-C₃N₄ was a new doorway to facilitate the next generation of carbon-based supercapacitors, it possess a plentiful attractive properties, including particular chemical and thermal stability, nitrogen rich framework, environmentally friendly characteristics and mild synthesis conditions. It also reported that high nitrogen content in g- C₃N₄ can provide active sites for faradic reactions, which could increase the surface polarity, improve the wettability of electrode and consequently, enhance the mass transfer efficiency. What’s more, the well-developed nanostructures with high surface area could undoubtedly favor of achieving more abundant active sites and better mass transfer over g-C₃N₄. However, there’s scarcely any report about g-C₃N₄ quantum dots (QDs) for electrode materials except our previous work [29].

Herein, we report a facile approach to assemble g-C₃N₄ QDs doped graphene hydrogel nanomaterials by dispersion g-C₃N₄ QDs in graphene oxide (GO) precursor solution, the hybrid hydrogel with hierarchical and interconnected structure are obtained through a typical self-assembly process during the reduction of GO by a hydrothermal reaction. We found that the incorporation of g-C₃N₄ QDs into the porous GH network can markedly promote ion diffusion/transport capability at the electrode/electrolyte interface and enhance the Faradic reaction and electron transfer, leading to the observed increase in the capacitance. We also investigated the effect of g-C₃N₄ QDs doping content on GH for electrochemical performance. We obtained the 2.5 wt% content of g-C₃N₄ QDs on GH own optimal electrochemical performance on electrode, it was able to deliver a specific capacitance of 385.8 F g⁻¹ at 5 mV s⁻¹ , which was around 4.1 times higher than that of GH electrode (93.2 F g⁻¹). The assembled symmetric g-C₃N₄ QDs-GH exhibited a high energy density of 22.5 Wh kg⁻¹ at a power density of 250 W kg⁻¹ and the symmetric device also exhibited

excellent flexibility and cycling stability.

4.2 Experimental

Materials: GO powders, melamine, $\text{NH}_3 \cdot \text{H}_2\text{O}$, H_2SO_4 and HNO_3 . Deionized water was used for all experiments. All the chemical reagents with reagent grade were used in the experiments without further purification.

4.2.1 Preparation of g- C_3N_4 quantum dots

Firstly, 5g Melamine was calcinated in muffle at 550°C for 4h to get bulk- C_3N_4 . Then, 2 g of bulk g- C_3N_4 was treated in the mixture of concentrated sulfuric acid (40 mL) and nitric acid (40 mL) for about 2 h at room temperature. The mixture was then diluted with deionized water (1 L) and washed for several times, the as-obtained white product was porous g- C_3N_4 . Second, 444 mg of the porous g- C_3N_4 was dispersed in 134 mL concentrated $\text{NH}_3 \cdot \text{H}_2\text{O}$, and then the mixed suspension was transferred into a 200 mL Teflon cup and heated in a sealed autoclave at 180°C for 12 h, during which the porous g- C_3N_4 will be peeled into porous nanosheets. Upon cooling to room temperature, the precipitate was washed with water for several times to remove the adsorbed NH_3 molecules. Third, 10 mg of porous g- C_3N_4 nanosheets was dispersed in 100 mL water, and then ultrasound for about 6 h. The as-obtained aqueous suspension was then centrifuged at about 7000 rpm, and dialyzed in a dialysis bag to remove large-sized nanoparticles.

4.2.2 Preparation of GH and GH-CN composites

GH was obtained by some modifications in the processdure from the literature described by Xu etal [11]. 125ml homogeneous GO aqueous solution at concentrations of 2.5 mg/ml was added to a 200ml Teflon-lined autoclave and maintained at 180°C for 12h. After the hydrothermal process, the autoclave was cooled to room temperature. GH was brought out by a tweezer and dried by freeze-drying method.

For GH-CN composites synthesis, a certain amount (125ml) of GO and g- C_3N_4 quantum dots mixed solution (2.5mg/ml) with different weight ratio (CN/ (CN+GO) =

0 wt%, 1 wt%, 2.5 wt% and 5 wt%) were added to the autoclave, the processdure was same as the GH preparation. The composites were named as GH, GH-1CN, GH-2.5CN and GH-5CN respectively.

4.3 Characterization

Scanning electron microscopy (SEM) images and Energy dispersive spectrometry (EDS) mapping images were taken on a JEOL FESEM-JSM820, and transmission electron microscope (TEM) images and high-resolution transmission electron microscopy (HRTEM) images were obtained using a Hiachi H-8100 TEM instrument. X-ray diffraction (XRD) measurement was performed using a Bruker D8 Advance diffractometer with a non-monochromated Cu K α operated at 40 kV and 30 mA. Fourier transform infrared (FTIR) spectra were obtained using a Nicolet IR 200 FT-IR spectrometer (Thermo Scientific). X-ray photoelectron spectroscopy (XPS: Thermo Fisher) measurements were performed using monochromatic AlK α radiation ($h\nu = 1486.6$ eV).

4.4 Electrochemical measurement

Electrochemical performance was investigated by cyclic voltammetry (CV), galvanostatic charge/discharge (GCD), and electrochemical impedance spectroscopy (EIS) tests. All electrochemical measurements were performed using a BioLogic VSP electrochemical workstation at room temperature. A three-electrode system was used to test the electrochemical performance of the prepared electrodes with platinum wire and Ag/AgCl electrodes as the counter and reference electrodes, respectively. The working electrode for the testing supercapacitor was prepared by mixing active materials, acetylene black and polyvinylidene fluoride (PVDF) in N-methyl-2-pyrrolidone (NMP) at a mass ratio of 80:10:10. The as-prepared slurry was coated onto the surface of the glass carbon electrode (5mm in diameter), with an average mass loading of ~ 0.5 mg/cm². The electrode was dried at 40°C for 1h in an oven. All electrochemical tests were performed in an aqueous electrolyte of 6 M KOH at room temperature. EIS was performed at open circuit potential in a frequency range

from 10 kHz to 0.01 Hz with an AC amplitude of 5 mV.

Fabrication of symmetric supercapacitor (SSC): At first, Ni foam was pressed using a 1 ton weight to form a flexible Ni sheet, which was then washed several times with acetone and ethanol. This Ni sheet was used as a working electrode as well as a current collector. The capacitive performance of GH-2.5CN composite was investigated using a two-electrode testing device. The working electrodes for tests were prepared by mixing active materials, acetylene black and polyvinylidene fluoride (PVDF) in N-methyl-2-pyrrolidone (NMP) at a mass ratio of 80:10:10 to form the homogeneous slurry. The slurry was pressed onto the nickel sheet and dried at 70°C for 12 h. Then, two electrodes with identical or very close weight were separated by a polytetrafluoroethylene membrane separator and assembled with PVA/KOH gel electrolyte. The as-fabricated SSC device was named as GH-CN//GH-CN.

The specific capacitance (C_s) of the product can be calculated from the CV curves and galvanostatic charge-discharge curves according to the following equation:

$$C_s = \frac{\int I(V) dV}{v \times m \times \Delta V} \quad (1)$$

$$C_s = \frac{I \times \Delta t}{m \times \Delta V} \quad (2)$$

where $\int I(V) dV$ is the area enclosed by the CV curves, ΔV (V) is the potential window, v (mV s^{-1}) is the potential scan rate, m (g) is the mass of the active materials in the electrodes, and Δt (s) is the discharge time.

The energy density E (Wh kg^{-1}) and power density P (W kg^{-1}) of the device were calculated using the following equations:

$$E = \frac{C_s \times (\Delta V)^2}{2 \times 3.6} \quad (3)$$

$$P = \frac{3600 \times E}{\Delta t} \quad (4)$$

4.5 Results and discussion

The process for the synthesis of g-C₃N₄ QDs embedded in graphene hydrogel composites by hydrothermal method is illustrated in Fig.4-1. The g-C₃N₄ QDs was added to the GO homogeneous solution which after ultrasonic for 2 hours, thus the

quantum dots can be embedded into the sheet while the formation of graphene hydrogel during the hydrothermal process. As shown in Fig.4-1, the graphene hydrogel still can keep cylindrical though g-C₃N₄ QDs was added. Finally, the GH-CN composites electrodes were used to fabricate the symmetric supercapacitor for powering a light-emitting diode (LED).

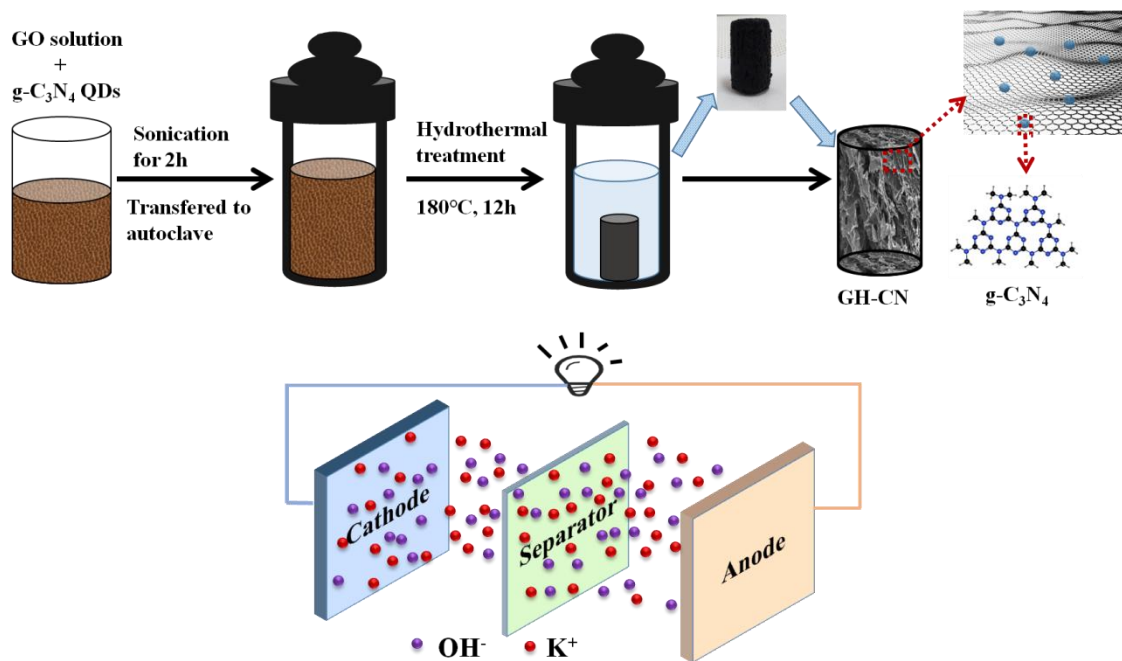


Fig. 4-1 Synthesis of GH-CN composites as the electrode materials for symmetric supercapacitor.

The phases and chemical features of all prepared samples were measured by XRD and FTIR analysis. In Fig.4-2a, all samples showed two obvious broad peaks at about 25 ° and 43 °; which can be assigned to the (002) and (100) planes of the carbon phase respectively. Meanwhile, the broad peaks suggest the poor aligned structure of graphene sheet along their stacking direction and reflects the framework is composed of layer stacked graphene sheets [11]. And the intensity of peaks of GH-CN decreased with compared to GH, which attributed to the adding of g-C₃N₄ QDs, the quantum dots embedded into the graphene hydrogel maybe has a little effect on the aligned structure of graphene sheet. Moreover, Fig.4-2b presents FTIR spectra of the as-prepared samples and all the samples showed peaks at 1217 cm⁻¹, 1400 cm⁻¹, 1720 cm⁻¹ and 2250 cm⁻¹ which were ascribed to the stretching vibration of C-C, C-O-H, C=O and

C=C respectively. However, the intensity of C=C peak decreased after adding of g-C₃N₄ QDs, which is also agreement with the XRD results. What's more, the GH-CN composites showed a obvious new peak at 1580 cm⁻¹, which is correspond to the typical stretching vibration of C=N band, this results indicates the g-C₃N₄ QDs were well embedded into the graphene hydrogel, and this conclusion will be further proven by XPS results in Fig.4-7.

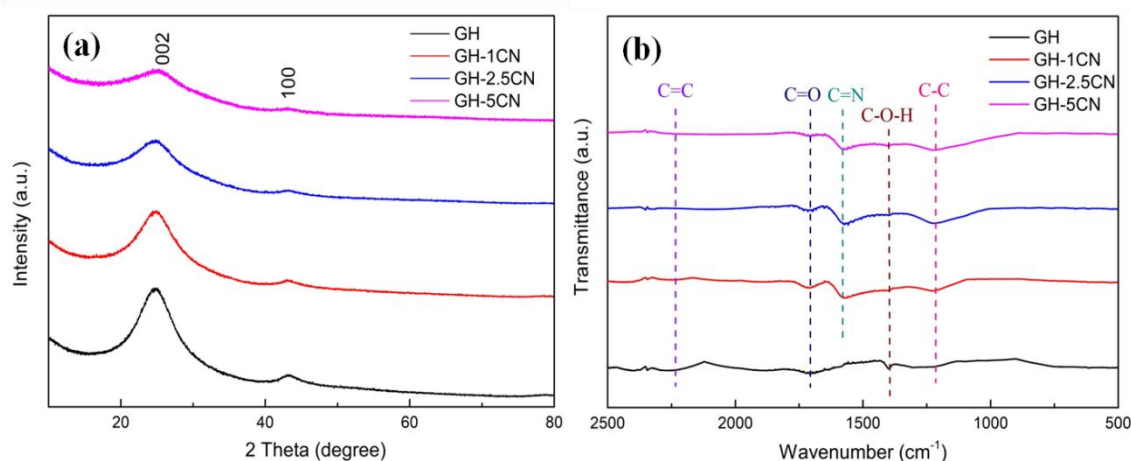


Fig. 4-2 (a) XRD results and (b) FTIR patterns of GH and GH-CN composites.

Fig.4-3 presents the FE-SEM images of GH and GH-2.5CN samples, the elemental mapping and EDS measurement are also tested for GH-2.5CN sample. The typical SEM image of GH is shown in Fig.4-3a and Fig.4-4, the SEM image shows that GH has a well-defined and interconnected 3D porous network and layer-stack structure. Fig.4-3b and 4-3c shows the SEM image of the GH-2.5CN sample, it also shows similar morphology with GH, 3D network structure, composed of a large amount of interconnected pores. In the Fig.4-3c, it's clearly that the walls of these pores consisting of thin layers of stacked graphene nanosheets. The EDS elemental maps of Fig.4-3d are shown in Fig.4-3 e-g, and the results indicated that carbon, oxygen and nitrogen were uniformly distributed in the GH-2.5CN composite. To further validate the composition, the sample was invitigated by EDS as shown in Fig.4-3h, where the carbon, oxygen and nitrogen were detected, this result is in conjunction with the SEM observations above. Therefore, the elemental distribution of Fig.4-3d is shown in Fig.4-3i, the weight percent of carbon, nitrogen and oxygen is

about 77.0%, 2.4% and 20.6% respectively. These results confirming that the g-C₃N₄ QDs are successfully assembled into GH networks.

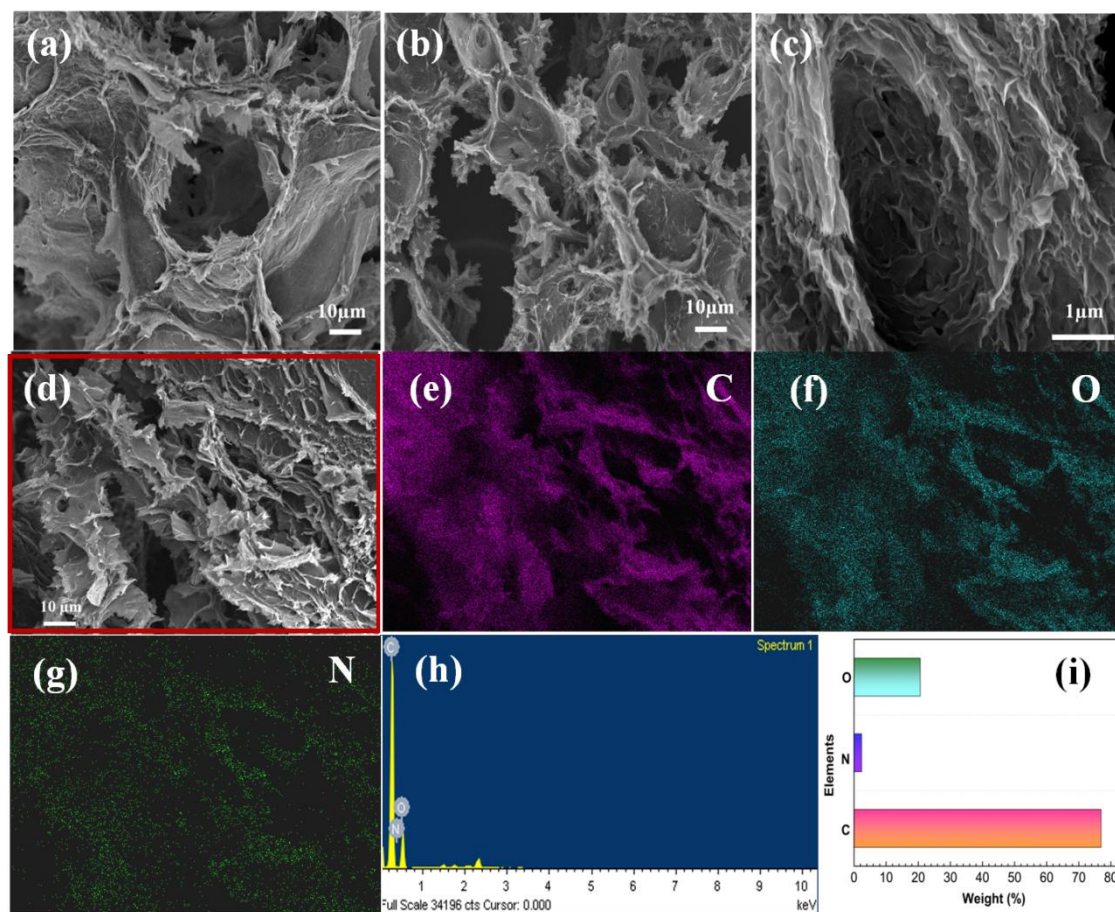


Fig. 4-3 (a) SEM images of GH; (b,c) GH-2.5CN composites; (d-g) SEM image and elemental mapping for GH-2.5CN composites; (h,i) EDS measurement of the plotted area and the elemental distribution of GH-2.5CN composites.

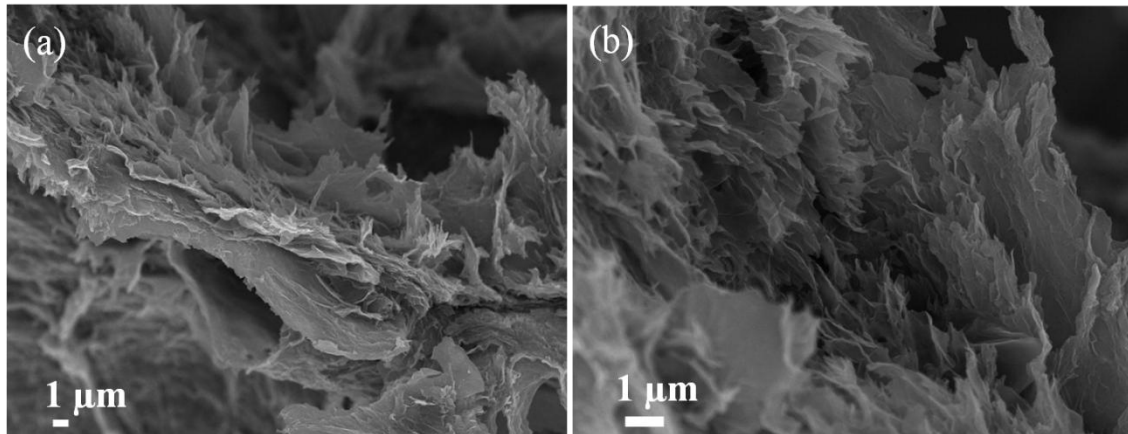


Fig. 4-4 SEM images of GH

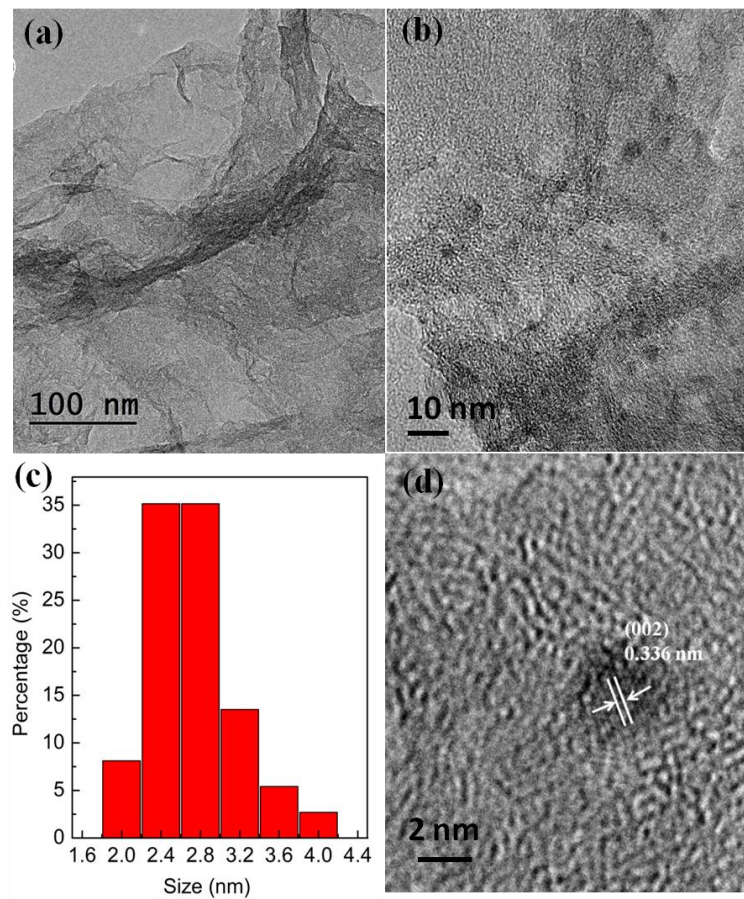


Fig. 4-5 (a)TEM iamge of the GH nanostructure; (b) TEM image of GH-2.5CN ; (c) the size distribution of g-C₃N₄ QDs on graphene hydrogel from (b); (d) HRTEM image of GH-2.5CN.

The morphology and structure of GH and GH-2.5CN were further examined by TEM analyse, as shown in Fig.4-5. From Fig.4-5a, the prepared GH show ultrathin nanosheets with some wrinkles, suggesting that 3D framework could be composed of the grapheme sheets. Fig.4-5b-d and Fig.4-6 show the TEM of GH-2.5CN, it can be directly observed that some dark dots distributed in the grapheme sheet, this clearly state the tight hybridization of g-C₃N₄ QDs with ultrathin graphene nanosheets for GH-2.5CN sample. In Fig.4-5b, the g-C₃N₄ QDs show spherical morphology, and mainly distribute in 2-4 nm with the average lateral size of about 2.8 nm. The HRTEM image of GH-2.5CN as shown in Fig.4-5d further reveals the presence of g-C₃N₄ QDs, and the dark dot has an obvious lattice fringes of 0.336 nm, which is in coincidence with the (002) facet of graphitic carbon nitride [30]. The TEM results further confirmed that GH-CN products were successfully synthesized.

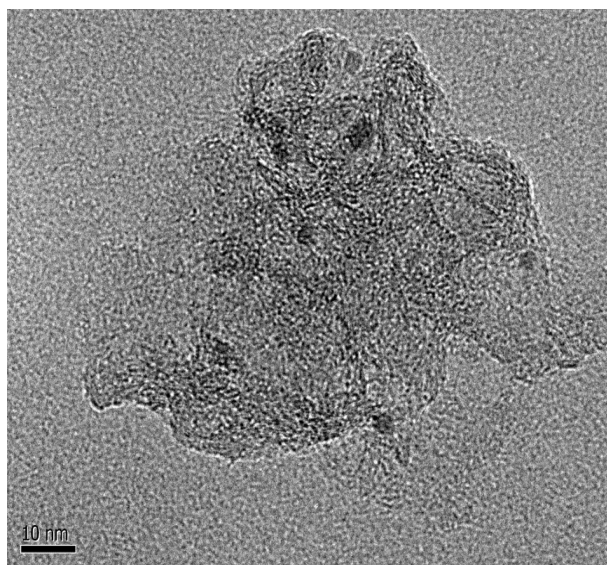


Fig. 4-6 TEM images of GH-2.5CN

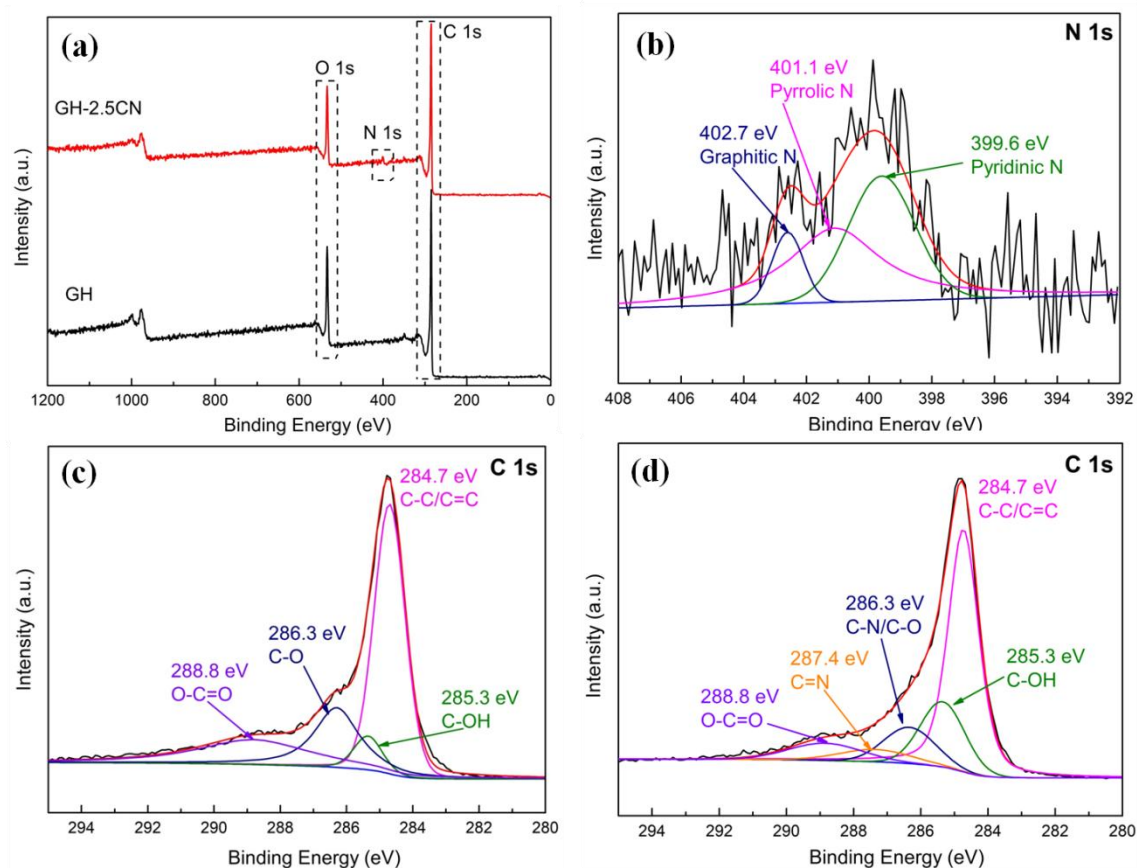


Fig. 4-7 (a) XPS survey spectra of GH and GH-2.5CN samples; (b) N 1s of GH-2.5CN; (c) C 1s of GH; (d) C 1s of GH-2.5CN.

The corresponding XPS profiles of GH and GH-2.5CN are displayed in Fig.4-7, indicating the chemical bond on the samples. The full survey spectrums of GH and GH-2.5CN are shown in Fig.4-7a, two elements of C and O are detected in the GH while three elements of C, N and O are detected in the GH-2.5CN, indicating the g-C₃N₄ QDs are successfully introduced to graphene hydrogel. To get detailed chemical states information, the high-resolution XPS spectra of N1s and C1s were recorded. For N1s of GH-2.5CN, as illustrated in Fig.4-7b, there're three peaks locate at the binding energies of 399.6 eV, 401.1 eV and 402.7 eV, which can be ascribed to pyridinic N, pyrrolic N and graphitic N, respectively. In these three nitrogen bonding configurations, pyrrolic N is in sp³-hybridized state and pyridinic N is in sp²-hybridized state, they are both negative charge. However, graphitic N is positive charge and in the sp²-hybridized state. Therefore, pyrrolic N and pyridinic N can generate pseudocapacitance via Faraday reactions, while graphitic N can enhance the conductivity of graphene materials through the positive charge and its repair effect on

graphene sheets. Fig.4-7c and Fig.4-7d show the C1s spectra for GH and GH-2.5CN respectively. In Fig.4-7c, the C1s spectrum can be de-convoluted into four peaks at 284.7 eV, 285.3 eV, 286.3 eV and 288.8 eV, which are assigned to C-C/C=C in graphene plane, C-OH, C-O and O-C=O bonds, respectively [31]. Compared with GH, the binding energies at 286.3 eV and 287.4 eV of GH-2.5CN are assigned to C-N/C-O and C=N bonds. These results can further demonstrate the successful incorporation of g-C₃N₄ QDs with graphene hydrogel.

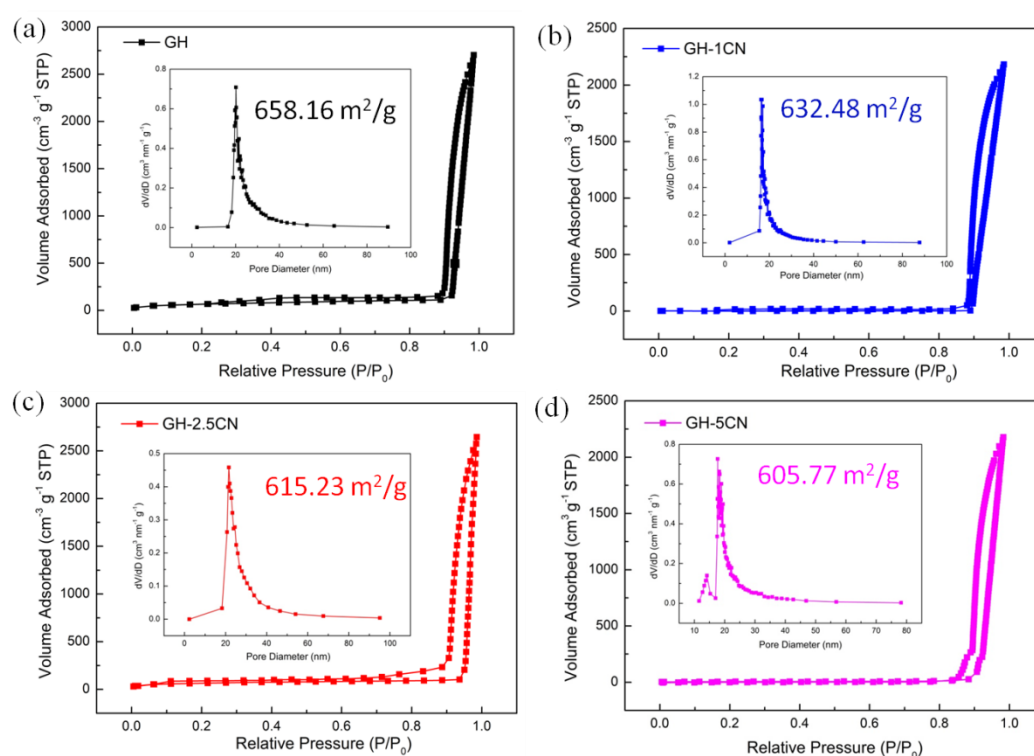


Fig.4-8 Nitrogen adsorption-desorption isotherms and pore size distribution plots of GH (a), GH-1CN (b), GH-2.5CN (c) and GH-5CN (d).

The porous structure of GH and GH-CN composites were confirmed by the nitrogen adsorption and desorption measurements. Brunauer–Emmett–Teller (BET) and Barrett–Joyner–Halenda (BJH) analysis reveal that the freeze-dried GH has a high specific surface area of $\approx 658.16 \text{ m}^2 \text{ g}^{-1}$ the pore sizes in the range of 2–100 nm (Figure 4-8a). It should be noted that the BET measurement of the freeze-dried GH could substantially underestimate the specific surface area of GH because of partial re-stacking of some graphene layers and the fusing of mesopores within GH during

the freeze-drying process, with compare with the theoretical surface area of single-layer graphene ($\approx 2630 \text{ m}^2 \text{ g}^{-1}$). This isotherm curves belongs to the Type II isotherm and reflect the typical physical adsorption process on mesoporous and macroporous adsorbents, due to the interaction of the adsorbate on the surface, the adsorption capacity rises slowly at a lower relative pressure. The inflection point of the isotherm usually appears near the single-layer adsorption. As the relative pressure continues to increase, the multilayer adsorption gradually forms. When the saturated vapor pressure is reached, there are infinite adsorption layers. The amount of adsorbed gas increases as the component partial pressure increases, because the interaction between the adsorbate molecules is stronger than that between the adsorbate and the adsorbent, the adsorption heat of the first layer is smaller than the heat of liquefaction of the adsorbate, so that the adsorbate is more difficult to adsorb at the initial stage of adsorption, and as the adsorption process proceeds, the adsorption self-acceleration occurs, and the number of adsorption layers is not limited. It's obviously that the surface area decreased while the addition of g-C₃N₄ QDs, because some quantum dots block up some pores and affect the amount of adsorbed gas, the surface area were $632.48 \text{ m}^2 \text{ g}^{-1}$, $615.23 \text{ m}^2 \text{ g}^{-1}$ and $605.77 \text{ m}^2 \text{ g}^{-1}$ of GH-1CN, GH-2.5CN and GH-5CN, respectively. From the isothermal curves, this belongs to the H3 type hysteresis loop, H3 type hysteresis loop is mainly found in aggregates of layered structures, it often occurs in mesoporous and macroporous mixed materials. Also, after the addition of g-C₃N₄ quantum dots, the shape of hysteresis loop has a little change, because of the mainly pore shape of GH is like cylindrical-shape, and the quantum dots has some slits-shape pores, so the GH-CN composites have a little change of the hysteresis loop shapes, as it's the mixture of cylindrical-shape and slits-shape pores.

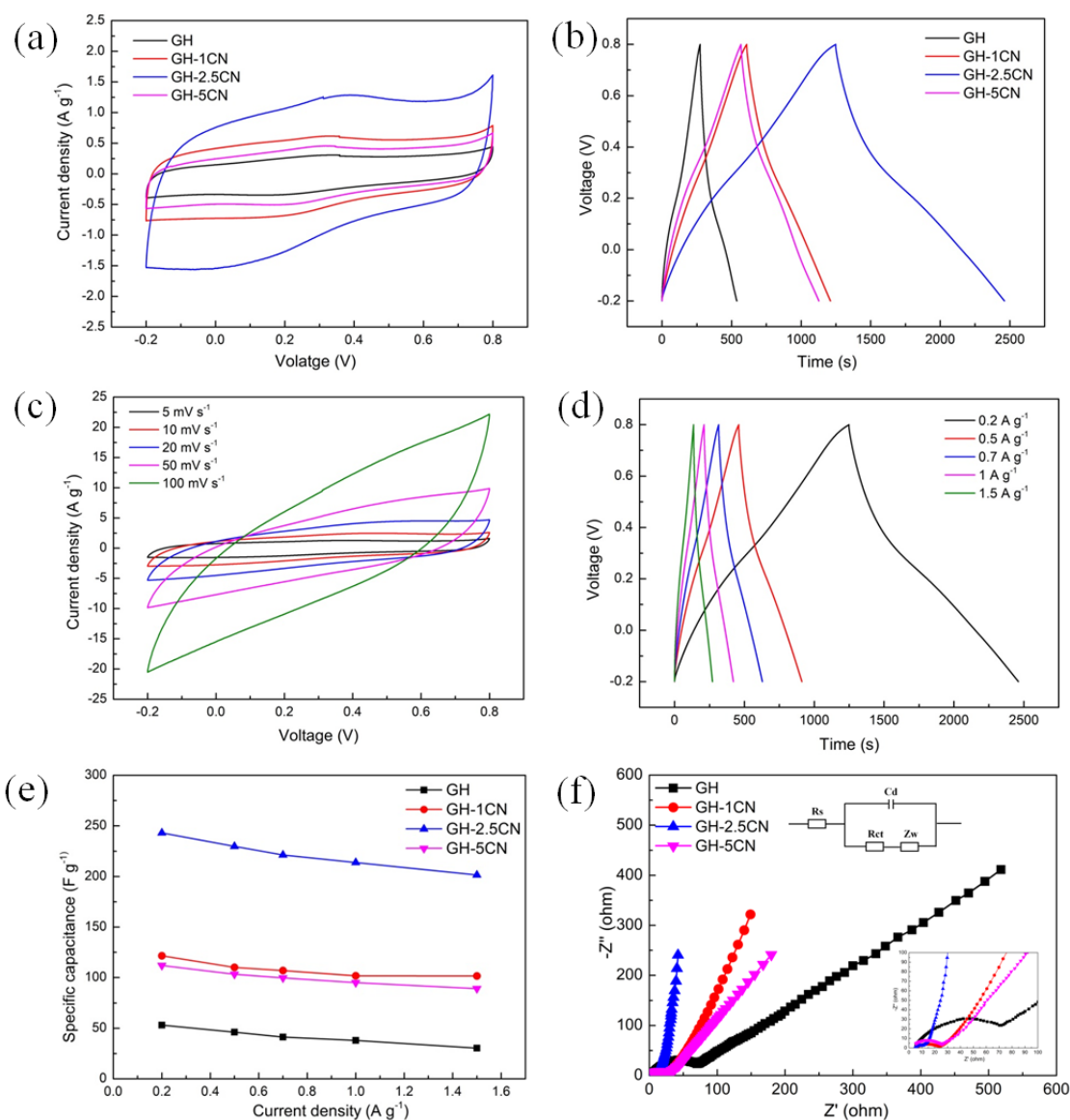


Fig. 4-9 Electrochemical performance of GH, GH-1CN, GH-2.5CN and GH-5CN electrodes in 6M KOH electrolyte using a three-electrode system. (a) Cyclic voltammograms of different electrodes at a scan rate of 5 mV s^{-1} ; (b) Galvanostatic charge-discharge curves of different electrodes at 0.2 A g^{-1} ; (c) CV curves of GH-2.5CN at different scan rates from 5 to 100 mV s^{-1} ; (d) GCD curves of GH-2.5CN at different current density from 0.2 to 1.5 A g^{-1} ; (e) The specific capacitance at different current densities of all samples; (f) Electrochemical impedance spectroscopy (EIS) of the different electrodes (insert: the EIS in the region of high frequency).

The capacitive behaviors of electrode materials were first evaluated by standard three-electrode system in 6M KOH aqueous electrolyte. Fig.4-9 shows the

electrochemical performance of the GH-based electrodes. By comparing the CV curves of GH, GH-1CN, GH-2.5CN and GH-5CN electrodes at a scan rate of 5 mV s^{-1} within potential range from -0.2 to 0.8 V (Fig.4-9a), we can clearly see the CV curves are almost rectangular-shaped. This indicates that the GH and GH-CN composites have an ideal supercapacitive behavior. Apparently, the area of the CV curve for the GH-2.5CN is obviously larger than that of others, indicating higher specific capacitance and synergistic effects. From equation (1), the specific capacitance of all samples at different scan rates were calculated as shown in Table.4-1, the capacitance of GH, GH-1CN, GH-2.5CN and GH-5CN at 5 mV s^{-1} were 93.2, 198.9, 385.8 and 140.8 F g^{-1} , respectively. The capacitance of GH-2.5CN is 4.1 times of GH. The investigation of different scan rate and different density on GH electrode is shown in Fig.4-9. The GCD curves of the GH and GH-CN composites at a current density of 0.2 A g^{-1} are shown in Fig.4-9b. The specific capacitances can be calculated according to equation (2) of those curves from GH to GH-5CN, the corresponding values are about 53.1, 121.6, 243.2 and 112.1 F g^{-1} , respectively. The specific capacitance seems to rise with the increase of g-C₃N₄ QDs content from 0 to 2.5 wt%, however, the capacitance gradually decreased with a further increase to 5 wt%. The hybrid sample presents a highest specific capacitance of 243.2 F g^{-1} with 2.5 wt% g-C₃N₄ QDs, which is 4.6 times higher than those of the pure GH (53.1 F g^{-1}). The investigation of different scan rate on GH-2.5CN electrode is shown in Fig.4-9c, at low scan rate ($\leq 50\text{ mV s}^{-1}$), the CV curves retain a similar rectangular shape without obvious redox peaks as the potential scan rates increased, indicating that the supercapacitor is charged and discharged at a pseudo constant rate. The rectangular shapes suggest the pseudocapacitance feature of the typical GH-CN hybrid hydrogel. However, with the scan rate increasing to 100 mV s^{-1} the CV curve was deviated from rectangularity shape to spindle shape because of the high scan rate. The specific capacitance of all samples also decreased with rising the potential scan rate (as shown in Table.4-1), because at high scan rates, K^+ ions can easily reach to the deep pores of the electrodes at low scan rates, which also contributes to higher specific capacitance. In Fig.4-8d and e, the specific capacitance of the samples gradually declines as the current density increased from 0.2 to 1.5 A g^{-1} . The specific capacitance of GH-2.5CN remained 82.9%

(from 243.2 F g^{-1} to 201.6 F g^{-1}) with increasing the current density from 0.2 to 1.5 A g^{-1} , however, GH sample only kept about 57.2% (from 53.1 F g^{-1} to 30.4 F g^{-1}), it indicates GH-2.5CN is more rate stability than pure GH. Further detailed comparison of as obtained specific capacitance with all samples at different current density is shown in Table.4-2.

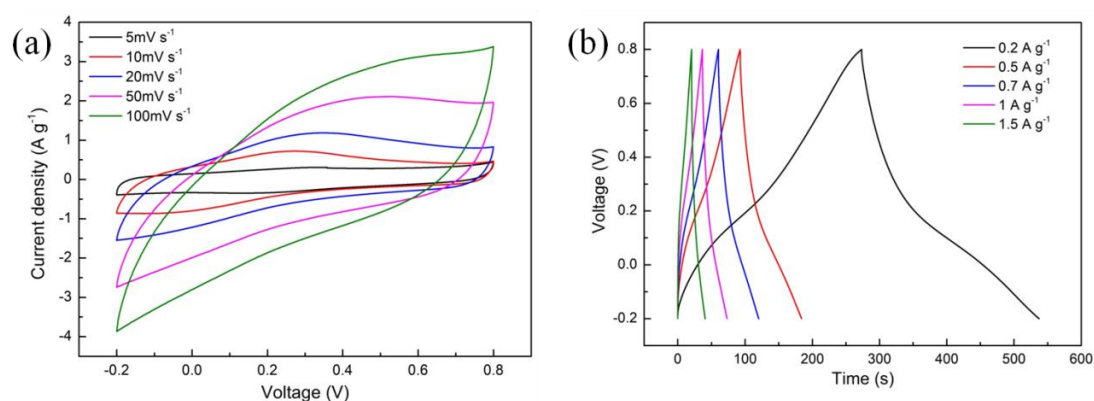


Fig. 4-10 (a) CV curves of GH at different scan rates from 5 to 100 mV s^{-1} ; (b) GCD curves of GH-2.5CN at different current density from 0.2 to 1.5 A g^{-1}

The Nyquist plots of the hybrid hydrogels obtained using AC electrochemical impedance spectroscopy in the frequency range of 10 kHz to 0.01 Hz are shown in Fig.4-9f. All curves show an intersection at the real axis at high frequencies, which describes the intrinsic internal resistance in series (R_s) of the electrochemical system; a semicircular at high to intermediate frequencies (the insert in Fig.4-9f), related to the Faradic charge transfer resistance on the electrolyte/electrode interface (R_{ct}); a 45° Warburg region in the mid-frequency range, referred to the electrolyte ion diffusion in the bulk of electrode (Z_w), the straight line in the low frequency region, revealing the ideal capacitive behavior. Comparing the impedance plots of the electrodes, the R_s of GH, GH-1CN, GH-2.5CN and GH-5CN electrodes are 5.42Ω , 5.08Ω , 4.71Ω and 5.30Ω , respectively. Obviously, the R_s of GH-2.5CN is lower than others, suggesting that the GH-2.5CN electrode has lower internal resistance. The R_{ct} of GH, GH-1CN, GH-2.5CN and GH-5CN electrodes are 69.68Ω , 23.29Ω , 11.71Ω and 25.8Ω , respectively. The lowest R_{ct} of GH-2.5CN electrode indicates lowest charge transfer resistance and fastest Faradic reaction at the electrolyte/electrode interface. Additionally, GH-CN composites electrodes all exhibit a shorter 45° Warburg region

at middle frequencies and a more vertical line at low frequencies than pure GH electrode. The above results demonstrate the addition of g-C₃N₄ QDs into GH has enhanced conductivity and promoted ion diffusion/transport capability at the electrode/electrolyte interface. Note that the observed electrochemical characters for the g-C₃N₄ QDs doped graphene hydrogel are much better than those reported for other graphene hydrogel-based and carbon-based materials, as listed in Table.1. It seems that g-C₃N₄ QDs doping offers new active sites and helps in the formation of interconnected porous structure, which enhanced the Faradic reaction and electron transfer, leading to the observed increase in the capacitance.

Table 4-1 Specific capacitance of as-prepared electrodes at different scan rate

Sample	5 mV s ⁻¹	10 mV s ⁻¹	20 mV s ⁻¹	50 mV s ⁻¹	100 mV s ⁻¹
GH	93.2	84.1	67.6	44.5	29.4
GH-1CN	198.9	185.8	168.7	140.2	113.2
GH-2.5CN	385.8	335.0	267.0	162.7	134.9
GH-5CN	140.8	130.9	116.8	100.0	86.8

Table 4-2 Specific capacitance of as-prepared electrodes at different current density.

Sample	0.2 A g ⁻¹	0.5 A g ⁻¹	0.7 A g ⁻¹	1 A g ⁻¹	1.5 A g ⁻¹
GH	53.1	46.2	41.3	38.0	30.4
GH-1CN	121.6	110.1	107.1	101.8	101.6
GH-2.5CN	243.2	229.7	221.3	213.7	201.6
GH-5CN	112.1	103.4	99.7	95.1	89.1

Table 4-3 Comparison of the specific capacitance, potential window, and experimental conditions of the reported supercapacitor electrodes made of graphene hydrogel-based and carbon-based materials measured in 3 electrodes system to our work.

Materials	Synthesis	Electrolyte	Capacitance (F g ⁻¹)	Condition	Potential window (V)	Ref.
N-doped	Solvotherm	25%	205	5 mV s ⁻¹	-0.5 to	[32]

graphene hydrogel	al method	KOH				0.5	
N-doped graphene aerogels	Hydrothermal	6M KOH	175	0.5 A g^{-1}	-1 to 0		[33]
N-doped graphene	Solid microwave method	6M KOH	197	0.5 A g^{-1}	-0.9 to 0		[34]
Graphene hydrogels	Chemical method	6M KOH	190	0.5 A g^{-1}	0 to 1		[35]
N/P co-doped carbon	Solvent evaporation	1M H_2SO_4	206	0.5 A g^{-1}	-0.1 to 0.9		[36]
rGO-aramid nanofiber hydrogel	Sol-gel method	6M KOH	190	5 mV s^{-1}	0 to 1.0		[37]
Conjugated microporous polyporphyrin coated GH	Hydrothermal	1M H_2SO_4	182.7	0.5 A g^{-1}	0 to 1.0		[38]
Dense graphene microspheres	Water bath	6M KOH	179	0.2 A g^{-1}	0 to 1.0		[39]
g-C ₃ N ₄ QDs doped graphene hydrogel	Hydrothermal	6M KOH	385.8 243.2	5 mV s^{-1} 0.2 A g^{-1}	-0.2 to 0.8		This work

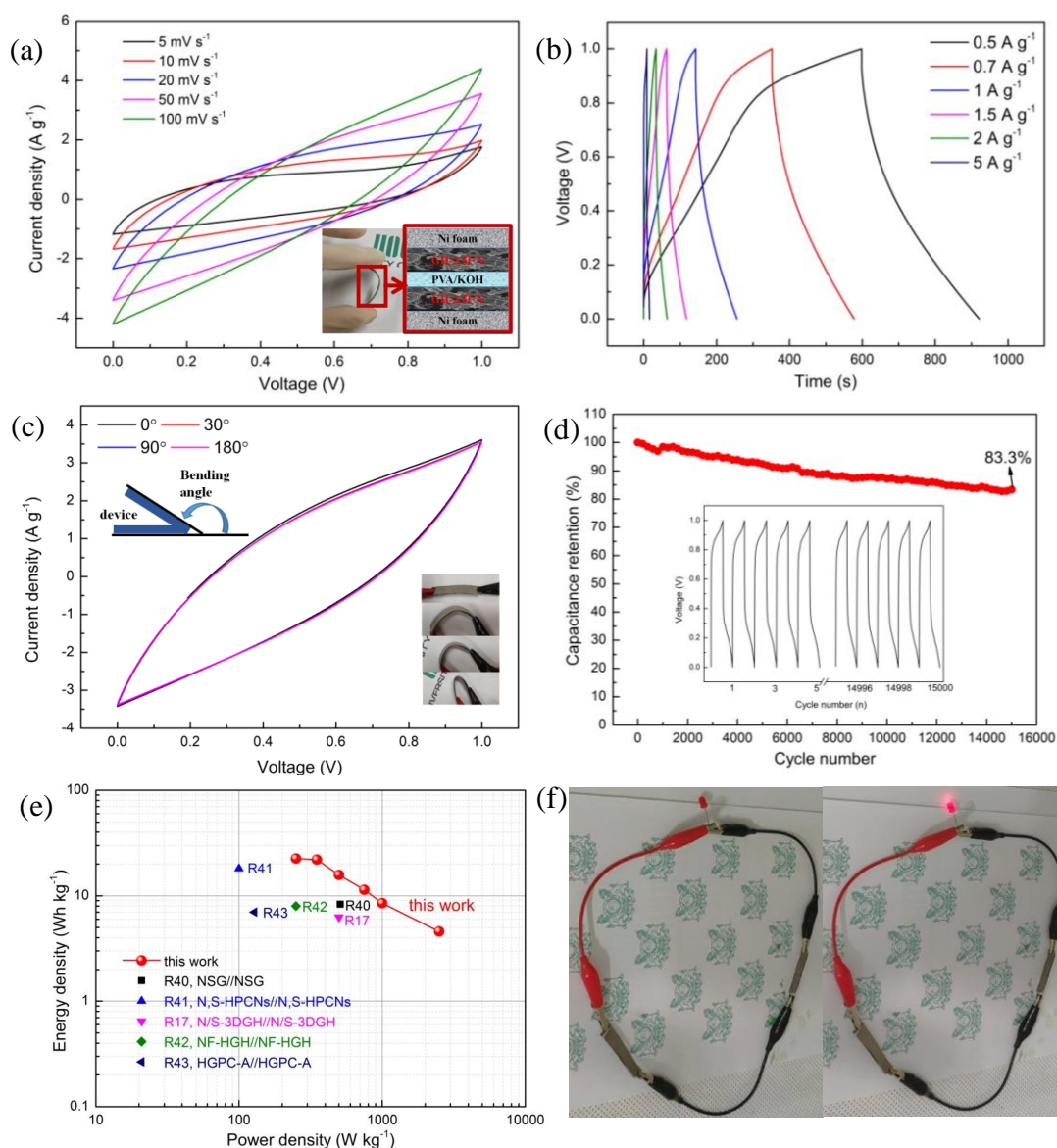


Fig. 4-11 Two-electrode electrochemical performance of GH-CN//GH-CN solid-state symmetric supercapacitor (SSC) in KOH/PVA electrolyte. (a) CV curves of the device at various scan rates from 5 to 100 mV s^{-1} (insert are the photograph of device and schematic diagram); (b) GCD curves of the device at different current density from 0.5 to 5 A g^{-1} ; (c) CV curves of the device under different bending conditions at a scan rate of 50 mV s^{-1} (insert are photographs of the device under different bending conditions) (d) Cycling test of the device over 15000 cycles at a current density of 5 A g^{-1} (insert is the charge/discharge profiles at the rate of 5 A g^{-1}); (e) Ragone plot of the device derived from the GCD curves and other results from the literatures; (f) The photograph of the device connected in series lighting the red LED.

To further evaluate the electrode for real application, all-solid state symmetric supercapacitors (SSC) were fabricated by employing GH-2.5CN composites electrodes as cathode and anode and filter paper (PTFE) as a separator with PVA/KOH gel electrolyte. The insert photograph in Fig.4-11a is the schematic diagram of the SSC device. As shown in Fig.4-11a, the shape of CV curves of the as-fabricated GH-CN//GH-CN symmetric supercapacitors at different scanrates from 5 to 100 mV s^{-1} is well maintained, indicating stable rate capability. The mass specific capacitance of the SSC at various scan rates calculated from the CV curves by using equation (1), the highest specific capacitance was 211.15 F g^{-1} at a scan rate of 5 mV s^{-1} . Fig.4-10b show the GCD curves of the as-synthesized device at current densities varying from 0.5 to 5 A g^{-1} . The specific capacitance can be determined by the GCD curves using the equation (2), the specific capacitance reached a maximum of 162.27 F g^{-1} at a current density of 0.5 A g^{-1} . To further evaluate the practicality of the SSC in the actual situation, the bending test was performed under different bending conditions. Fig.4-11c shows that the CV curves are almost unchanged at different bending degrees of 0° ; 30° ; 90° and 180° (Fig.4-11c insert), which reveals excellent flexibility and electrochemical stability. Fig.4-11d exhibits the cyclic stability of the GH-CN//GH-CN SSC that retained 83.3% capacitance of its initial value after 15000 cycles at current density of 5 A g^{-1} . The excellent cyclic stability of the device can be ascribed to the high stability of the 3D porous network structure and the g- C_3N_4 QDs embedded in the network, it's also because of the good contact between electrode and gel electrolyte.

Energy density and power density are regarded as the two main parameters to investigate and were obtained from the equation (3) and (4). The Ragone plot of the SSC device is shown in Fig.4-11e, which exhibits a high energy density of 22.5 Wh kg^{-1} at a power density of 250 W kg^{-1} . Moreover, a high power density of 2500 W kg^{-1} can be obtained when the energy density is as high as 4.6 Wh kg^{-1} . This energy density values, are higher than those of recently reported other symmetric energy storage devices such as NSG//NSG (8.3 Wh kg^{-1} at power density of 510 W kg^{-1}) [40], N,S-HPCNs//N,S-HPCNs (18.1 Wh kg^{-1} at power density of 100 W kg^{-1}) [41], N/S-3DGH//N/S-3DGH (6.25 Wh kg^{-1} at power density of 500 W kg^{-1}) [17],

NF-HGH//NF-HGH (7.99 Wh kg^{-1} at power density of 250 W kg^{-1}) [42], and HGPC-A//HGPC-A (7.0 Wh kg^{-1} at power density of 128 W kg^{-1}) [43]. To meet the needs of the operating voltage and energy output for practical applications, two SSCs assembled in serial can light a commercial red LED (in Fig.4-11f).

4.6 Conclusion

In this work, rational GH-CN hybrid hydrogels with porous network structure were self-assembled by dispersion of g-C₃N₄ QDs in GO solutions via a hydrothermal reaction. The g-C₃N₄ QDs play an important role in enhancing the pseudocapacitive activity, conductivity and promoted ion diffusion/transport capability. Benefiting from the synergistic effects of g-C₃N₄ QDs and porous network graphene hydrogel, the typical GH-CN electrode showed the highest specific capacitance of 385.8 F g^{-1} at 5 mV s^{-1} and 243.2 F g^{-1} at 0.2 A g^{-1} . For further verification, a symmetric supercapacitor based on GH-CN electrodes was fabricated, and its electrochemical characteristic was investigated. The prepared symmetric GH-CN//GH-CN supercapacitor exhibited a maximum specific capacitance of 211.2 F g^{-1} at a scan rate of 5 mV s^{-1} . This psuoercapacitor showed good capability and excellent cycling stability, with capacitance retention maintained at 83.3% after 15000 cycles at a current density of 5 A g^{-1} . Moreover, the assembled symmetric supercapacitors showed a maximum energy density of 22.5 Wh kg^{-1} at power density of 250 W kg^{-1} and illuminated a red LED, demonstrating the potential of GH-CN as a good candidate electrode material for energy storage devices.

4.7 References

- [1] Sharma K, Arora A, Tripathi S K. *Journal of Energy Storage*, 2019, 21: 801-825.
- [2] González A, Goikolea E, Barrena J A, et al. *Renewable and Sustainable Energy Reviews*, 2016, 58: 1189-1206.
- [3] Wang G, Zhang L, Zhang J. *Chemical Society Reviews*, 2012, 41(2): 797-828.
- [4] Borenstein A, Hanna O, Attias R, et al. *Journal of Materials Chemistry A*, 2017, 5(25): 12653-12672.

- [5] Zhang L L, Zhao X S. *Chemical Society Reviews*, 2009, 38(9): 2520-2531.
- [6] Chen S M, Ramachandran R, Mani V, et al. *Int. J. Electrochem. Sci*, 2014, 9(8): 4072-4085.
- [7] Dubey R, Guruviah V. *Ionics*, 2019, 25(4): 1419-1445.
- [8] Ke Q, Wang J. *Journal of Materiomics*, 2016, 2(1): 37-54.
- [9] Chee W K, Lim H N, Zainal Z, et al. *The Journal of Physical Chemistry C*, 2016, 120(8): 4153-4172.
- [10] Lemine A S, Zagho M M, Altahtamouni T M, et al. *International Journal of Energy Research*, 2018, 42(14): 4284-4300.
- [11] Xu Y, Lin Z, Huang X, et al. *Advanced materials*, 2013, 25(40): 5779-5784.
- [12] Xu Y, Lin Z, Huang X, et al. *ACS nano*, 2013, 7(5): 4042-4049.
- [13] Khazaeli A, Godbille-Cardona G, Barz D P J. *Advanced Functional Materials*, 2020: 1910738.
- [14] Chen P, Yang J J, Li S S, et al. *Nano Energy*, 2013, 2(2): 249-256.
- [15] Liu D, Fu C, Zhang N, et al. *Electrochimica Acta*, 2016, 213: 291-297.
- [16] Liao Y, Huang Y, Shu D, et al. *Electrochimica Acta*, 2016, 194: 136-142.
- [17] Zhang W, Chen Z, Guo X, et al. *Electrochimica Acta*, 2018, 278: 51-60.
- [18] An H, Li Y, Long P, et al. *Journal of Power Sources*, 2016, 312: 146-155.
- [19] Feng H, Xie P, Xue S, et al. *Journal of Electroanalytical Chemistry*, 2018, 808: 321-328.
- [20] Xu L, Cheng C, Yao C, et al. *Organic Electronics*, 2020, 78: 105407.
- [21] Li Z, Wei J, Ren J, et al. *Carbon*, 2019, 154: 410-419.
- [22] Lin R, Li Z, Abou El Amaiem D I, et al. *Journal of Materials Chemistry A*, 2017, 5(48): 25545-25554.
- [23] Ashritha M G, Hareesh K. *Journal of Energy Storage*, 2020, 32: 101840.
- [24] Dong B, Li M, Chen S, et al. *ACS Applied Materials & Interfaces*, 2017, 9(21): 17890-17896.
- [25] Ghaemmaghami M, Mohammadi R. *Sustainable Energy & Fuels*, 2019, 3(9): 2176-2204.
- [26] Lin Z, Wang K, Wang X, et al. *ACS Applied Nano Materials*, 2020, 3(7): 7016-7028.

- [27] Safaei J, Mohamed N A, Noh M F M, et al. *Journal of Materials Chemistry A*, 2018, 6(45): 22346-22380.
- [28] Chen Q, Zhao Y, Huang X, et al. *Journal of Materials Chemistry A*, 2015, 3(13): 6761-6766.
- [29] Liu D, Hur S H, Chung J S, et al. *Applied Sciences*, 2020, 10(21): 7927.
- [30] Liu H, Lv X, Qian J, et al. *ACS nano*, 2020, 14(10): 13304-13315.
- [31] Zhou W, Lei S, Sun S, et al. *Journal of Power Sources*, 2018, 402: 203-212.
- [32] Chang Y, Han G, Yuan J, et al. *Journal of power sources*, 2013, 238: 492-500.
- [33] Du J, Liu L, Yu Y, et al. *Materials Chemistry and Physics*, 2019, 223: 145-151.
- [34] Wang K, Li L, Zhang T, et al. *Energy*, 2014, 70: 612-617.
- [35] Banda H, Aradilla D, Benayad A, et al. *Journal of Power Sources*, 2017, 360: 538-547.
- [36] Yan X, Yu Y, Ryu S K, et al. *Electrochimica Acta*, 2014, 136: 466-472.
- [37] Shah S A, Kulhanek D, Sun W, et al. *Journal of colloid and interface science*, 2020, 560: 581-588.
- [38] Zhang M, Zhao T, Dou J, et al. *ChemElectroChem*, 2019, 6(24): 5946-5950.
- [39] Wei J, Luo C, Li H, et al. *Carbon*, 2019, 149: 492-498.
- [40] Cheng L, Hu Y, Qiao D, et al. *Electrochimica Acta*, 2018, 259: 587-597.
- [41] Xin G, Wang M M, Zhang W, et al. *Electrochimica Acta*, 2018, 291: 168-176.
- [42] Chen Y, Li Y, Yao F, et al. *Sustainable Energy & Fuels*, 2019, 3(9): 2237-2245.
- [43] Wang M, Yang J, Liu S, et al. *Journal of colloid and interface science*, 2020, 560: 69-76.

CHAPTER 5 Facile preparation of N-GQDs doped MnCO₃/ZnMn₂O₄ growing on Ni foam composites for high-performance supercapacitor electrodes

5.1 Introduction

At present, the energy depletion and environmental degradation force researchers to study for new efficient energy storage devices. Supercapacitors have aroused growing attention because of their rapid charging and discharging behavior, admirable power density, safety, and high green factor [1,2]. Pseudocapacitors operate through a reversible redox reaction of the active material such as transition metal compound leading to better electrochemical properties than those of electrochemical double-layer capacitors (EDLC) that store the charges in an electric double layer [3-5]. The active material on the electrodes is the most significant part of the supercapacitor, which directly determines the performance of the device. Therefore, it is very critical for energy storage devices to prepare high-performance electrode materials.

In recent years, a variety of pseudocapacitive electrode materials, such as transition metal oxides/hydroxides/sulfides/carbonate have been used as the electrode material for high performance capacitances to realize the practical applications of SCs [6-10]. Many binary transitionmetal oxides, such as ZnCo₂O₄, NiCo₂O₄, ZnMn₂O₄, and ZnFe₂O₄, have been assessed as high capacity electrodes for SCs and Li-ion batteries because of their low cost, environmentally friendly nature, and very good electrochemical performance [11-14]. Moreover, first rate composites containing oxides for supercapacitor electrode materials, such as ZnO@MnCo₂O₄, MnO₂@CoNiO₂, and Fe₃O₄@Fe₂O₃ etc., have been designed and investigated for further improvements in the electrochemical performance of supercapacitors [15-17]. Hu et al. reported starfish-shaped porous Co₃O₄/ZnFe₂O₄ hollow nanocomposites on Ni foam through a simple hydrothermal, which exhibited an excellent specific capacitance of 326 F g⁻¹ at 1 A g⁻¹. [18] Reddy et al reported unique ZnMn₂O₄@ZnFe₂O₄ microspheres were fabricated on Ni foam using a facile and cost-effective

hydrothermal method for high-performance supercapacitor applications, and the results showed that the $\text{ZnMn}_2\text{O}_4@\text{ZnFe}_2\text{O}_4$ electrode exhibits a high specific capacitance of 1024.66 F g^{-1} at 10 mA cm^{-2} [19]. Therefore, combining two types of binary metal compounds to form a unique hierarchical nanostructure is one of the best routes to improve the electrochemical performance.

In addition, graphene quantum dots (GQDs), as zero-dimensional graphitic nanocrystals with the size of only several nanometers, have been highly concerned in electrochemical field owing to their unique structure and superior properties. GQDs have much higher edge/core atomic ratios than usual carbon materials, which could greatly enhance electrochemical activities of electrodes [20-23]. Doping N atom on carbon materials has also been considered as an effective way to enhance supercapacitive performance of carbon electrode materials by providing extra pseudocapacitance due to the faradaic interactions between electrolyte ions and carbon surface. Therefore, N-doped GQDs (N-GQDs) can serve as highly electrochemically active carbon materials to combine with metal oxides for high capacitive performance [24-27].

In this study, novel hierarchical N-GQDs/ $\text{MnCO}_3/\text{ZnMn}_2\text{O}_4$ composites were grown directly on Ni foam by simple hydrothermal method followed by calcinations treatment for applications as high rate electrodes in supercapacitors. The N-GQDs/ $\text{MnCO}_3/\text{ZnMn}_2\text{O}_4$ composites exhibited excellent electrochemical properties, including a high specific capacitance of 960.6 F g^{-1} , as well as better cycling stability than $\text{MnCO}_3/\text{ZnMn}_2\text{O}_4$ (450.3 F g^{-1}). The homogeneously dispersed N-GQDs can increase the conductivity and activity sites. In addition, the electrochemical experiments including cyclic voltammetry (CV), galvanostatic charge-discharge (GCD), and electrochemical impedance spectroscopy (EIS) were performed to understand the electron transport behaviors as well as to calculate the superior specific capacitance in 1 M KOH electrolyte. Moreover, Ragone plot was used to compare the energy density and mechanical stability of N-GQDs/ $\text{MnCO}_3/\text{ZnMn}_2\text{O}_4$ with the other reported results. Results clearly indicate that the combination of N-GQDs and $\text{MnCO}_3/\text{ZnMn}_2\text{O}_4$ can constitute a promising binary metal-based electrode material with superior supercapacitive performance, which can provide an alternative to design

the quantum dots decorated novel binary metal compounds materials with sample methods for a wide variety of electrochemical application such as supercapacitors, batteries, and hydrogen evolution from water.

5.2 Materials and methods

5.2.1 Chemicals

Zinc acetate dehydrate, Manganese acetate tetrahydrate and Urea were obtained from Daejung chemicals & metals CO.LTD. Ammonium fluoride was purchased from Sigma Aldrich. Citric acid monohydrate was the products of OCI company LTD. All the chemicals were of extra pure grade and were used as received. Moreover, bi-distilled deionized (DI) water was used to prepare all the solutions unless otherwise mentioned.

5.2.2 Synthesis of N-GQDs

The N-GQDs were fabricated by dissolving 0.21 g citric acid and 0.18 g urea into 5 mL of bi-distilled deionized water and stirred to form a clear solution. The solution was then transferred into a 50-mL Teflon lined stainless autoclave. The sealed autoclave was heated to 160 C in an oven and kept for additional 4 h. After hydrothermal reaction, the autoclave was cooled down naturally. The obtained aqueous solution was centrifuged at 5000 rpm for 5 min to dislodge the deposit and obtain the upper aqueous solution for further use. The upper aqueous were dialyzed with dialysis membrane (3500 MWCO) over all night and the dialyzed aqueous were collected as pristine N-GQDs solution.

5.2.3 Fabrication of $\text{MnCO}_3/\text{ZnMn}_2\text{O}_4$ and N-GQDs/ $\text{MnCO}_3/\text{ZnMn}_2\text{O}_4$

In a typical synthesis, 0.002 mol of Manganese(II) acetate tetrahydrate ($\text{Mn}(\text{CH}_3\text{COO})_2 \cdot 4\text{H}_2\text{O}$) and 0.001 mol of Zinc(II) acetate dehydrate ($\text{Zn}(\text{CH}_3\text{COO})_2 \cdot 2\text{H}_2\text{O}$) were dissolved in 70 mL of deionized water (DI) in a 100 mL

beaker. To the above mixture, 0.006 mol of ammonium fluoride were added to modify the size and structure, then 0.015 mol of urea was added and the solution mixture was allowed to stir for 20 min. Then the above solution was transferred to a 90 mL hydrothermal autoclave including a piece of Ni foam (2 cm×3 cm). The autoclave was maintained at 120°C for 5 h in a heated oven and after cooling the product to room temperature and repeatedly washed with deionized water for 5 times, and then dried at 60°C in a vacuum oven. Finally, the precursor was calcined at 350°C for 2 h in air to obtain the hierarchical MnCO₃/ZnMn₂O₄ composites on Ni foam and named as MC/ZM.

For the preparation of N-GQDs/MnCO₃/ZnMn₂O₄ composite, the synthesis method was the same as MnCO₃/ZnMn₂O₄ except adding 2ml N-GQDs (0.5mg ml⁻¹) solution with the mixed solution to the autoclave. And the N-GQDs/MnCO₃/ZnMn₂O₄ composite was named as N/MC/ZM.

5.2.4 Materials characterization

The chemical composition and crystal phase of MC/ZM and N/MC/ZM on Ni foam were characterized by X-ray powder diffraction was performed using a Bruker D8 Advance diffractometer with a non-monochromated Cu K α operated at 40 kV and 30 mA. Fourier transform infrared (FTIR) spectra were obtained using a Nicolet IR 200 FT-IR spectrometer (Thermo Scientific). X-ray photoelectron spectroscopy (XPS: Thermo Fisher) measurements were performed using monochromatic AlK α radiation ($h\nu = 1486.6$ eV). The morphology of MC/ZM and N/MC/ZM on Ni foam was tested through Scanning Electron Microscopy (JEOL FESEM-JSM820), the composition was also analyzed by energy dispersive X-ray spectroscopy (EDS) attached to the SEM instrument. High-resolution transmission electron microscopy (HRTEM) and selected area electron diffraction (SAED) observations were carried out (JEOL-JEM-F200) at 200 kV.

5.2.5 Electrochemical measurements

Electrochemical performance was investigated by cyclic voltammetry (CV),

galvanostatic charge/discharge (GCD), and electrochemical impedance spectroscopy (EIS) tests. All electrochemical measurements were performed using a BioLogic VSP electrochemical workstation at room temperature. A three-electrode system was used to test the electrochemical performance of the prepared electrodes with platinum foil and Hg/HgO electrodes as the counter and reference electrodes, respectively. The Ni-foam covered with MC/ZM and N/MC/ZM was cut into small pieces and the loading density of MC/ZM and N/MC/ZM on Ni foam was calculated to be around 1.5-1.7 mg cm⁻², the small piece was used directly as a working electrode. All electrochemical tests were performed in an aqueous electrolyte of 1 M KOH at room temperature. EIS was performed at open circuit potential in a frequency range from 10 kHz to 0.01 Hz with an AC amplitude of 5 mV. The solid-state flexible ASC were prepared using the MC/ZM and N/MC/ZM as positive and negative electrodes, respectively, which were assembled with PVA/KOH gel electrolyte and filter paper as a separator. The prepared two electrodes were wetted with the PVA/KOH gel electrolyte for 10 min and then assembled face to face with filter paper using gentle pressure.

The specific capacitance (Cs) of the product can be calculated from the CV curves and galvanostatic charge-discharge curves according to the following equation:

$$C_s = \frac{\int I(V) dV}{v \times m \times \Delta V} \quad (1)$$

$$C_s = \frac{I \times \Delta t}{m \times \Delta V} \quad (2)$$

where $\int I(V) dV$ is the area enclosed by the CV curves, ΔV (V) is the potential window, v (mV s⁻¹) is the potential scan rate, m (g) is the mass of the active materials in the electrodes, and Δt (s) is the discharge time.

The energy density E (Wh kg⁻¹) and power density P (W kg⁻¹) of the device were calculated using the following equations:

$$E = \frac{C_s \times (\Delta V)^2}{2 \times 3.6} \quad (3)$$

$$P = \frac{3600 \times E}{\Delta t} \quad (4)$$

5.3 Results and discussion

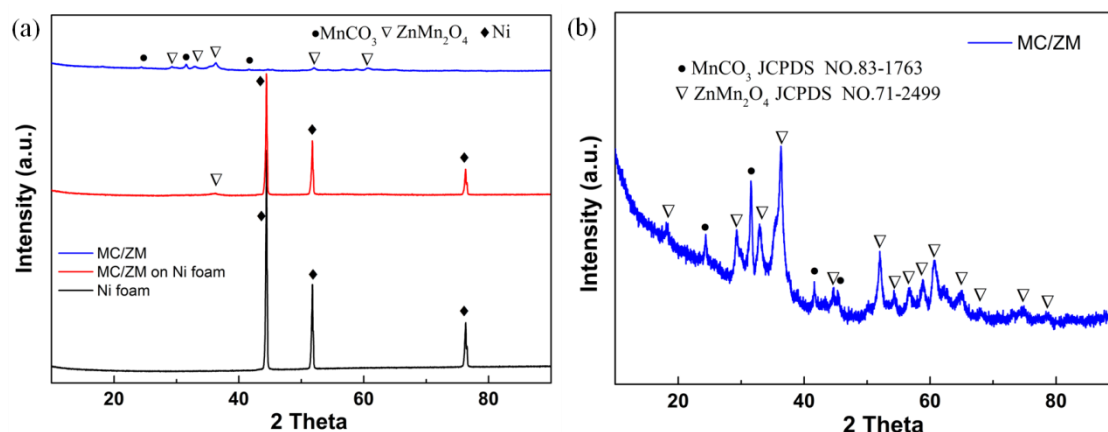


Fig. 5-1 (a) XRD patterns for the prepared MC/ZM composites, MC/ZM on Ni foam and Ni foam; (b) XRD patterns for MC/ZM (enlarged degree).

Fig.5-1a reveals the crystal structure of hierarchical MC/ZM, MC/ZM on Ni foam and Ni foam for XRD analysis. It is significant that there are the typical peaks at $2\theta=44.5^\circ$, 51.8° and 76.4° derived from Ni foam (JCPDS NO.70-1849). For as prepared MC/ZM on Ni foam, it can be seen that all the diffraction peaks of MC/ZM is inconspicuous except a weak peak of ZnMn_2O_4 phase owing to the strong impact of Ni substrate. In order to confirm the phases of the MC/ZM composite, the MC/ZM was peeled off from the Ni foam. In Fig.5-1b, it clearly can be seen that there're two kinds phases of diffraction peaks of the MC/ZM hierarchical structures could be assigned to the phase of ZnMn_2O_4 (JCPDS NO.71-2499) and MnCO_3 (JCPDS NO.83-1763) [28]. In detail, the typical peaks at $2\theta=18.2^\circ$, 29.3° , 33.0° , 36.0° , 44.7° , 51.9° , 54.4° , 56.7° , 59.0° , 60.8° , 61.9° , 65.1° , 68.3° , 75.0° and 78.6° derived from ZnMn_2O_4 phase, and the peaks at $2\theta=24.3^\circ$, 31.5° , 41.6° and 45.4° can be derived from MnCO_3 phase. These results also implied the formation of $\text{MnCO}_3/\text{ZnMn}_2\text{O}_4$ composite on Ni foam successfully.

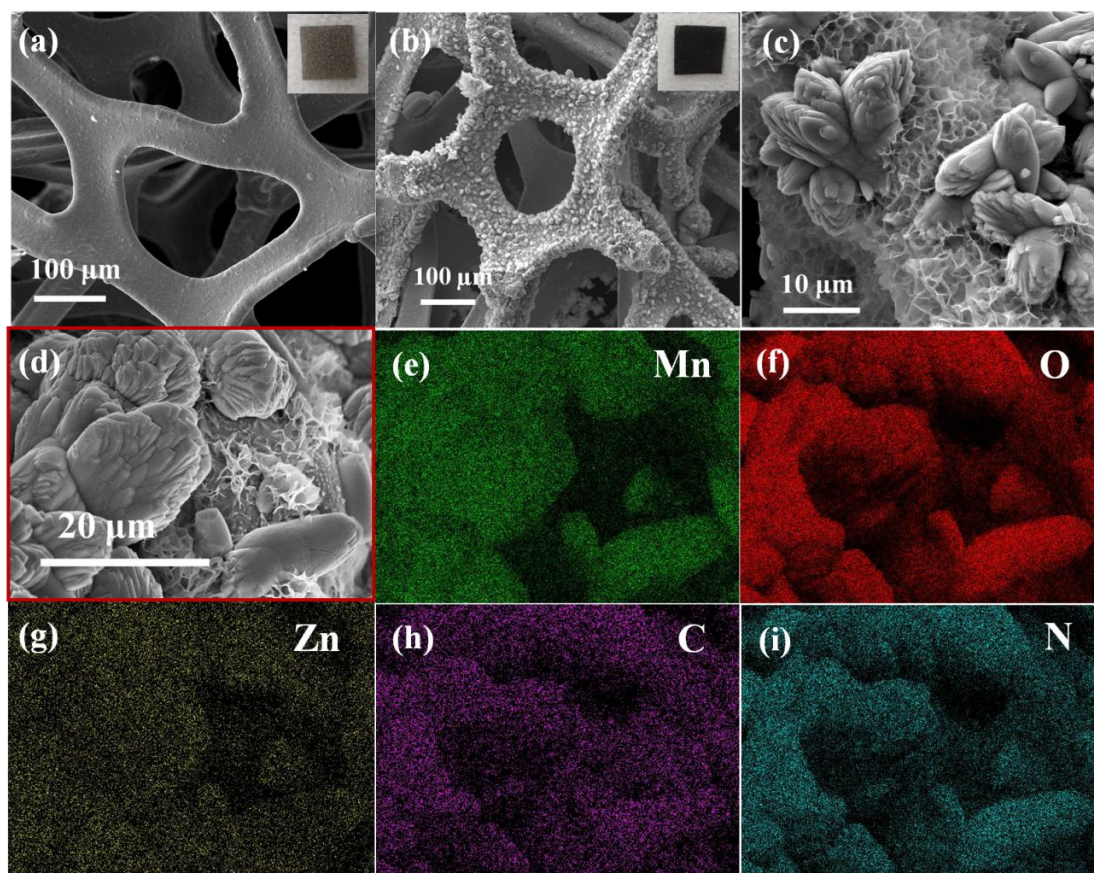


Fig.5-2 SEM images in different magnifications : (a) Ni foam; (b-d) hierarchical N/MC/ZM on Ni foam; (e-i) EDS elemental mapping images (of Fig.5-2d).

Fig.5-2a shows the typical morphology of three-dimensional conductive framework structure to Ni foam, which can provide good supporting effect for electrodes, making for the transmission of electrons and ions, and can enhance the conductivity of materials. Fig.5-2b-d illustrate the structure of MC/ZM on Ni foam, it's clearly seen that the hierarchical porous nanosheets growing uniformly on the substrate surface of Ni foam, and some particles dispersed on the nanosheets. There is enough space between the interconnected nanosheets, which accommodates the strain induced by the volume change in the process of discharging and charging. For the sheet structure of nanometer thickness, it can shorten the diffusion path of ion transport, and be beneficial to charge transfer, ion diffusion and the infiltration of electrolyte, thereby the electrochemical performance could be improved. From the mapping test of Fig.5-2d, the elements disperse of Mn, O, Zn, C and N were shown in Fig.5-2e-i respectively. In Fig5-2e, most Mn element dispersed on the particles and a small amount dispersed on

the nanosheets. And in Fig.5-2f, the oxygen element dispersed uniformly on the sample. The zinc element distributed most area of the sample in Fig.5-2g, because the nanosheets also exist under the particles. Combine with the results of XRD, we can make an assumption that the particles are mainly MnCO_3 phase, and the nanosheets are mainly ZnMn_2O_4 phase. In Fig.5-2h, the carbon element dispersed uniformly on the sample because the carbon element not only from the MnCO_3 but also from the adding of N-GQDs. The nitrogen element dispersed uniformly on the composite in Fig.5-2i, which indicated the addition of N-GQDs successfully. The SEM image and EDS mapping of Mn, O, Zn and C elements and EDS spectrum of MC/ZM on Ni foam were shown in Fig.5-3. It can be seen that the MC/ZM and N/MC/ZM have the same morphology, which indicate that there's no influence for the morphology with the addition of N-GQDs.

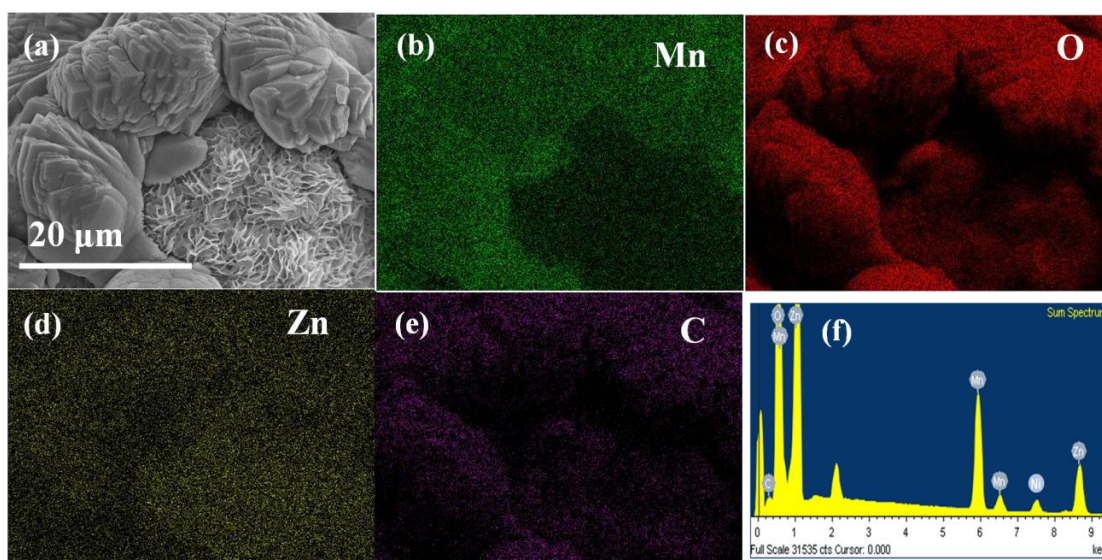


Fig.5-3 (a) SEM image of MC/ZM on Ni foam; (b-e) EDS elemental mapping images of Fig.5-3a; (f) EDS spectrum of MC/ZM on Ni foam.

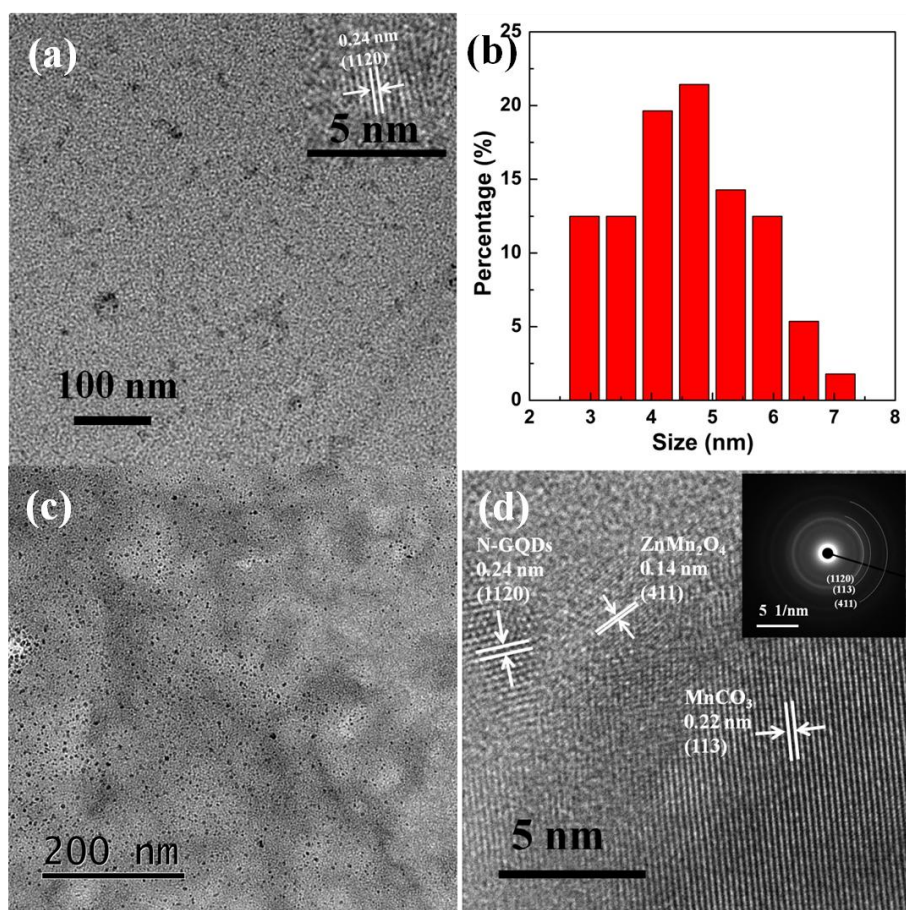


Fig.5-4 (a)TEM image of N-GQDs (insert: the HRTEM of N-GQDs) ; (b) the size-distribution of N-GQDs; (c) TEM and (d) HRTEM images of N/MC/ZM composite (insert: corresponding SAED patterns of N/MC/ZM composite).

The TEM and insert HRTEM image of the as-prepared N-GQDs from Fig.5-4a show that they are well dispersed in the aqueous solution and the fringes distance of 0.24 nm corresponding to that of graphene (1120) plane, this means that the as-prepared N-GQDs have a good crystalline structure. The histogram in Fig. 5-4b indicates that the particle sizes of N-GQDs are 2.6-7.0 nm with an average diameter of 4 ± 0.6 nm, which is corroborated with the previously reported data. Furthermore, the TEM image shows a homogeneous distribution of N-GQDs onto the MC/ZM composite (Fig.5-4c). Since the particle size of N-GQDs onto MC/ZM is too small, the HRTEM is further used to characterize the existence of N-GQDs, ZnMn_2O_4 and MnCO_3 . As illustrated in Fig 5-4d, the HRTEM image of N-GQD/ MnCO_3 / ZnMn_2O_4 shows the distribution of a size about 5 nm N-GQDs with fringes distance of 0.24 nm corresponding to that of graphene (1120) plane onto MC/ZM structures, which is consistent with the as-prepared

N-GQDs. In addition, the lattice spacing of 0.22 nm and 0.14 nm are observed, which are the (113) plane of MnCO_3 and (411) plane of ZnMn_2O_4 , respectively. These results strongly indicate the successful embedment of N-GQDs into MC/ZM structures. The inset portion of Fig.5-4d is the SAED pattern of the composite material, and the polycrystalline ring shows the corresponding (1120), (113) and (411) crystal plane of the composite. The results correspond exactly to our XRD pattern, which further indicates the synthesis of N/MC/ZM composites.

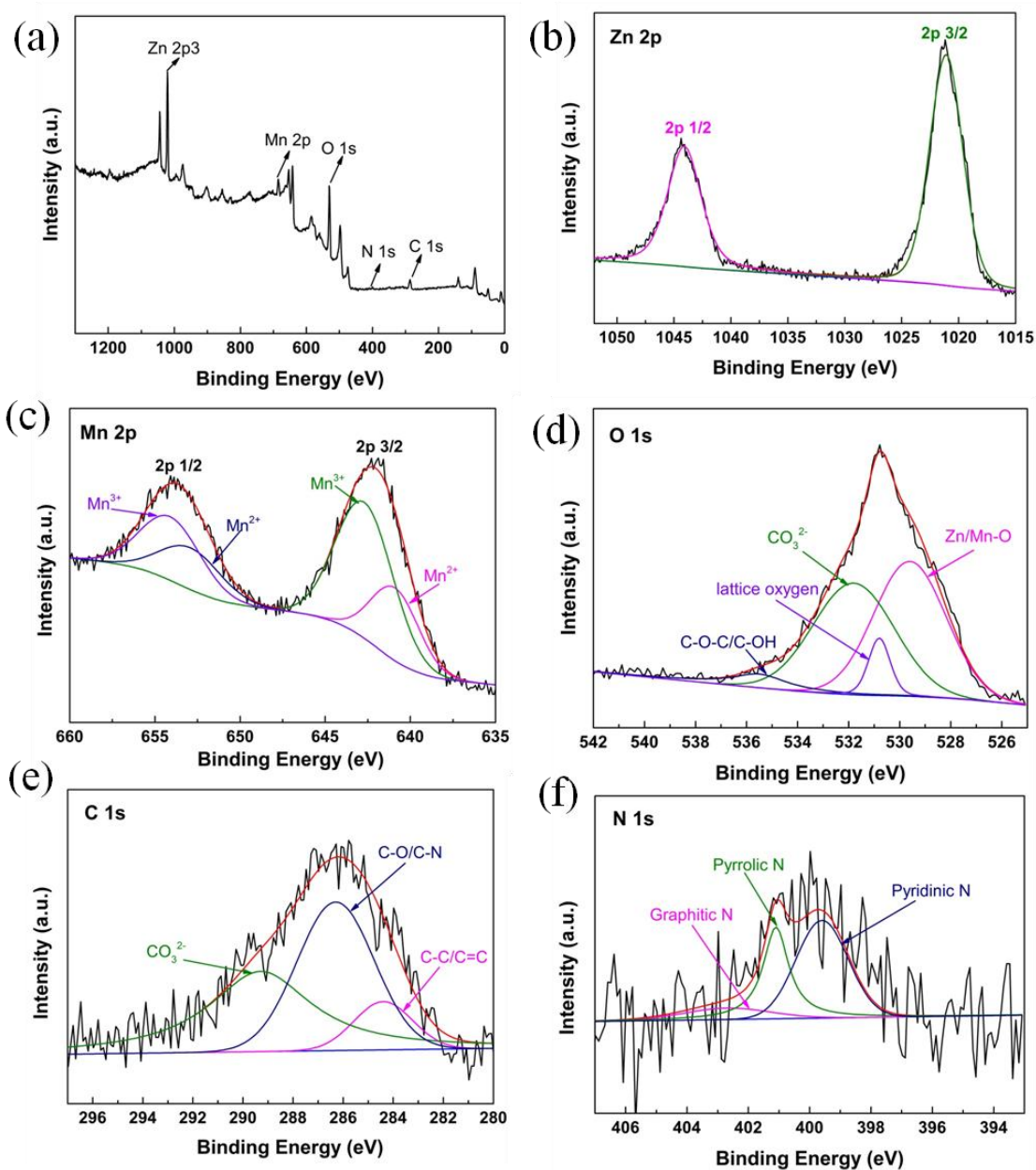


Fig.5-5. (a) XPS survey spectra (b) Zn 2p (c) Mn 2p (d) O 1s (e) C 1s (f) N 1s of N/MC/ZM sample.

The corresponding XPS profiles of N/MC/ZM are displayed in Fig.5-5, indicating the chemical bond on the samples. The full survey spectrum of N/MC/ZM is shown in Fig.5-5a, there are five elements of Zn, Mn, O, N and C are detected in it, it also indicate that the N-GQDs are successfully doped on MC/ZM. To get detailed chemical states information, the high-resolution XPS spectra of Zn 2p, Mn 2p, O 1s, C 1s and N 1s are recorded. As illustrated in Fig.5-5b, a high-resolution spectrum of Zn 2p show two peaks at 1021.2, 1044.3 eV with an energy difference of 23.1 eV attributes to Zn 2p_{3/2} and Zn 2p_{1/2}, which is in good agreement with Zn²⁺ oxidation states[29]. The Mn2p high-resolution spectrum is presented in Fig. 5-5c. The two major peaks located at 642.1 eV and 653.7 eV, belong to the Mn 2p_{3/2} and Mn 2p_{1/2}. These fitting peaks at 640.9 eV and 652.9 eV are corresponding to Mn²⁺ oxidation state. The two peaks at 643 eV and 654.1 eV were related to the Mn³⁺ oxidation state[30]. In Fig.5-5d, the O1s peaks display four fitting peaks at 529.6 eV, 531.3 eV, 531.8 eV and 535.5 eV corresponding to the representative metal-oxygen bond, lattice oxygen, CO₃²⁻ and C-O-C/C-OH respectively[31-34]. These results indicate that the successful synthesis of MnCO₃/ZnMn₂O₄. Fig. 5-5e shows the high-resolution spectrum of C 1s peak of N/MC/ZM. Three major peaks at 284.7 eV, 286.3 eV and 289.3 eV are clearly observed in the C 1s peak. Peaks at 284.7 eV, 286.3 eV are the aromatic C-C/C=C and C-O/C-N groups, respectively, while another peak belong to CO₃²⁻ at 289.3 eV, which confirm the successful doping of N-GQDs[35]. For N1s of GH-2.5CN, as illustrated in Fig.5-5f, there're three peaks locate at the binding energies of 399.6 eV, 401.1 eV and 402.7 eV, which can be ascribed to pyridinic N, pyrrolic N and graphitic N, respectively. In these three nitrogen bonding configurations, pyrrolic N is in sp³-hybridized state and pyridinic N is in sp²-hybridized state, they are both negative charge. However, graphitic N is positive charge and in the sp²-hybridized state. Therefore, pyrrolic N and pyridinic N can generate pseudocapacitance via Faraday reactions, while graphitic N can enhance the conductivity of graphene materials through the positive charge and its repair effect on graphene sheets. It is noteworthy that the deconvoluted results of O 1s , C 1s and N 1 s indicate the existence of hydrophilic functional groups in the N/MC/ZM nanomaterials, which may feature the pseudo-capacitive behavior, particularly in the presence of aqueous electrolytes, to enhance the electrochemical performance of

N/MC/ZM [36,37].

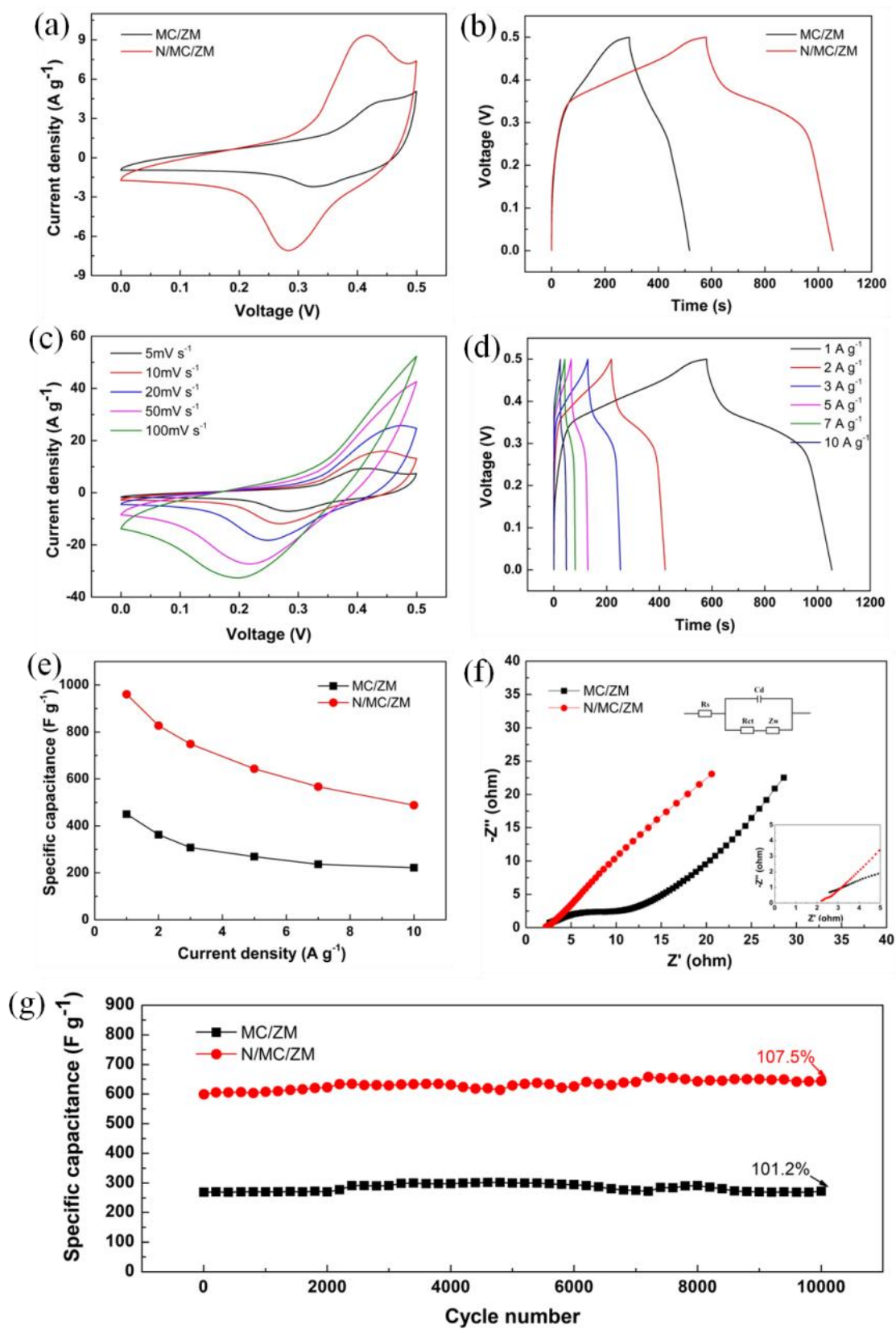


Fig.5-6 (a) CV curves of MC/ZM and N/MC/ZM electrodes at the scan rate of 5 mV/s

in 1.0 M KOH electrolyte; (b) GCD curves of MC/ZM and N/MC/ZM electrodes at 1 A g⁻¹ current density; (c) CV curves of N/MC/ZM electrode at different scan rates of 5-100 mV s⁻¹; (d) GCD curves of N/MC/ZM electrode at different current densities of 1-10 A g⁻¹; (e) the specific capacitance of MC/ZM and N/MC/ZM electrodes at different current densities derived from GCD; (f) Nyquist plots of MC/ZM and N/MC/ZM electrodes in 1.0 M KOH electrolyte and its equivalent circuit model (insert shows the curves obtained in the high frequency region); (g) cycling performance of MC/ZM and N/MC/ZM at 5 A g⁻¹.

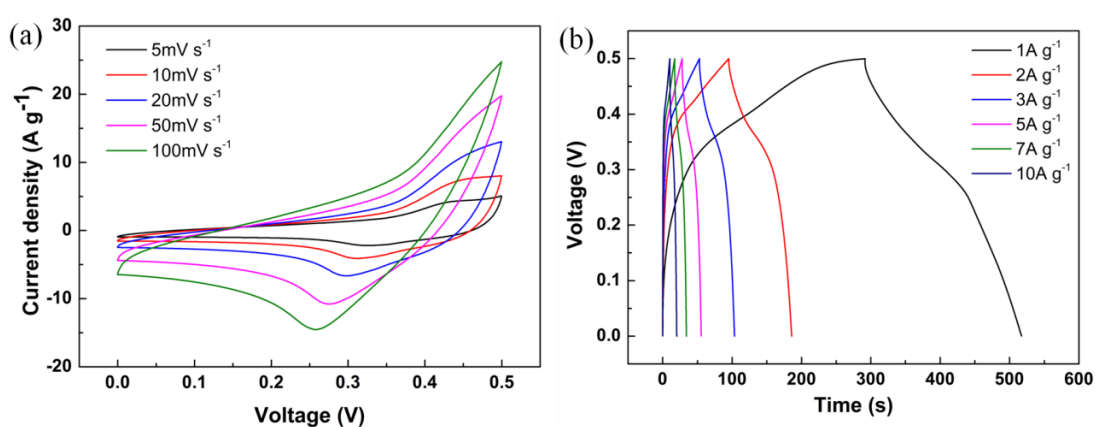


Fig.5-7. (a) CV curves of MC/ZM at different scan rates and (b) GCD curves of MC/ZM at different current densities.

Cyclic voltammogram (CV), galvanostatic charge-discharge (GCD) and electrochemical impedance are the important electrochemical techniques that give adequate information about the material's electrochemical properties. Fig.5-6a shows the CV curves of capacitive performance of the MC/ZM and N/MC/ZM electrodes in the potential window of 0-0.5 V at the scan rate of 5 mV s⁻¹. As can be seen, current and storage capacity significantly enhanced with the addition of N-GQDs. Because the diffusion of protons or alkaline ions into the structure becomes easier and faradic reactions perform better after the addition of N-GQDs. The improvement of supercapacitor properties in N/MC/ZM composite mode is clearly seen by comparing the voltammograms (Fig. 5-6a). What's more, the MC/ZM and N/MC/ZM composites both have well-defined redox peaks. In the CV curves of the MC/ZM and N/MC/ZM at

5 mV s⁻¹ scan rate, two peaks were observed at the potential of 0.42V and 0.31V for MC/ZM electrode whereas the peaks were observed at 0.41V and 0.29V for N/MC/ZM. It was obvious that EDLC materials will show the rectangular curves and transition metal oxides exhibit a reversible redox peak due to the faradaic oxidation and reduction process of the materials at the surface. Wherein, pseudocapacitor materials will show the characteristics of both EDLC and metal oxides. In these two electrodes, the peaks at 0.42V or 0.41V is attributed to oxidation and the peak at 0.31V or 0.29V due to reduction. In pseudocapacitor materials, electrochemical reactions may occur through surface de/adsorption, de/intercalation along with faradaic redox reaction [38,39]. The electrochemical reaction of the composite materials can be written as:

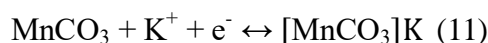
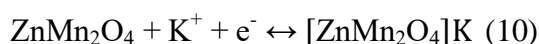
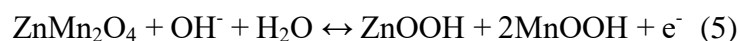


Fig.5-6b represents the GCD curves at the current density of 1 A g⁻¹ within the potential window at 0-0.5V of MC/ZM and N/MC/ZM electrodes. With the addition of N-GQDs to the composite, discharge time went up and SC value also increased according to Eq. (2). This is due to the addition of N-GQDs with MC/ZM, which promotes ion diffusion/transport capability at the electrode/electrolyte interface. and enhance the conductivity, thus facilitates the charge-discharge process and shows a better performance than MC/ZM. From the CV curves of N/MC/ZM shown in Fig.5-6c, It was observed that all the prepared N/MC/ZM composite shows a slight shift on the potential when going from low scan to high scan rates. A maximum of 0.05 V potential shifts in the oxidation of N/MC/ZM was observed between the scan rates from 5 to 100 mV s⁻¹. Further, the enhanced current was observed when increasing scan rates from 5 to 100 mV s⁻¹. It should be noted that, the shift of redox peak with increasing the scan rates was observed which is due to the high diffusion resistance and polarization.

Moreover, the enhanced current at high scan rates was aroused by high electronic and ionic transport of electrode materials. The specific capacitance of the electrode materials by CV test was calculated according to the Eq. (1). The GCD curves of N/MC/ZM was shown in Fig.5-6d, as calculated according to the Eq. (2), it's obvious that N/MC/ZM has a high specific capacitance of 960.6 F g^{-1} at 1 A g^{-1} , while the same electrode show specific capacitance of 827.5, 748.7, 643.4, 566.9, and 488.1 F g^{-1} at 2, 3, 5, 7 and 10 A g^{-1} current densities, respectively. And the detail compare of specific capacitance of MC/ZM and N/MC/ZM at different current densities were also shown in Fig.5-6e. The specific capacitance of MC/ZM was much lower than N/MC/ZM, while the values were 450.3, 362.7, 307.8, 269.0, 236.8 and 221.8 F g^{-1} at 1, 2, 3, 5, 7 and 10 A g^{-1} current densities, respectively. Moreover, the detail CV curves and GCD curves of MC/ZM were shown in Fig.5-7. To explore the mechanism, the electrochemical impedance spectroscopy (EIS) was tested in the frequency range of 0.01 Hz-10 kHz at 5 mV of amplitude and open circuit potential. Fig 5-6f shows the Nyquist plots of MC/ZM and N/MC/ZM, the Nyquist plots mainly has two parts: i) a semi-circle trend in high frequency and ii) a linear line in low frequency. All curves show an intersection at the real axis at high frequencies, which describes the intrinsic internal resistance in series (R_s) of the electrochemical system; the diameter of semi-circle represents the charge transfer resistance (R_{ct}), which is ascribed to conductivity of electrode material and a 45° Warburg region in the mid-frequency range, referred to the electrolyte ion diffusion in the bulk of electrode (Z_w). The slope of straight line indicated the diffusive resistance, related with the penetration of electrolyte ions. All samples show a semicircular trend in the high-frequency region, while a straight line in the low-frequency region. N/MC/ZM exhibits a smaller radius in high frequency region and a shorter 45° Warburg region at middle frequencies and a more vertical line at low frequencies than MC/ZM, demonstrating the lower value (0.35Ω) of charge transfer resistance and rapid diffuse of electrolyte ions than that of MC/ZM (7.2Ω). This is because of the addition of N-GQDs facilitate ion transfer throughout the structure and compensate the low conductivity of MC/ZM. The equivalent circuit was displayed in the inset of Fig. 5-6f. Typically, the N/MC/ZM reaches a remarkable cycling performance with 107.5% retention of the initial capacity after 10000 cycles at 5 A g^{-1}

(Fig.5-6g) while the MC/ZM keeps capacitance retention of 101.2% after 10000 cycles at the same current density. It indicates that this structure has a relatively good stability.

The observed high specific capacitance of N/MC/ZM composite compared to other $ZnMn_2O_4$ based materials may be attributed to the existence of N-GQDs, $ZnMn_2O_4$ and $MnCO_3$ and their synergistic effects. Table 5-1 compares the specific capacitance of the prepared N/MC/ZM materials with earlier reported $ZnMn_2O_4$ based materials reveals the prepared N/MC/ZM composite showed high specific capacitance.

Table.5-1 The specific capacitance of different $ZnMn_2O_4$ electrodes.

Material	Electrolyte	Specific capacitance $F g^{-1}$ @ Current density $A g^{-1}$	References
$ZnMn_2O_4$	1M Na_2SO_4	$240 F g^{-1}$ @ $1A g^{-1}$	[40]
$ZnMn_2O_4$	0.5M Na_2SO_4	$456.8 F g^{-1}$ @ $1A g^{-1}$	[41]
$ZnMn_2O_4/Mn_2O_3$	2M KOH	$380 F g^{-1}$ @ $0.5A g^{-1}$	[29]
$ZnMn_2O_4/Mn_3O_4$	1M Na_2SO_4	$321 F g^{-1}$ @ $1mV s^{-1}$	[42]
$ZnMn_2O_4$	1M KOH	$447 F g^{-1}$ @ $1A g^{-1}$	[43]
$ZnMn_2O_4$	6M KOH	$411.7 F g^{-1}$ @ $1A g^{-1}$	[44]
N-GQDs/ $MnCO_3$ / $ZnMn_2O_4$	1M KOH	$960.6 F g^{-1}$ @ $1A g^{-1}$	This work

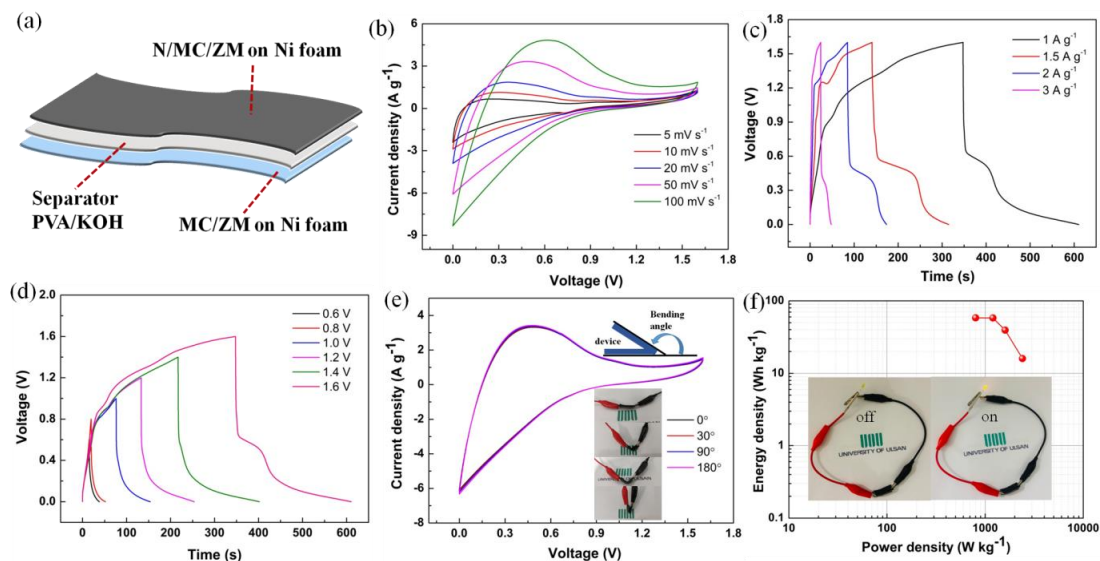


Fig.5-8. Two-electrode electrochemical performance of N/MC/ZM//MC/ZM solid-state asymmetric supercapacitor (ASC) in KOH/PVA electrolyte. (a) Schematic illustration of flexible solid-state N/MC/ZM//MC/ZM asymmetric supercapacitor. (b) CV curves and (c) GCD curves of the device. (d) GCD curves of the devices collected at different potential windows at a fixed current density of 1 A g^{-1} . (e) CV curves under different bending conditions at 50 mV s^{-1} . (f) Ragone plots of the device (insert is the photographs of LED light powered by the device).

In order to investigate the practical utilities and flexible characteristic of the promising MC/ZM and N/MC/ZM on Ni foam, the flexible solid-state asymmetric supercapacitor (ASC) MC/ZM//N/MC/ZM device is assembled and the structure is schematically illustrated in Fig.5-8a. Briefly, a piece of filter paper and a polyvinyl alcohol (PVA)/KOH gel are serving as a separator and electrolyte, respectively, which sandwiched by the MC/ZM and N/MC/ZM as cathode and anode. The CV curves of the ASC device at scan rates ranging from 5 to 100 mV s^{-1} are shown in Fig.5-8b, and the GCD curves (Fig.5-8c) display a good capacity, which reaches a prominent capacitance of 164.3 F g^{-1} at 1 A g^{-1} . As depicted in Fig.5-8d, the GCD curves of the ASC device are collected at 1 A g^{-1} with an operational voltage window ranging from 0.6 to 1.6 V, demonstrating the voltage of as-assembled ASC MC/ZM//N/MC/ZM device can be stabilized up to 1.6 V. From Fig.5-8e, when the solid-state ASC MC/ZM//N/MC/ZM device is bended to various conditions, the CV curves keep nearly the same, indicating its excellent suitability to shape deformation. Additionally,

Fig.5-8f further presents the power and energy densities of the solid-state ASC MC/ZM//N/MC/ZM device, it can reach a high energy density of 58.4 Wh kg^{-1} at the power density of 800 W kg^{-1} . To meet the needs of the operating voltage and energy output for practical applications, one ASC device can light a commercial yellow LED (in Fig.5-8f). To sum up, the outcomes mentioned above definitely suggest the ultrahigh energy density, flexibility and practical application of the ASC MC/ZM//N/MC/ZM device, which can faultlessly fulfill the avid demanding for high-performance energy storages.

5.4 Conclusion

A hierarchical structure like N-GQDs/MnCO₃/ZnMn₂O₄ composite electrode was designed and synthesized using simple, low-cost, and effective hydrothermal approach for supercapacitor applications. The resulting composite had a hierarchical structure formed with nanosheets, particles and quantum dots which provided a abundant pores for rapid electrons and ions transportation. Moreover, the dispersion of MnCO₃ particles on ZnMn₂O₄ nanosheets was more favorable to the synergistic effects, and the addition of N-GQDs enhanced higher conductivity. As a result, the N-GQDs/MnCO₃/ZnMn₂O₄ electrode exhibited a maximum specific capacitance of 960.6 F g^{-1} at 1 A g^{-1} . The solid-state ASC MC/ZM//N/MC/ZM showed good capability and excellent cycling stability, with capacitance retention maintained at 107.5% after 10000 cycles at a current density of 5 A g^{-1} . Moreover, the assembled symmetric supercapacitors showed a maximum energy density of 58.4 Wh kg^{-1} at power density of 800 W kg^{-1} and illuminated a yellow LED. Therefore, the N-GQDs/MnCO₃/ZnMn₂O₄ electrode is a promising candidate for high energy storage devices in supercapacitor applications.

5.5 References

- [1] Kumar S, Saeed G, Zhu L, et al. Chemical Engineering Journal, 2020: 126352.
- [2] Najib S, Erdem E. Nanoscale Advances, 2019, 1(8): 2817-2827.
- [3] Chodankar N R, Pham H D, Nanjundan A K, et al. Small, 2020, 16(37): 2002806.

- [4] Tang S, Zhu B, Shi X, et al. *Advanced Energy Materials*, 2017, 7(6): 1601985.
- [5] Barai H R, Lopa N S, Ahmed F, et al. *ACS omega*, 2020, 5(35): 22356-22366.
- [6] Li G, Chang Z, Li T, et al. *Ionics*, 2019, 25(8): 3885-3895.
- [7] Wang H Y, Li D G, Zhu H L, et al. *Electrochimica Acta*, 2017, 249: 155-165.
- [8] Sekhar S C, Nagaraju G, Yu J S. *Applied Surface Science*, 2018, 435: 398-405.
- [9] Karuppaiah M, Sakthivel P, Asaithambi S, et al. *Materials Chemistry and Physics*, 2019, 228: 1-8.
- [10] Himasree P, Durga I K, Krishna T N V, et al. *Electrochimica Acta*, 2019, 305: 467-473.
- [11] Wu H, Lou Z, Yang H, et al. *Nanoscale*, 2015, 7(5): 1921-1926.
- [12] Yuan C, Li J, Hou L, et al. *Advanced Functional Materials*, 2012, 22(21): 4592-4597.
- [13] Kim J G, Lee S H, Kim Y, et al. *ACS applied materials & interfaces*, 2013, 5(21): 11321-11328.
- [14] Zhu M, Zhang X, Zhou Y, et al. *RSC Advances*, 2015, 5(49): 39270-39277.
- [15] Gopi C V V M, Venkata-Haritha M, Kim S K, et al. *RSC advances*, 2016, 6(105): 102961-102967.
- [16] Reddy A E, Anitha T, Gopi C V V M, et al. *RSC advances*, 2017, 7(20): 12301-12308.
- [17] Tang X, Jia R, Zhai T, et al. *ACS applied materials & interfaces*, 2015, 7(49): 27518-27525.
- [18] Hu X W, Liu S, Qu B T, et al. *ACS applied materials & interfaces*, 2015, 7(18): 9972-9981.
- [19] Reddy A E, Anitha T, Gopi C V V M, et al. *New Journal of Chemistry*, 2018, 42(4): 2964-2969.
- [20] Wang S, Shen J, Wang Q, et al. *ACS Applied Energy Materials*, 2019, 2(2): 1077-1085.
- [21] Rahimpour K, Teimuri-Mofrad R. *Electrochimica Acta*, 2020, 345: 136207.
- [22] Ashourdan M, Semnani A, Hasanpour F, et al. *Journal of Energy Storage*, 2021, 36: 102449.
- [23] Keyang H, Ruiyi L, Zaijun L, et al. *Electrochimica Acta*, 2020, 353: 136524.

- [24] Li Z, Liu X, Wang L, et al. *Small*, 2018, 14(39): 1801498.
- [25] Li Z, Bu F, Wei J, et al. *Nanoscale*, 2018, 10(48): 22871-22883.
- [26] Li Z, Wei J, Ren J, et al. *Carbon*, 2019, 154: 410-419.
- [27] Wu H, Guo Z, Li M, et al. *Electrochimica Acta*, 2021, 370: 137758.
- [28] Abdollahifar M, Huang S S, Lin Y H, et al. *Journal of Power Sources*, 2018, 378: 90-97.
- [29] Sannasi V, Subbian K. *Ceramics International*, 2021, 47(9): 12300-12309.
- [30] Nagamuthu S, Vijayakumar S, Lee S H, et al. *Applied Surface Science*, 2016, 390: 202-208.
- [31] Jayakumar A, Antony R P, Wang R, et al. *Small*, 2017, 13(11): 1603102.
- [32] Chen C, Yu W, Liu T, et al. *Solar Energy Materials and Solar Cells*, 2017, 160: 43-53.
- [33] Chen C, Liu X, Fang Q, et al. *Vacuum*, 2020, 174: 109198.
- [34] Duan J, Zhu C, Du Y, et al. *Journal of Materials Science*, 2017, 52(17): 10470-10479.
- [35] Zhou W, Lei S, Sun S, et al. *Journal of Power Sources*, 2018, 402: 203-212.
- [36] Li Z, Bu F, Wei J, et al. *Nanoscale*, 2018, 10(48): 22871-22883.
- [37] Yang J, Jo M R, Kang M, et al. *Carbon*, 2014, 73: 106-113.
- [38] Hussain S K, Yu J S. *Chemical Engineering Journal*, 2019, 361: 1030-1042.
- [39] Sim C K, Razali S A, Majid S R, et al. *Journal of Electronic Materials*, 2020, 49(2): 1024-1035.
- [40] Bhagwan J, Kumar N, Yadav K L, et al. *Solid State Ionics*, 2018, 321: 75-82.
- [41] Barkhordari H, Heydari H, Nosrati A, et al. *Ionics*, 2019, 25(1): 275-285.
- [42] Ameri B, Davarani S S H, Moazami H R, et al. *Journal of Alloys and Compounds*, 2017, 720: 408-416.
- [43] Fang Q, Chen C, Yang Z, et al. *Journal of Alloys and Compounds*, 2020, 826: 154084.
- [44] Huang T, Zhao C, Qiu Z, et al. *Ionics*, 2017, 23(1): 139-146.

CHAPTER 6 Other work

Facile synthesis of boron nitride quantum dots doped ZnO nanoparticle photocatalyst with efficiently enhanced photocatalytic degradation of methylene blue and methyl orange

6.1 Introduction

At present, organic dyes are widely used in many fields, and the dye wastewater produced contains a large number of toxicity and refractory organic pollutants, which caused serious pollution to the water ecosystem[1,2]. The dyes can last for a long time in environment, and its potential toxicity needs to be solved urgently. Many methods include physical adsorption, biodegradation, membrane and photocatalysis have been explored to treat dye wastewater[3-6]. Among these methods, photocatalytic degradation is a preferred approach, because of their high degradation efficiencies, low-cost, easy preparation of catalysts and no secondary pollution[7,8].

Various systems were used in photocatalytic degradation of dyes with different success, but semiconductors are among the most researched and employed due to their high efficiencies and environmentally friendliness. Zinc oxide (ZnO) with a wide band gap (3.37eV) as a II-VI semiconductor is a high-efficiency photocatalyst for the degradation of organic pollutants due to its nontoxic, high abundance, low cost and excellent chemical and thermal stability characteristics[9,10]. However, ZnO photocatalytic efficiency is greatly hindered because of narrow light-absorption range and high recombination ratio of photoinduced electron-hole pairs [11].

Therefore, a plenty of efforts have been devoted towards solving these two problems such as the doping of ZnO with precious metal (Ag, Eu, Pt), g-C₃N₄, carbon, nitrogen, etc. to reducing the bandgap energy, which rendered them more photocatalytically active over a wide range of wavelengths (UV region to visible

region)[9,12-14]. For instance, Li Sun et al. synthesized nitrogen doped ZnO nanoparticles by one step controllable pyrolysis of zeolitic imidazolate framework-8 (Zif-8) precursors under 550°C. The photocatalytic degradation rate to methylene blue reaches 95.3% after 80 min, which is much higher than that of commercial ZnO (66.9%)[15]. Raji Atchudan et al. synthesized the ZnO@N-C hybrid composite composed of ZnO NPs-decorated nitrogen-doped graphitic-carbon sheets. The homogenous distribution of ZnO NPs on the nitrogen-doped graphitic-carbon promotes the photocatalytic activity. The nitrogen-doped graphitic carbon layers increased light absorption as well as the reduced charge recombination it enhances the photocatalytic efficiency[16]. Sindhya et al. fabricated ZnO/g-C₃N₄/Ag composites via a homemade automated jet nebulizer spray technique and the ZnO/g-C₃N₄/Ag thin film causes 96 and 99% decomposition of Methylene Blue (MB) and Malachite Green (MG) dye molecules, respectively [17].

Besides these carbon and nitrogen doping, boron nitride has been widely investigated to elevate the photocatalytic activity. Hexagonal boron nitride, known as “white graphene”, possesses some special properties including good optical characteristics, low toxicity, high chemical and thermal conductivity and great charge transfer ability, and it has attracted rising attention in recent years[18-21]. Up to now, there're little kinds of ZnO based boron nitride photocatalysts, Sundar Mayavan's team[22] developed the ZnO-containing porous boron nitride sheets as a new class of sunlight-driven photocatalyst. They also applied this materials for oxygen reduction reaction and degradation of methyl orange dye under UV irradiation, which indicating that boron nitride have a great potential in photocatalysis. Furthermore, with the size of boron nitride shrinking to the quantum dots level, the edge effects and defect centers appear on the boron nitride quantum dots, which endow them with fascinating fluorescence properties and excellent dispersibility. Yang yang et al[23] synthesized boron nitride quantum dots (BNQDs) decorated ultrathin porous g-C₃N₄ for promoting visible-light-driven molecular oxygen activation, the results showed that the negatively charged groups on the BNQDs will attract the photo-excited holes, and thus promote the dissociation efficiency of excitons and boost the separation of charges. However, to the best of our knowledge, the investigation about the BNQDs doping with ZnO for

organic dyes degradation is still limited.

In this paper, we present a facile method to synthesize a novel metal-free boron nitride quantum dots decorated ZnO nanoparticles (ZnO-BN) with enhanced photocatalytic activity for photocatalytic degradation of methylene blue (MB) and methyl orange (MO) in water. The enhanced photocatalytic efficiency of ZnO-BN nanohybrids is attributed to the presence of BN quantum dots which play a key role in reducing the band gap energy of ZnO and inhibiting the recombination of photoexcited charge carrier. In addition, after five recycle experiments, the as-prepared BNQDs doped ZnO can still maintain a high efficiency degradation capacity.

6.2 Experimental

6.2.1 Materials

Zinc Acetate dihydrate ($\text{Zn}(\text{CH}_3\text{COO})_2 \cdot 2\text{H}_2\text{O}$), Potassium hydroxide (KOH), boric acid, melamine, anhydrous ethanol, methylene blue (MB), methyl orange (MO), isopropyl alcohol (IPA), and ethylene diamine tetraacetic acid (EDTA) and p-benzoquinone (BQ) were all commercial analytical grade reagents and used as received without any further treatment or purification.

6.2.2 Preparation of ZnO nanoparticles

The synthesis procedure of ZnO nanoparticle is given as follows. First, 5.2g zinc acetate dehydrate [$\text{Zn}(\text{CH}_3\text{COO})_2 \cdot 2\text{H}_2\text{O}$] was dissolved in 200 ml deionized water heated at 65°C under constant stirring. Simultaneously, 100 ml potassium hydroxide (KOH) solution (0.5M) was added drop wise with this zinc acetate dihydrate solution under vigorous stirring (1200 rpm) at 65°C. This mixtures solution was stirred continuously at 65°C for 1 h to achieve the white colored milky suspension. Then the product was centrifuged several times in ethanol for filtration and dried at 100°C for 2h in oven.

6.2.3 Preparation of boron nitride quantum dots

The boron nitride quantum dots were synthesized through a facile hydrothermal procedure. In detail, 100mg boric acid was dissolved in 10ml deionized water, and then 34 mg melamine was added to the boric acid solution under stirring. After stirring for 20min, the suspension was transferred into a Teflon-lined autoclave and kept at 200°C for 15h. After cooling to room temperature, the product was filtered with ultra filtration membrane (0.22 μm) to remove large particles, finally the BNQDs solution is obtained.

6.2.4 Preparation of ZnO-BN photocatalysts

The ZnO-BN photocatalysts were prepared as follows. Firstly, 0.300 g of ZnO was uniformly dispersed in 50 mL of ethanol and sonicated for 60 min. Subsequently, a certain volume of BNQDs solution was added dropwise to the above suspension and stirred for 24 h. Finally, after ethanol was completely vaporized, the BU photocatalysts were collected and dried in a vacuum oven at 70 °C. ZnO photocatalysts with different BNQDs content designated as ZnO-xBN, where “x” denote as the added volume of BNQDs solution (X = 1, 2, 4, 6 mL).

6.2.5 Characterization

X-ray diffraction (XRD) measurement was performed using a Bruker D8 Advance diffractometer with a non-monochromated Cu K α operated at 40 kV and 30 mA. The morphology and mapping was collected on a field-emission scanning electron microscope (FE-SEM, JEOL-JSM820) with energy-disperse X-ray spectroscopy (EDS). Transmission electron microscope (TEM) test was carried out on a Hitachi, H-8100 electron microscope at an accelerating voltage of 200 kV. X-ray photoelectron spectroscopy (XPS: Thermo Fisher) measurements were performed using monochromatic AlK α radiation ($h\nu = 1486.6$ eV). Fourier transform infrared (FTIR) spectra were collected on a Thermal Fisher Nicolet iS5 spectrometer using samples embedded in potassium bromide (KBr) pellets. Ultraviolet visible (UV-vis) diffuse reflectance spectra were recorded on Specord-210-Plus spectrophotometer. The

photoluminescence (PL) spectra of the nanoparticles were recorded on a Agilent Technologies PCB-1500 spectrophotometer at the 330nm excitation wavelength. The zeta potential measurements were performed by Malvern Instruments ZEN3600.

6.2.6 Photocatalytic activity measurement

The photocatalytic activities of photocatalysts were examined by MB or MO degradation experiments under UV light irradiation. Four Sigma BLB (black light bulb) lamp (20 W, $\lambda = 315-400$ nm) was employed as the UV light source. In a typical photocatalytic degradation experiment, 50 mg of photocatalyst powders were added into a 50 mL aqueous solution of MB or MO (10 mg/L). Before illumination, the suspension was magnetically stirred in dark for 1 h to obtain the adsorption/desorption equilibrium of MB or MO dye on the surface of the sample. Then the catalyst was exposed under the UV lamp. At a certain regular interval, 3 mL reaction solution was sampled every 10 min and a filter was used to separate catalysts and the solution of MB or MO concentrations were analysed with UV-visible spectroscopy. The absorption of the MB and MO peak was observed at 665 nm and 470nm respectively.

To further understand the photocatalytic mechanism, trapping experiments were conducted to determine the dominant reactive species involved in the photodegradation of MB or MO dye. EDTA (1 mM), BQ (1 mM), and IPA (1 mM) were selected as the scavengers for trapping holes (h^+), superoxide radical ($\cdot O_2$) and hydroxyl radical ($\cdot OH$) respectively. The experimental procedure was similar to the photodegradation of MB or MO experiments, except that 50ml of MB or MO solution was replaced by 50ml of mixture of the dye and scavenger.

6.3 Results and discussion

6.3.1 Characterization of the products

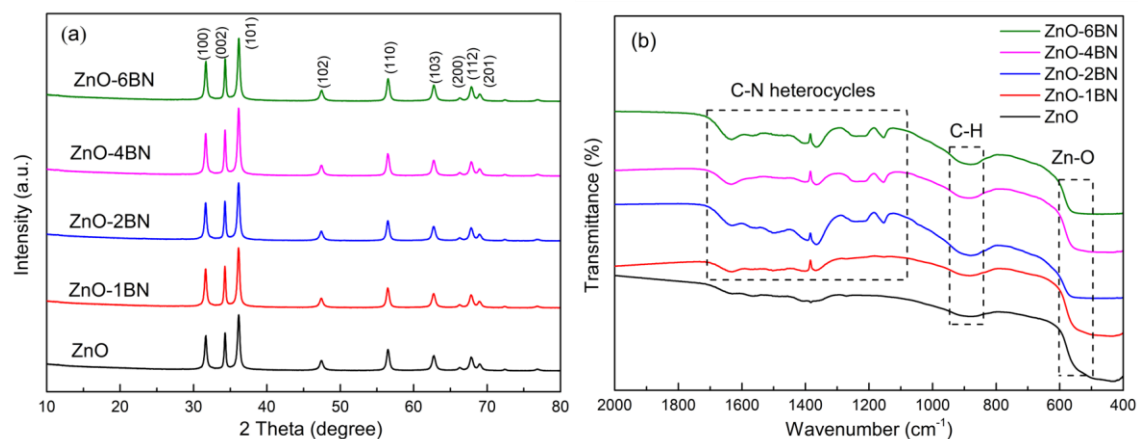


Fig.6-1. (a) XRD patterns and (b) FTIR spectra of the synthesized ZnO and ZnO-BN composites.

To clarify the crystal structure and chemical features of these samples, XRD and FTIR tests were performed. Fig.6-1a shows the typical XRD patterns of the ZnO nanoparticles and ZnO-BN composites with different BNQDs content. From the results, it can be seen that all of the indexed diffraction peaks of these samples are matched with ZnO (JCPDS NO. 36-1451), which confirms that the obtained ZnO has a wurtzite structure[16]. However, after the loading of BNQDs, no significant difference can be seen and no clear boron nitride peaks can be detected, because of the ZnO nanoparticles have a high crystallinity degree and low content of BNQDs.

Moreover, the direct evidence for the composition of the ZnO-BN composites was obtained by the FTIR spectra in Fig.6-1b. The samples all showed broad peaks at 580cm^{-1} and 890cm^{-1} , the peaks at 580cm^{-1} correspond to the stretching mode of ZnO. The peaks at 890cm^{-1} attributed to the stretching of the C-H band, which resulting from the precursor[24]. However, compared to ZnO, there's new group of peaks between $1100\text{-}1700\text{cm}^{-1}$ appeared in ZnO-BN composites, which is ascribed to the typical stretching vibration modes of the C-N heterocycles[23]. On the basis of the above FTIR results, it may be said that ZnO-BN hybrid structures are achieved.

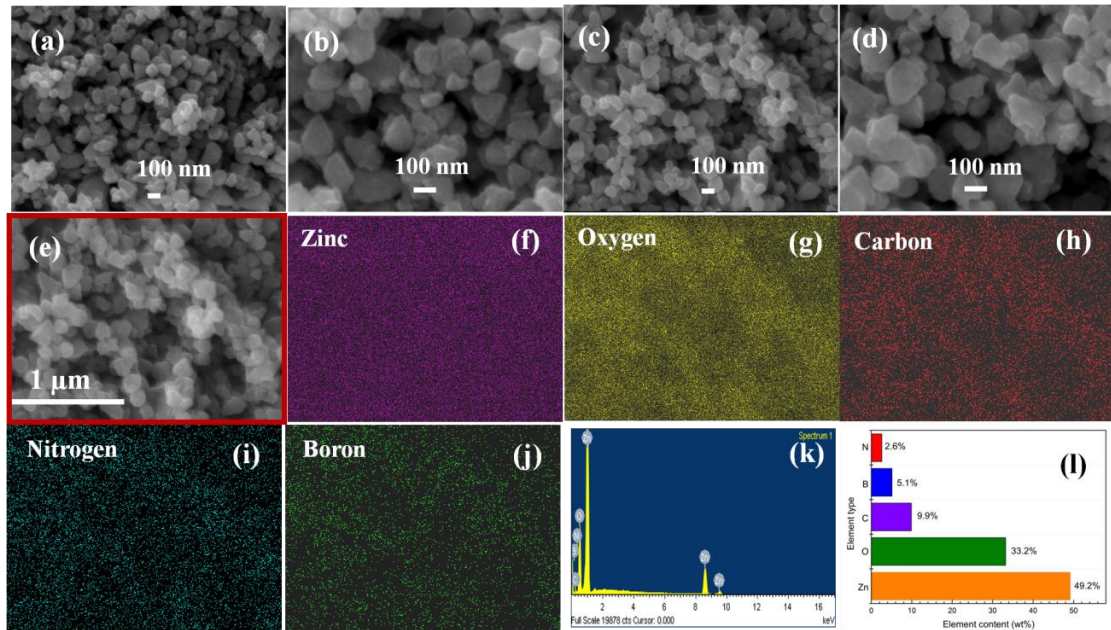


Fig.6-2. SEM images of ZnO nanoparticles (a,b), and ZnO-4BN composites (c,d); SEM image and elemental mapping for ZnO-4BN composites (e-j); EDS measurement of the plotted area and the elemental distribution of ZnO-4BN composites (k,l).

The surface morphology with elemental composition and structural morphology were assessed using FESEM with EDX element mapping. Fig.6-2(a,b) shows the morphology of ZnO nanoparticles, all the particles are uniform and average size is about 100nm. After doping with BNQDs, in Fig.6-2(c,d) it can be seen that the morphology of ZnO-BN has no change while compared with ZnO, because the size of BNQDs are so small that it can't be detected by FESEM. However, the BNQDs are evenly distributed on the ZnO which is further confirmed by the EDX mapping images. The FESEM image (Fig.6-2e) and the corresponding EDX mapping and evaluation are shown in (Fig.6-2f-k). It can be seen that Zn, O, N, C and B elements are evenly distributed in the ZnO-4BN composite, indicating that BNQDs have been successfully doped into ZnO.

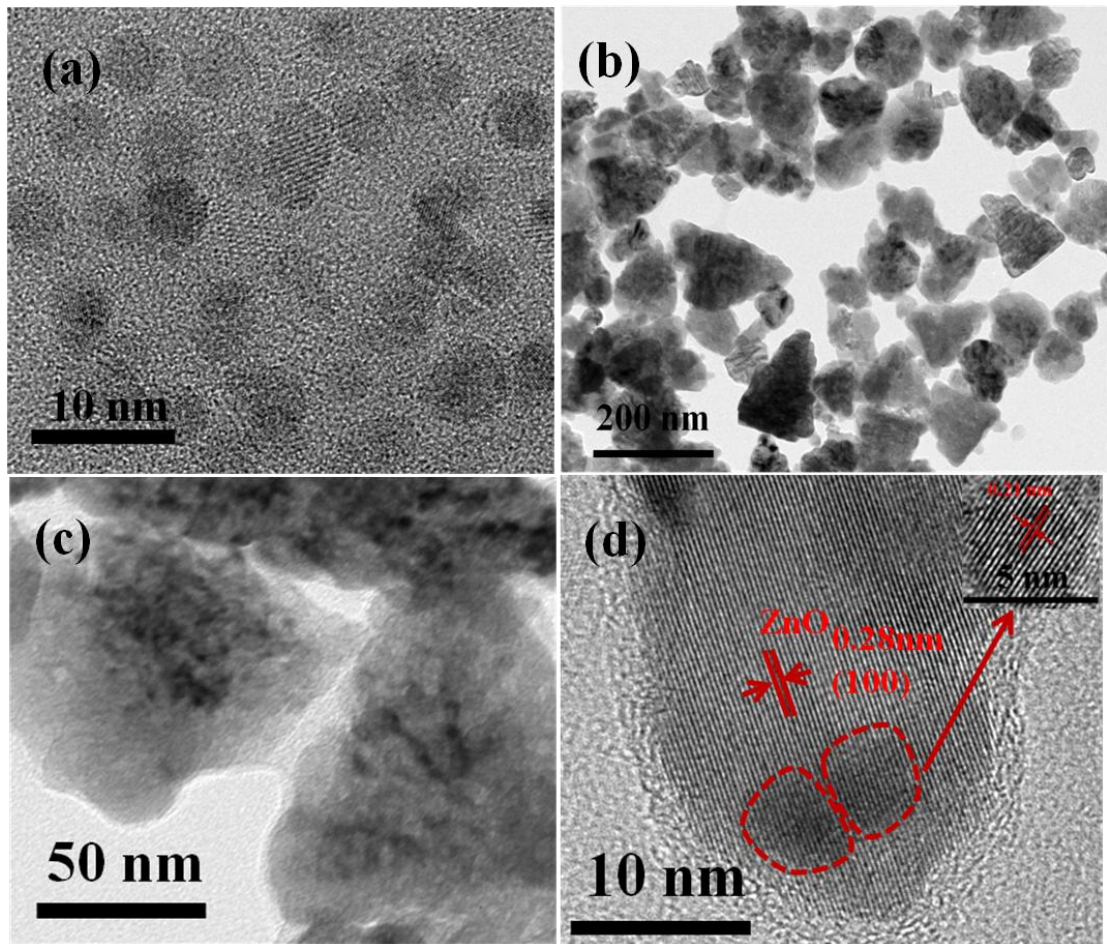


Fig.6-3. TEM images of BNQDs (a) and ZnO-4BN composites (b-d) (insert, HRTEM of BNQDs).

TEM images were collected for getting the direct information about morphology and structure of the samples. From Fig.3a, the prepared BNQDs are mainly distributed in 4-6nm with the average lateral size of about 5nm. In Fig.6-3b-c, there're some dark dots can be directly observed on ZnO nanoparticles in the ZnO-BN composites and ZnO has similar triangle shapes in accordance with the morphology in FESEM (Fig.6-2c-d). The high resolution TEM (HRTEM) image of ZnO-BN further reveals the presence of BNQDs. As exhibited in the insert of Fig.3d, the dark dot from ZnO-4BN sample has an obvious lattice fringes of 0.21nm, which is in coincidence with the (100) facet of BN. Meanwhile, it's also can be clearly seen that the composites showed lattice fringes of 0.28nm, which in consistent with the (100) facet of ZnO. These results clearly state the hybridization of BNQDs with ZnO nanoparticles for ZnO-BN sample.

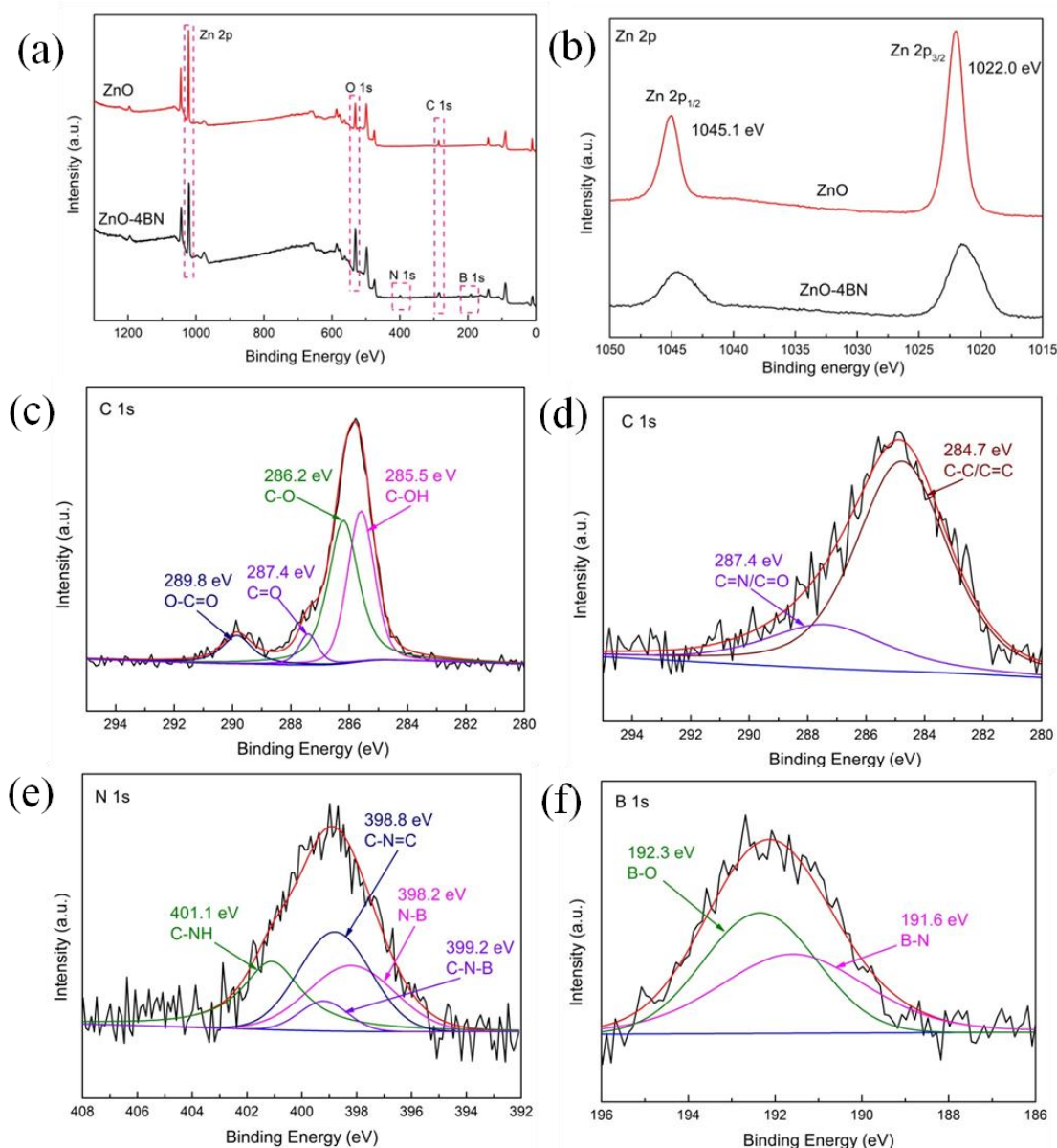


Fig.6-4. XPS spectra of ZnO and ZnO-4BN samples: (a) total survey, (b) Zn 2p, (c) C1s of ZnO, (d) C1s of ZnO-4BN, (e) N 1s of ZnO-4BN and (f) B 1s of ZnO-4BN.

The chemical composition of ZnO and ZnO-4BN was studied by XPS analysis, is presented in Fig.6-4. The XPS survey spectrum was shown in Fig.6-4a, three elements of Zn, O, and C are detected in ZnO while two additional elements of B and N are found in the ZnO-4BN sample. To get detailed chemical states information, the high-resolution XPS spectra of Zn 2p, C 1s, N 1s and B 1s were recorded. The analysis of the Zn 2p photoelectron spectra revealed presence of Zn $2p^{3/2}$ and Zn $2p^{1/2}$ peaks located at 1022.0 eV and 1045.1 eV respectively. The peak at 1022.0 eV is characteristic of Zn²⁺ ion in an oxide environment[25]. For C1s of ZnO, as illustrated in

Fig.6-4c, four peaks at the binding energies of 285.5 eV, 286.2 eV, 287.4 eV and 289.8 eV can be seen, they can be ascribed to C-OH, C-O, C=O and O-C=O band respectively[26]. However, the C 1s of ZnO-4BN is shown in Fig.6-4d, the peak appeared at 284.7 eV and 287.4 eV are corresponding to sp²-hybridized carbon (C-C/C=C) and C=N/C=O band respectively, while the peaks at 285.5 eV, 286.2 eV and 289.8 eV disappeared. Additionally, the N 1s spectrum in Fig.6-4e can be divided into three peaks at 398.2 eV, 398.8 eV, 399.2 eV and 401.1 eV, which are assigned to the N-B, C-N=C, C-N-B and C-NH bonds respectively [23]. In Fig.6-4f, the B 1s spectrum of ZnO-4BN has two strong peaks at 191.6 eV and 192.3 eV which are characteristic signal for the B-N and B-O stretching vibration respectively [18]. Therefore, combining with the mentioned above results, it can be concluded that the successful preparation of ZnO-BN photocatalysts.

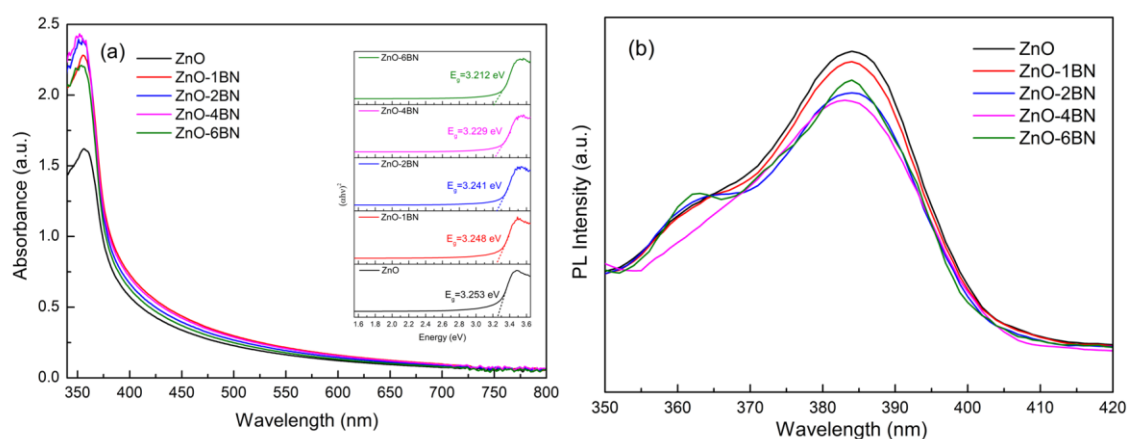


Fig.6-5. (a) UV-vis and (b) PL spectra of ZnO and ZnO-BN composites with different fluencies. The insert picture displays the corresponding $(\alpha h\nu)^2$ versus $h\nu$ plots.

Fig.6-5a represents the UV-vis spectra of ZnO and ZnO-BN composites. It can be found that the pure ZnO possesses absorption wavelength from the UV to the visible light region which can up to about 400nm, with the adding of BNQDs, the absorbance in the visible light gradually increased. However, compared with ZnO, the adsorption edge of ZnO-BN samples except ZnO-1BN (because of the low content of BNQDs) shows somewhat blue-shift due to the existence of BNQDs, but they still hold distinct UV light absorption. The strong absorption intensity in UV and visible light region for ZnO-BN composites is a key factor for good photocatalytic performance. The band gap of the synthesized samples was also estimated by applying the Kubelka-Munk function,

the band gap energies of ZnO (~3.253 eV), ZnO-1BN (~3.248 eV), ZnO-2BN (~3.241 eV), ZnO-4BN (~3.229 eV) and ZnO-6BN (~3.212 eV) maybe extracted from their $(\alpha h\nu)^2$ versus $h\nu$ plots (in the insert picture in Fig.6-5a). These results further suggest that incorporation of BNQDs into ZnO nanoparticles doesn't strongly modify the band gap of the obtained catalysts.

The PL analysis usually can be used to estimate the photo induced charge carriers separation and transfer ability of the as-prepared photocatalysts. Fig.6-5b depicts the samples' PL emission spectra at an excitation wavelength of 330nm. It can be seen that ZnO exhibits the main emission peak at about 385nm and displays the highest PL intensity in compared with that of ZnO-BN composites. Compared to pure ZnO, the ZnO-BN samples show lower PL intensities when BNQDs modified with ZnO to form heterojunction, suggesting the recombination rate of photogenerated electron-hole pairs become lower. In addition, it can be seen that the ZnO-4BN sample possesses the lowest PL intensity, indicating its higher electron-hole pair's separation and demonstrating its best photocatalytic activity.

6.3.2 Evaluation of photocatalytic activity

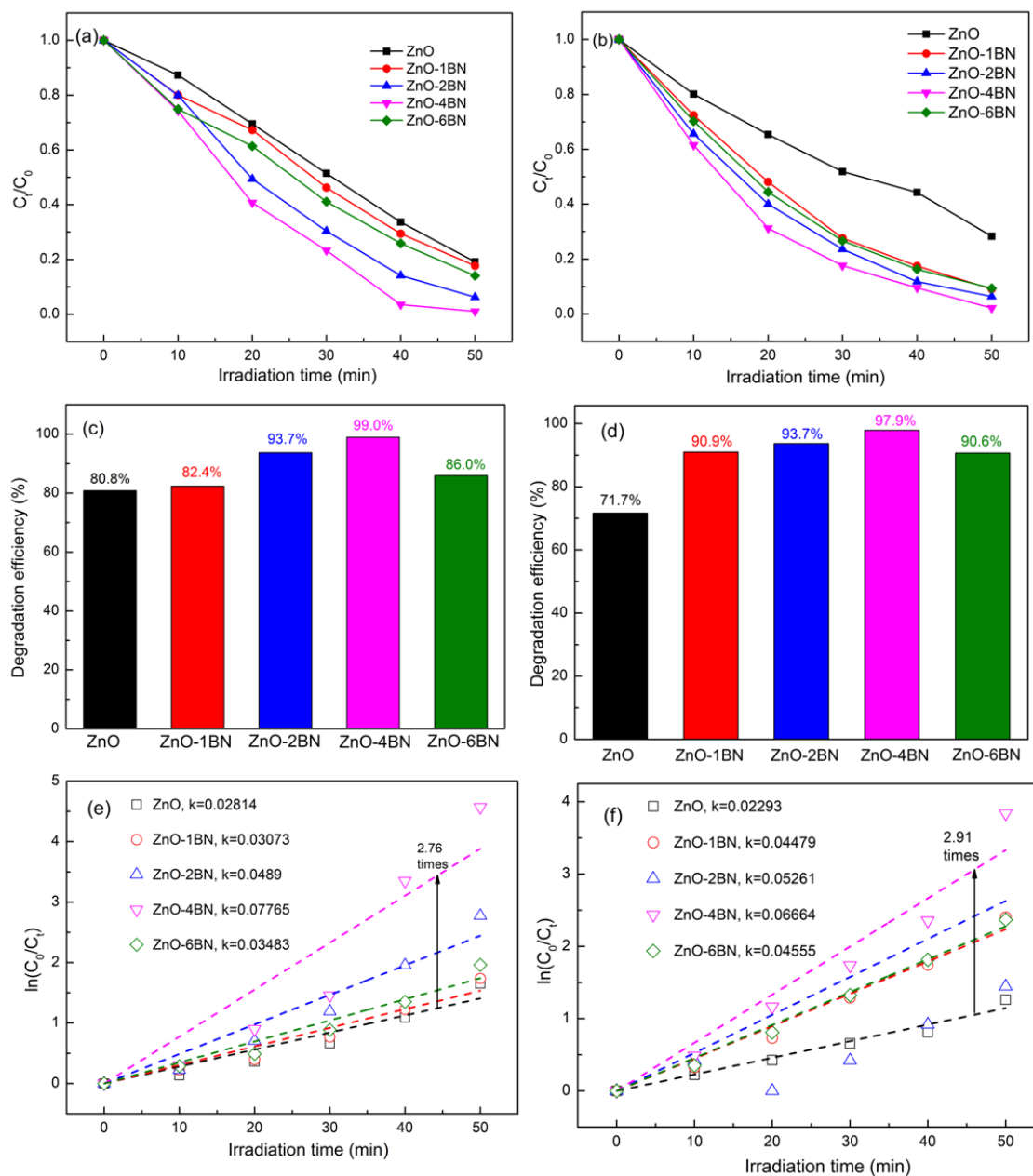


Fig.6-6. The photocatalytic activities of ZnO and ZnO-BN composites for degradation of (a) MB and (b) MO under UV light irradiation; Degradation efficiencies of (c) MB and (d) MO under UV light irradiation for different samples; Pseudo first-order kinetic fitting curves and the corresponding apparent rate constants for (e) MB and (f) MO degradation.

Methylene blue (MB) is the most common soluble dye in water that is generally applied for cotton, printing and tannin, medicinal purposes and dyeing leather. Methyl Orange (MO) is an acidic dye that used in pharmaceutical, textile, and paper industries. Therefore, reducing these dyes and turning them into harmless materials is great importance.

From the UV-vis results in Fig.6-5a, the strong absorption in the UV region confirms the UV light activity of the as-prepared samples. The photocatalytic efficiency of ZnO and ZnO-BN composites is evaluated by the photodegradation of MB and MO under UV light irradiation. Before the light irradiation, the adsorption property was firstly examined. Before the UV irradiation, the MB or MO solution with catalysts was stirred for 1h, the adsorption ability can be determined according to the UV-vis spectrum in Fig.6-7, It can be clearly seen that the adsorption ability of all catalysts keeps stable after 30min, indicating that the suspensions are adsorption-desorption equilibrium after 30min magnetic stirring.

Fig.6-6a and Fig.6-6b depicts the change in MB and MO concentration (C_t/C_0) with irradiation time over all samples under UV light irradiation respectively. The C_0 represents the concentration of MB or MO after reaching adsorption-desorption equilibrium, and the C_t refers to the concentration of MB or MO after time t of photocatalytic reaction. Meanwhile, the photocatalytic degradation efficiency (DE%) was calculated by the following equation and shown in Fig.6c and Fig.6d:

$$DE(\%) = (1 - C_t/C_0) \times 100\% \quad (1)$$

In Fig.6-6a and Fig.6-6c, it can be found that the pure ZnO exhibit relatively lower photocatalytic activity (80.8%) in degradation of MB. However, when BNQDs introduced into ZnO nanoparticles, the ZnO-BN photocatalysts can be significantly enhanced their photocatalytic activities. After irradiated for 50min, 82.4%, 93.7%, 99.0% and 86.0% of MB were photodegraded with increasing the BNQDs content from 1ml to 6ml, respectively. In addition, the ZnO-4BN sample displays the highest MB degradation rate. On the other hand, Fig.6-6b and d depicts the photocatalytic activity of as-prepared samples for degradation of MO under UV light. It can be observed that the pure ZnO exhibits poor activity (71.7%) in MO degradation. On the contrary, the as-prepared ZnO-BN samples can improve photocatalytic performance, which is

similar to the above MB degradation. After irradiation for 50min, 90.9%, 93.7%, 97.9% and 90.6% of MO were photodegraded by using ZnO-1BN, ZnO-2BN, ZnO-4BN and ZnO-6BN composites, respectively. In addition, the ZnO-4BN sample exhibits the highest photocatalytic activity in MO degradation. Fig.6-8 displays the time-dependent UV-vis spectrum of MB and MO on the ZnO-4BN, it is apparent that the intensity of characteristic absorption peak at 665nm and 470nm respectively, which declines with the time prolongs. And Fig.6-9 presents the photographs of MB and MO aqueous solution in the presence of ZnO (a) and ZnO-4BN (b) depends on irradiation time. Nevertheless, the photocatalytic performance of ZnO-BN decreases when the BNQDs exceed the optimal proportion, indicating that the presence of more BNQDs in this nanocomposites does not necessarily obtain the best photocatalytic performance because excessive BNQDs will depress electron-hole pair's separation and demonstrating lower photocatalytic activity, these results are in agreement with the PL measurement shown in Fig.6-5b. Therefore, these results suggest that the ZnO-BN photocatalyst not only can efficiently degrade MB, but also can decompose colorless MO under UV light, which can be a good candidate for application in environmental purification.

The apparent rate constant (k) for the degradation of MB and MO was further assessed by the following equation:

$$k = \frac{\ln(C_0/C_t)}{t} \quad (2)$$

As displayed in Fig.6-6e, the plots of $\ln(C_0/C_t)$ versus t are found to be a linear relationship, clarifying that the reaction of MB photocatalytic degradation is in coincidence with the pseudo-first-order model. From the kinetic curves, the k value conforms the order: ZnO-4BN (0.07765 min^{-1}) > ZnO-2BN (0.04890 min^{-1}) > ZnO-6BN (0.03483 min^{-1}) > ZnO-1BN (0.03073 min^{-1}) > ZnO (0.02814 min^{-1}). The ZnO-4BN photocatalyst presents the highest apparent rate constant of 0.07765 min^{-1} , which is 2.76 times than that of pure ZnO. On the other hand, Fig.6-6f also displays the kinetic behaviors of ZnO and ZnO-BN samples for photodegradation of MO. It can be seen that the pseudo-first-order reaction kinetic model fitted the experimental data are also very well with the pseudo-first order correlation. It can be clearly observed that all of the ZnO-BN composites exhibit higher apparent rate constant than that of ZnO. The

optimal photocatalyst is ZnO-4BN according to its photocatalytic activity, which is similar to the result of MB degradation. The k value for MO degradation over ZnO-4BN sample (0.06664 min^{-1}) is about 2.91-fold higher than that of ZnO (0.02293 min^{-1}). Thus, the as-prepared ZnO-BN composites could significantly enhance UV-light-driven photocatalytic activity under UV light irradiation.

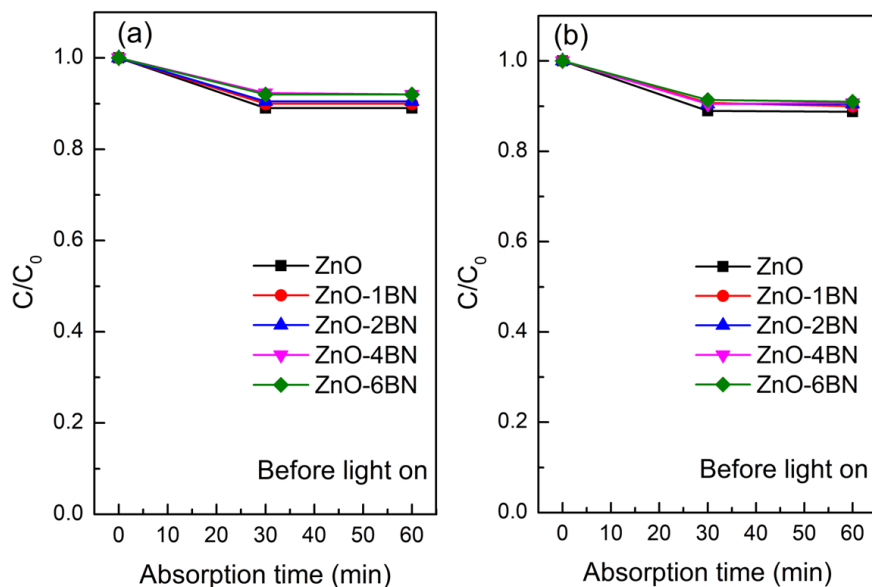


Fig.6-7. Adsorption properties of the synthesized photocatalysts for MB (a) and MO (b) degradation in the dark respectively.

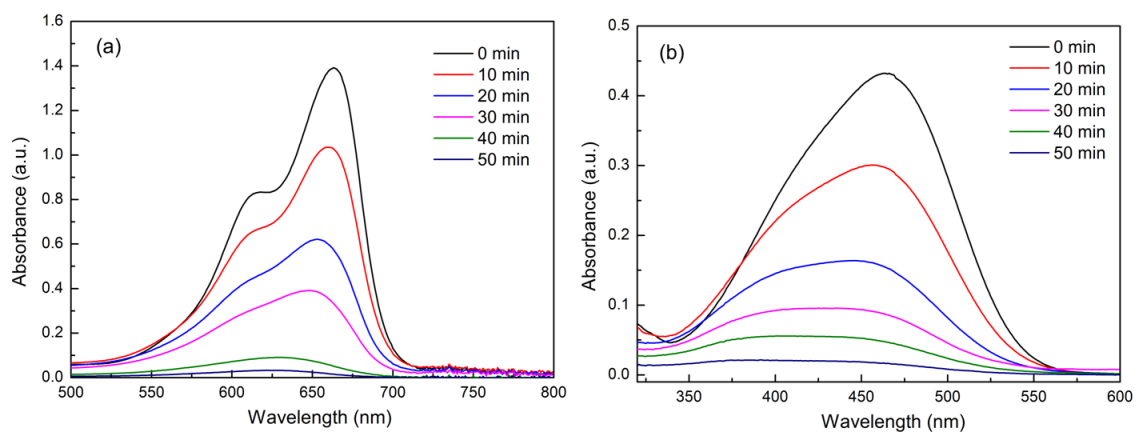


Fig.6-8. UV-vis spectra of MB (a) and MO (b) degradation in the presence of ZnO-4BN composite depends on irradiation time.

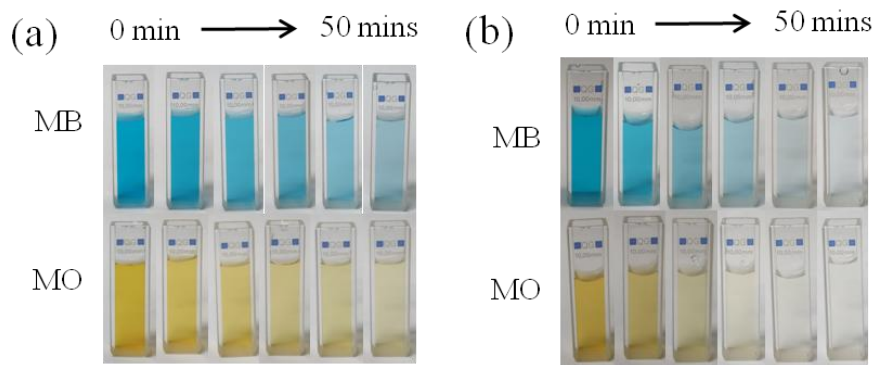


Fig.6-9. photographs of MB and MO aqueous solution in the presence of ZnO (a) and ZnO-4BN (b) depends on irradiation time

For comparison, Table.6-1 and Table.6-2 lists the kinetic data of the degradation of MB and MO by the various reported modified ZnO photocatalysts, respectively. It can be concluded that ZnO-4BN has a competitive photocatalytic degradation activity.

Table.6-1. Photocatalytic degradation of MB with modified ZnO composites under UV light irradiation.

Sample	Catalyst dosage(g/L)	Degrade d material	Light source	Irradiation time	Final MB degradation(%)	Rate Constant (min ⁻¹)	reference
N-doped ZnO/C ₃ N ₄	0.5 g/L	10 mg/L	300W Xe lamp	100 min	90%	0.0299	[9]
Ag-ZnO	0.6 g/L	10 mg/L	UV lamp,6W	60 min	87.74%	0.032	[10]
ZnO-Eu	1 g/L	10 mg/L	300W Osram vitalux lamp	150 min	90%	-	[12]
N-ZnO/C ₃ N ₄	1 g/L	20 mg/L	300W Xe lamp	90 min	95%	0.030	[14]
AgBr/g-C ₃ N ₄ /ZnO	0.4 g/L	5 mg/L	300W Xe lamp	80 min	96.3%	0.041	[27]

N self doped ZnO	0.5 g/L	20 mg/L	200W Xe lamp	80 min	95.3%	0.040	[11]
ZnO-4BN	1 g/L	10 mg/L	Sigma 20W/4 BLB	40 min	96.4%	0.0776	This work

Table.6-2. Photocatalytic degradation of MO with modified ZnO composites under UV light irradiation.

Sample	Catalyst dosage(g /L)	Degraded material	Light source	Irradiation time	Final MO degradation(%)	Rate Constant (min ⁻¹)	reference
ZnO-Eu	1 g/L	10 mg/L	300 W Osram vitalux lamp	60 min	95%	-	[12]
Graphene / ZnO	0.5 g/L	13 mg/L	Natural sunlight	150 min	100%	0.035	[28]
Ag-N-ZnO	0.2 g/L	30 mg/L	500 W Xe lamp	120 min	98.82%	0.026	[29]
ZnO/SnO ₂	0.2 g/L	20 mg/L	300 W Hg lamp	100 min	56%	-	[30]
Cu-TiO ₂ /ZnO	1 g/L	15 mg/L	500 W Xe lamp	60 min	83%	0.0306	[31]
ZnO/g-C ₃ N ₄	2.5 g/L	10 ⁻⁵ mol/L	500 W Xe lamp	120 min	Nearly 98%	0.136	[32]
ZnO-4BN	1 g/L	10mg/L	Sigma 20W/4 BLB	50min	97.9%	0.0666	This work

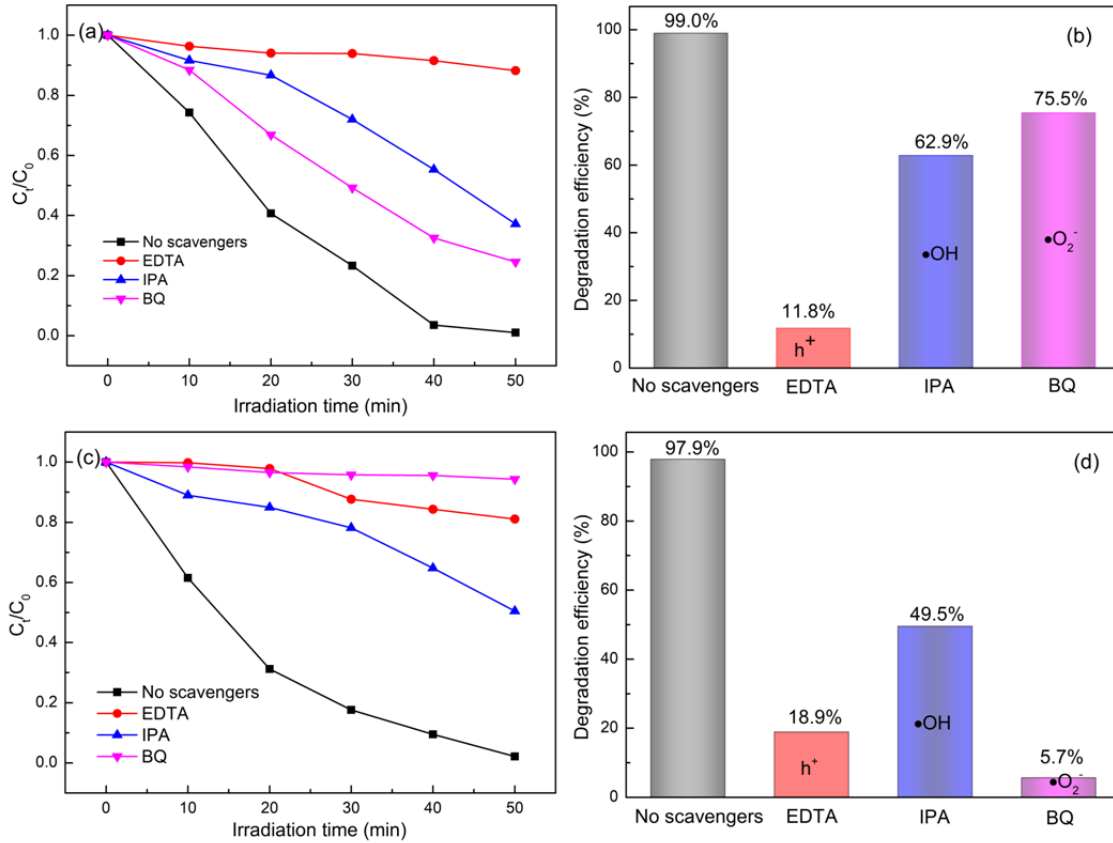


Fig.6-10. The species trapping experiment for degradation curve and efficiencies of MB (a,b) and MO (c,d) over ZnO-4BN sample under UV light irradiation.

Fig.6-10 depicts the different active species trapping experiments for MB and MO degradation over ZnO-4BN sample under UV-light irradiation. Herein, EDTA, IPA and BQ were employed as the scavengers of h^+ , $\bullet OH$ and $\bullet O_2^-$, respectively[15]. For MB, the degradation curve and efficiencies are shown in Fig.6-10a and 6-10b respectively, it can be seen that when BQ and IPA were added, the degradation efficiency of MB distinctly decrease from 99% to 75.5% and to 62.9% respectively. However, the presence of EDTA remarkably reduces the degradation efficiency of MB from 99% to 11.8%. These results indicating that h^+ play a very important role in MB degradation while $\bullet O_2^-$ and $\bullet OH$ also play inconvenient role. For MO, as shown in Fig.6-10c and 6-10d, it can be found that when IPA added, the photodegradation efficiency of MO was obviously inhibited from 97.9% to 49.5%. What's more, the efficiency significantly decreased from 97.95 to 18.9% and to 5.7% when EDTA and BQ were added, respectively. It suggests that these three active species (h^+ , $\bullet OH$ and $\bullet O_2^-$) all played important role in MO degradation. Therefore, the results also suggest that h^+ and $\bullet OH$

are the major reactive species for organic pollutants photocatalytic degradation in the ZnO-BN heterojunction system, and the MO photodegradation is driven by the O_2^- radicals from ZnO-BN under UV-light irradiation.

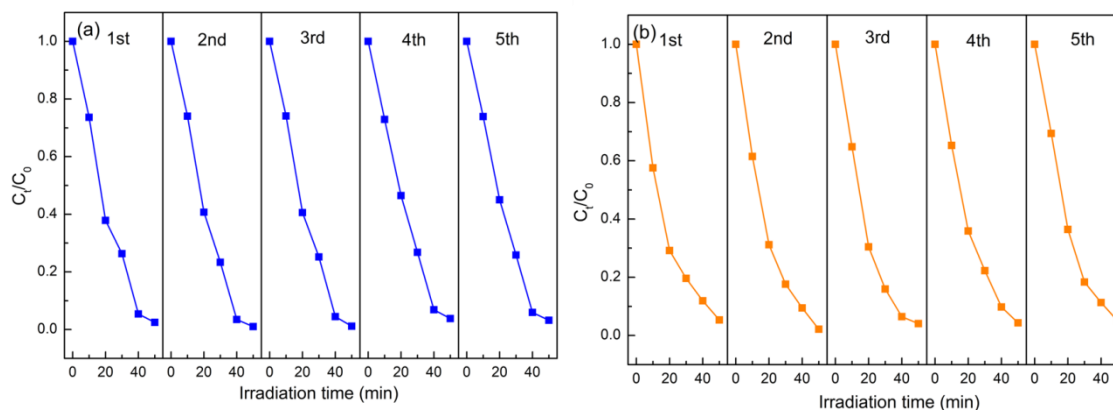


Fig.6-11. The recycled photocatalytic experiments of ZnO-4BN sample for degradation of MB (a) and MO (b) under UV light irradiation.

The photocatalytic reusability and repeated performance of the as-prepared ZnO-4BN sample was also studied by the circulation photocatalytic degradation of MB and MO under UV-light irradiation. From Fig.6-11, it can be observed that ZnO-4BN sample exhibits the barely changing photocatalytic degradation activity even after 5th successive recycles for the degradation of MB (Fig.6-11a) and MO (Fig.6-11b) under UV-light, which suggests that our photocatalyst possesses high stability for its practical application.

6.3.3 Mechanism of photocatalytic degradation

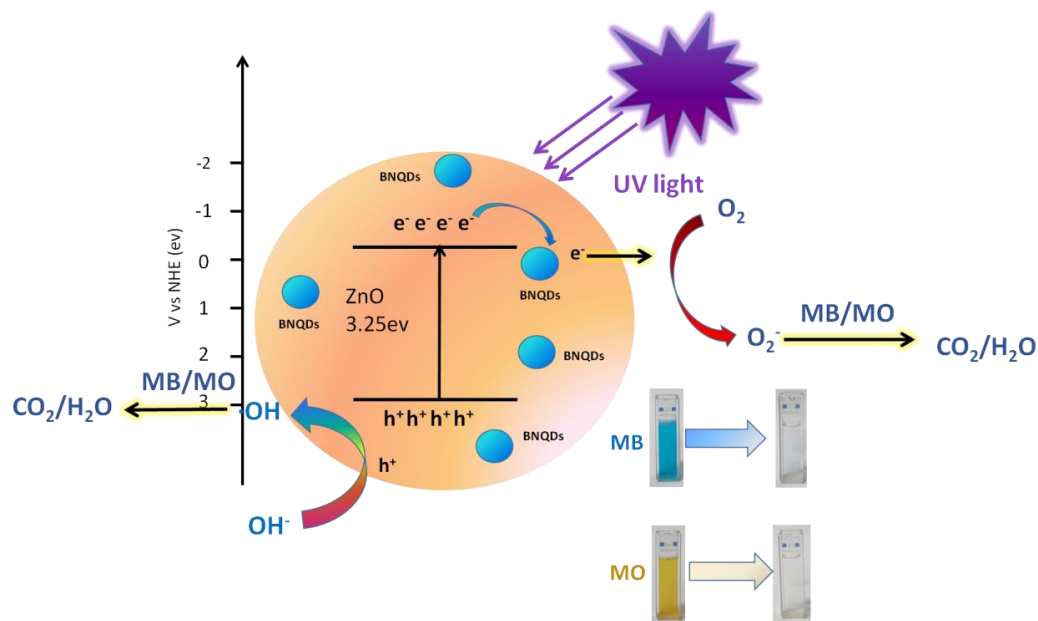


Fig.6-12. Schematic illustration of the possible photocatalytic processes in ZnO-BN of MB and MO degradation.

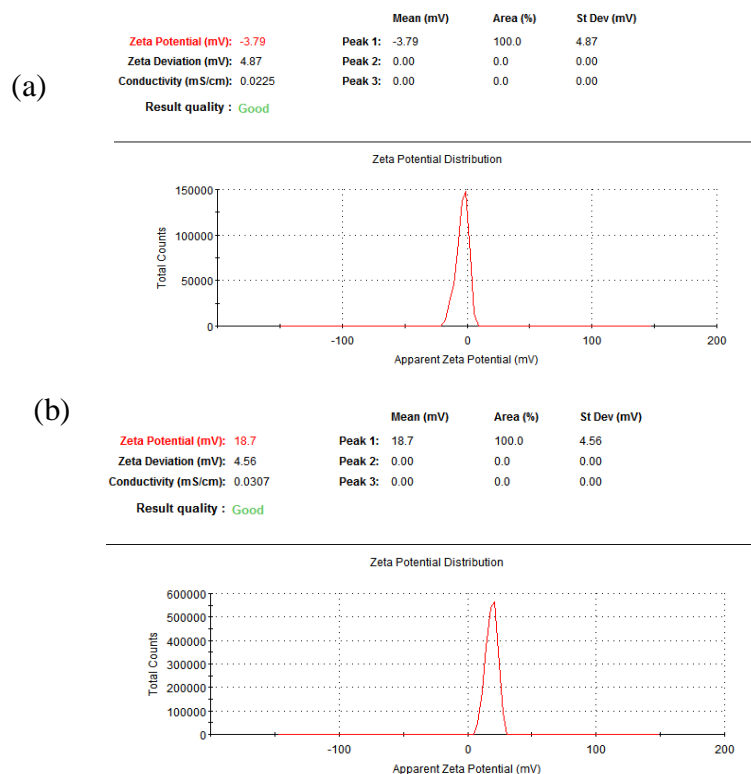
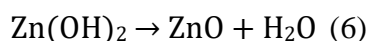
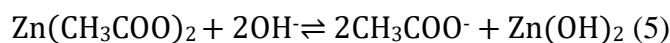
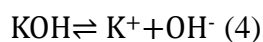
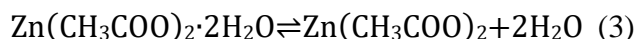
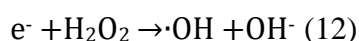
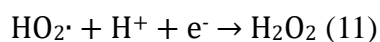
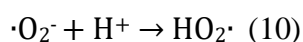
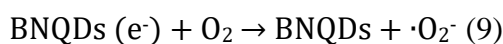
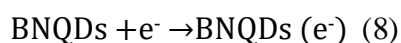
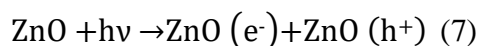


Fig.6-13. zeta-potential of BNQDs (a) and ZnO (b) dispersed in 10 ml (10 mg) of ethanol with sonication 20 minutes.

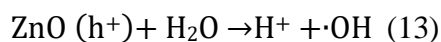
ZnO nanoparticles were synthesized via a modified precipitation method. The likely reaction mechanism leading to ZnO nanoparticles is presented as follows:



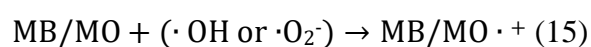
After BNQDs were added into ZnO, there's a electric effect between ZnO and BNQDs in the solvent evaporation process, because they showed opposite electric properties (the zeta potential test was shown in Fig.6-13.). And there's a synergetic effect between ZnO and BNQDs on the photocatalytic degradation of MB/MO, the proposed photocatalytic mechanism for the catalytic degradation of MB/MO dyes by as-prepared ZnO-BN is shown in Fig.6-12. The figure also displays the MB/MO solution before (0 min) and after (50min) the UV-light irradiation, the blue color or the orange color of the solution disappeared. When the UV light irradiates the ZnO, electron-hole pairs are created on the catalytic surface, the electrons excited to conductive band and the hole is created in the valence band. After charges are separated, the electron can diffuse toward the surface with or without recombination hole. What's more, fast recombination of exciton can drastically decrease photocatalytical efficiency. With BNQDs doping, the electron is trapped to it and is inhibited to recombine with hole, then electrons can react with adsorbate O_2 creating super oxide radicals (O_2^-). Next, the superoxide anion reacts with H^+ to generate first HO_2^- radicals, which react with to H^+ produce hydrogen peroxide molecules. The hydrogen peroxide molecules prompt the formation of additional hydroxyl radicals. The reaction process can be described as follows:



At the same time, photogenerated hole in the valence band is trapped by surface hydroxyl group or reacted with adsorbed water, creating highly reactive hydroxyl radical ($\cdot\text{OH}$):



The photogenerated radicals oxidize organic pollutants such as MB/MO in an oxidation process that continues until organic pollutants are entirely oxidized, which involves the formation of some intermediate, and intermediates are self degraded or they are degraded by reactive oxidative species (ROS) to final products:



Therefore, the enhanced photocatalytic performance of ZnO-BN composites can be attributed to the improved photogenerated electron-hole pair's separation and the harvesting ability of UV-light.

6.4 Conclusion

In summary, the ZnO-BN heterojunction photocatalyst were successfully synthesized by a facile method. The photocatalytic activity of ZnO nanoparticles could be greatly improved by introducing BNQDs into the ZnO. The loading content of BNQDs also play a key role in the photocatalytic activity of ZnO-BN heterojunctions. The ZnO-4BN displays the highest photocatalytic efficiency under UV light irradiation. In addition, the as-prepared samples exhibited efficient and stable UV-light-driven photocatalytic performance in degradation of organic dyes, which could be used as a candidate for application in environmental renovation.

6.5 References

- [1] Nuengmatcha P, Chanthai S, Mahachai R, et al. *Dyes and Pigments*, 2016, 134: 487-497.
- [2] Portillo-Vázquez N S, Hernández-Gordillo A, Bizarro M. *Catalysis Today*, 2017, 287: 106-112.

- [3] Li Q, Xue D X, Zhang Y F, et al. *Inorganic Chemistry Communications*, 2017, 85: 78-83.
- [4] Shi Y, Yang D, Li Y, et al. *Applied Surface Science*, 2017, 426: 622-629.
- [5] Chen S H, Cheow Y L, Ng S L, et al. *International Journal of Environmental Research*, 2019, 13(2): 273-282.
- [6] Vaiano V, Matarangolo M, Sacco O, et al. *Applied Catalysis B: Environmental*, 2017, 209: 621-630.
- [7] Zhang L, Zhang Q, Xie H, et al. *Applied Catalysis B: Environmental*, 2017, 201: 470-478.
- [8] Nguyen C H, Tran M L, Van Tran T T, et al. *Separation and Purification Technology*, 2020, 232: 115962.
- [9] Balcha A, Yadav O P, Dey T. *Environmental Science and Pollution Research*, 2016, 23(24): 25485-25493.
- [10] Rafaie H A, Nor R M, Azmina M S, et al. *Journal of environmental chemical engineering*, 2017, 5(4): 3963-3972.
- [11] Sun L, Shao Q, Zhang Y, et al. *Journal of Colloid and Interface Science*, 2020, 565: 142-155.
- [12] Trandafilović L V, Jovanović D J, Zhang X, et al. *Applied Catalysis B: Environmental*, 2017, 203: 740-752.
- [13] Zayed M, Ahmed A M, Shaban M. *International Journal of Hydrogen Energy*, 2019, 44(33): 17630-17648.
- [14] Liu Y, Liu H, Zhou H, et al. *Applied Surface Science*, 2019, 466: 133-140.
- [15] Sun L, Shao Q, Zhang Y, et al. *Journal of Colloid and Interface Science*, 2020, 565: 142-155.
- [16] Atchudan R, Edison T N J I, Perumal S, et al. *Journal of Photochemistry and Photobiology A: Chemistry*, 2018, 350: 75-85.
- [17] K. Ravichandran, E. Sindhuja, *Mater. Chem. Phys.* 221 (2019) 203–215.
- [18] Huo B, Liu B, Chen T, et al. *Langmuir*, 2017, 33(40): 10673-10678.
- [19] Li Q, Zheng Y, Hou X, et al. *Sensors and Actuators B: Chemical*, 2020, 304: 127353.
- [20] Liu M, Xu Y, Wang Y, et al. *Advanced Optical Materials*, 2017, 5(3): 1600661.

- [21] Peng C, Xing H, Fan X, et al. *Analytical chemistry*, 2019, 91(9): 5762-5767.
- [22] Bharathidasan T, Mandalam A, Balasubramanian M, et al. *ACS applied materials & interfaces*, 2015, 7(33): 18450-18459.
- [23] Yang Y, Zhang C, Huang D, et al. *Applied Catalysis B: Environmental*, 2019, 245: 87-99.
- [24] Gharagozlou M, Naghibi S. *Materials Research Bulletin*, 2016, 84: 71-78.
- [25] Ranjith Kumar D, Ranjith K S, Haldorai Y, et al. *ACS omega*, 2019, 4(7): 11973-11979.
- [26] Zhang Y, Fan S, Li S, et al. *J Mater Sci* (2020) 55:12214–12231.
- [27] Azimi E B, Badiei A, Sadr M H. *Journal of Physics and Chemistry of Solids*, 2018, 122: 174-183.
- [28] Wang L, Li Z, Chen J, et al. *Environmental Pollution*, 2019, 249: 801-811.
- [29] Chen X, Wu Z, Gao Z, et al. *Nanomaterials*, 2017, 7(9): 258.
- [30] Ali W, Ullah H, Zada A, et al. *Materials Chemistry and Physics*, 2018, 213: 259-266.
- [31] Dorraj M, Alizadeh M, Sairi N A, et al. *Applied Surface Science*, 2017, 414: 251-261.
- [32] Guan R, Li J, Zhang J, et al. *ACS omega*, 2019, 4(24): 20742-20747.

CHAPTER 7 Summary and recommendations for future work

7.1 Summary

The transition metal compound (MnO_2 , MnCO_3 , ZnMn_2O_4), carbon materials (carbon nanofibers, carbon cloth, and graphene hydrogel) and quantum dots ($\text{g-C}_3\text{N}_4$, N-GQDs) were investigated as electrodes materials for energy storage application.

There are some general strategies for electrochemical performance enhancement, such as dimension reduction, morphology control, composite formation, doping and functionalization, coating and encapsulation and electrolyte modification. In this thesis, the strategies like morphology control, composite formation, doping and functionalization were employed for electrode materials preparation. The hierarchical hollow urchin-like MnO_2 structures are obtained by controlling the hydrothermal reaction time. For improving electrical conductivity, the u- MnO_2 /CNFs nanocomposite is prepared, which is beneficial for maximizing the utilization of hierarchical structures of u- MnO_2 . When used as anode electrode of a Li-ion battery, the u- MnO_2 /CNFs nanocomposite exhibits excellent electrochemical performance of superior cycle capacity as well as high rate capacity. These outstanding performances are attributed to the unique hierarchical structure and synergetic hybridization of u- MnO_2 and CNFs which facilitates faster electron and Li ion transfer. The hierarchical composites of $\text{g-C}_3\text{N}_4$ QDs- MnCO_3 /carbon cloth were successfully fabricated on carbon cloth via a very simple hydrothermal method for the electrode materials of supercapacitors. The unique combination of MnCO_3 , $\text{g-C}_3\text{N}_4$ QDs and carbon cloth can release the pseudocapacitive potential of MnCO_3 by effective synergistic effect, $\text{g-C}_3\text{N}_4$ QDs and carbon cloth can improve the electron conductivity of nanocomposites. At the same time, the MnCO_3 and $\text{g-C}_3\text{N}_4$ QDs can ameliorate the hydrophilia in the electrolyte, then shorten the ion diffusion paths and furthermore increase the utilization of MnCO_3 . And rational GH-CN hybrid hydrogels with porous network structure were self-assembled by dispersion of $\text{g-C}_3\text{N}_4$ QDs in GO solutions

via a hydrothermal reaction. The g-C₃N₄ QDs play an important role in enhancing the pseudocapacitive activity, conductivity and promoted ion diffusion/transport capability. Benefiting from the synergistic effects of g-C₃N₄ QDs and porous network graphene hydrogel, the typical GH-CN electrode showed relatively good specific capacitance. A hierarchical structure like N-GQDs/MnCO₃/ZnMn₂O₄ composite electrode was designed and synthesized using simple, low-cost, and effective hydrothermal approach for supercapacitor applications. The resulting composite had a hierarchical structure formed with nanosheets, particles and quantum dots which provided a abundant pores for rapid electrons and ions transportation. Moreover, the dispersion of MnCO₃ particles on ZnMn₂O₄ nanosheets was more favorable to the synergistic effects, and the addition of N-GQDs enhanced higher conductivity.

7.2 Recommendations for future work

The transition metal oxides or compounds are good candidates for energy storage materials due to their high theoretical capacity, low cost, eco-friendliness, natural abundance, and high energy density. However, they also have some disadvantages such as low conductivity and volume change during charge and discharge process, which limits their high theoretical capacity to full utilization. In this case, some general strategies for performance enhancement are very necessary, and carbon materials or quantum dots are also good alternative for the medication, because they are good conductive media, mechanical support, faster ion and electron transport, and improve chemical and thermal stability. The composites including transition metal oxide or compound, carbon materials or quantum dots can be good candidates for energy storage materials.